Range uncertainty reductions in proton therapy and associated benefits for patients with brain or skull base tumors

Sebastian Tattenberg

15.10.2022

Range uncertainty reductions in proton therapy and associated benefits for patients with brain or skull base tumors

Dissertation
zum Erwerb des Doktorgrades der Naturwissenschaften
an der
Fakultät für Physik der
Ludwig-Maximilians-Universität München

Vorgelegt von
Sebastian Tattenberg
aus Leverkusen

München, den 15.10.2022

Erstgutachterin: Prof. Dr. rer. nat. Katia Parodi
Zweitgutachter: Prof. Dr. rer. nat. Thomas Bortfeld
Tag der mündlichen Prüfung: 30.01.2023

Zusammenfassung

Konventionelle externe Strahlentherapien zur Behandlung von Krebs basieren generell auf der Nutzung von Photonen, doch die Vorteile von protonenbasierten Behandlungen, die zu einer dem Tumor konformeren Dosisverteilung führen können, wurden bereits Mitte der 1940er Jahre erkannt.[1] Allerdings wurde die Protonentherapie erst durch technologische Fortschritte in den vergangenen Jahrzehnten zunehmend realisierbar, und Protonentherapien stehen weiterhin signifikanten Herausforderungen gegenüber.[2,3] Ein Beispiel dieser sind Ungenauigkeiten in der *in vivo* Protonenreichweite, die aus Faktoren wie den Bildern für die Bestrahlungsplanung und Unterschieden in der täglichen Positierung des Patienten herrühren.[4] Solche Reichweiteunsicherheiten verhindern es momentan, die potenziellen Vorteile der Protonentherapie voll auszunutzen. Viele verschiedene Ansätze, um *in vivo* Protonen-Reichweitenunsicherheiten zu reduzieren, werden daher momentan verfolgt. Diese Arbeit setzt sich zum Ziel, die Vorteile von Reichweiteunsicherheitsreduzierungen in der Protonentherapie zu quantifizieren und gleichzeitig zu Methoden zum Erreichen dieser beizutragen.

Dies umfasst die Quantifizierung direkter Vorteile von Reduzierungen der Reichweiteunsicherheit. Die Dosis des gesunden Gewebes und die Wahrscheinlichkeit einer strahlungsbedingten Nekrose des Hirnstamms oder Erblindung des Patienten wurde für zehn Patienten mit Clivus-Tumoren als Funktion der Reichweiteunsicherheit bestimmt. Patienten-spezifische Faktoren wie Tumorvolumen, verschriebene Strahlendosis, und der Abstand zwischen Tumor und *Chiasma opticum* wurden mit besonders hohen Vorteilen von Reichweiteunsicherheitsreduzierungen in Verbindung gebracht.

Allerdings werden Strahlrichtungen in der Protonentherapie momentan konservativ gewählt, um die potienziellen Effekte von Reichweiteunsicherheiten zu reduzieren. Indirekte Vorteile wie die Nutzung neuartiger Strahlenanordnungen bei niedrigeren Reichweiteunsicherheiten müssen daher ebenfalls in Betracht gezogen werden. Solche indirekten Vorteile wurden basierend auf einem Datensatz bestehend aus Behandlungsplänen für zehn Patienten mit Hirn- oder Schädelbasistumoren quantifiziert. Diese Studie bestätigte die Bedeutung von patientenspezifischen Faktoren wie dem Tumorvolumen und der verschriebenen Strahlendosis. Die zuvor genannten indirekten Vorteile überstiegen dabei die direkten Vorteile von Reduzierungen der Protonenreichweiteunsicherheit.

Die quantifizierten Vorteile von Verringerungen der Reichweiteunsicherheit können auf verschiedene Weisen erreicht werden. Spektroskopie der prompten Gammastrahlung, die während der Protonenbestrahlung emittiert wird erlaubt es, die Protonenreichweite in Echtzeit nachzuverfolgen. Die elementare Zusammensetzung des bestrahlten Gewebes kann somit ebenfalls bestimmt werden. Ein Prototyp für die Reichweitenverifizierung mittels Spektroskopie der emittierten prompten Gammastrahlung wurde am Massachusetts General Hospital (MGH) in Boston entwickelt. Die Leistung dieses Systems wurde für diese Dissertation anhand von Messungen in gewebenachahmenden und schweineartigen Proben verifiziert. Der Mittelwert des gemessenen Fehlers in der Protonenreichweite war hierbei für alle Proben kleiner als oder gleich 1.2 mm, und das System war in der Lage, basierend auf Sauerstoff- und Kohlenstoffanteil akkurat zwischen verschiedenen Gewebeproben zu unterscheiden.

Trotz zunehmender Forschung stellen Unsicherheiten in der Protonenreichweite weiterhin erhebliche Hürden der Protonentherapie dar. Die durchgeführten Studien quantifizieren die Vorteile und betonen somit die Bedeutung von Reduzierungen der Protonenreichweiteunsicherheit. Die durchgeführten Messungen tragen gleichzeitig einen Teil zu den beschriebenen Reichweiteunsicherheitsreduzierungen bei.

Abstract

Conventional radiotherapy for cancer is generally photon-based, but the physical advantages of proton-based treatments, which may allow for superior dose conformality to the tumor and superior normal tissue sparing, have been recognized as early as the mid-1940s.[1] However, only technological advancements in more recent decades rendered proton therapy more feasible, and proton treatments still face considerable hurdles.[2,3] The possibly most significant of these are uncertainties in the *in vivo* proton range, which stem from factors such as the images on which treatment plans are created and variations in patient setup between different treatment fractions.[4] Such range uncertainties currently prevent the potential advantages of proton therapy from being fully utilized. Many different approaches to reduce *in vivo* proton range uncertainties are therefore being investigated. This work aims to quantify the benefits of range uncertainty reductions while simultaneously contributing to methods which aim to achieve them.

This includes the quantification of direct benefits of range uncertainty reductions based on a set of ten cancer patients with clival tumors. Normal tissue metrics such as the dose to normal tissues as well as the probability of brainstem necrosis or blindness arising as a result of irradiation were determined as a function of range uncertainty. Patient-specific factors such as target volume, prescription dose, and distance between target and optic chiasm were linked to particularly high range uncertainty reduction benefits.

However, proton therapy beam arrangements are currently chosen conservatively in order to minimize the potential effects of uncertainties in the *in vivo* proton range. Indirect range uncertainty reduction benefits such as the feasibility of novel beam arrangements at lower levels of range uncertainty therefore also have to be considered. Such indirect benefits were quantified based on a data set of treatment plans for ten patients with brain or skull base tumors. This study confirmed the importance of patient-specific factors such as target volume and prescription dose. Indirect range uncertainty reduction benefits were observed to exceed the direct benefits of reductions in proton range uncertainties.

The quantified range uncertainty reduction benefits can be achieved in a multitude of different ways. Prompt gamma-ray spectroscopy - i.e., measurements of prompt gamma-rays emitted as a result of proton irradiation - allows proton ranges to be verified in real time. The elemental composition of the irradiated tissue can be determined simultaneously. A prototype for prompt gamma-ray spectroscopy-based proton range verification has been developed at Massachusetts General Hospital (MGH) in Boston. For this thesis, the detector prototype's performance was validated using a variety of tissue-mimicking and porcine samples. The mean measured range error was smaller than or equal to 1.2 mm for all samples, and the system was able to differentiate between samples of different elemental compositions accurately.

Proton therapy has experienced rapidly-growing interest in recent years. However, uncertainties in the *in vivo* proton range remain considerable hurdles. The studies conducted for the purpose of this thesis quantify the benefits and thereby emphasize the importance of reducing proton range uncertainties. At the same time, prompt gamma-ray spectroscopy measurements conducted for this thesis contribute towards eventually achieving the range uncertainty reductions studied.

Contents

List of Figures

List of Tables

List of Equations

Acronyms

MGH	Massachusetts General Hospital	i
USA	United States of America	1
GBD	Global Burden of Disease	1
NCDB	National Cancer Database	1
Gy	Gray	2
DIRAC	Directory of Radiotherapy Centres	2
IAEA	International Atomic Energy Agency	2
PTCOG	Particle Therapy Co-Operative Group	3
CT	Computed Tomography	4
OAR	Organ-At-Risk	4
NIST	National Institute of Standards and Technology	7
RBE	Relative Biological Effectiveness	8
LET	Linear Energy Transfer	8
LQ	Linear-Quadratic	8
DNA	Deoxyribonucleic acid	8
PIDE	Particle Irradiation Data Ensemble	9
LET$_d$	Dose-Averaged Linear Energy Transfer	9
IMRT	Intensity-Modulated Radiation Therapy	10
SOBP	Spread-Out Bragg Peak	10
PBS	Pencil-Beam Scanning	10
CBCT	Cone-Beam Computed Tomography	10
HU	Hounsfield Unit	12
MRI	Magnetic Resonance Imaging	13
PET	Positron Emission Tomography	13
SPR	Stopping Power Ratio	13
DET	Distal Edge Tracking	14
SFUD	Single Field, Uniform Dose	14
IMPT	Intensity-Modulated Proton Therapy	14
MCO	Multi-Criteria Optimization	14
SECT	Single-Energy-Spectrum Computed Tomography	15
GTV	Gross Target Volume	17
CTV	Clinical Target Volume	17
PTV	Planning Target Volume	17
DECT	Dual-Energy Computed Tomography	18
pCT	proton Computed Tomography	19
NTCP	Normal Tissue Complication Probability	24
TPS	Treatment Planning System	24
LKB	Lyman-Kutcher-Burman	27
CNS	Central Nervous System	46
PMT	Photomultiplier Tube	51
LaBr3:Ce	Cerium-Doped Lanthanum Bromide	51

CHAPTER 1

Introduction

In 2019, an estimated 10.1 million people died of cancer world-wide.[5] This makes cancer one of the leading causes of death globally, second only to cardiovascular diseases in terms of frequency. For the five most common causes of death, global numbers from 1990 to 2019 are shown in Figure 1.1. The Global Burden of Disease (GBD) study estimates a total of 56.5 million deaths globally for 2019. More than 1 in 6 deaths in 2019 was therefore attributable to cancer. Because of this prevalence, providing and improving upon high-quality cancer treatments remains of the utmost priority.

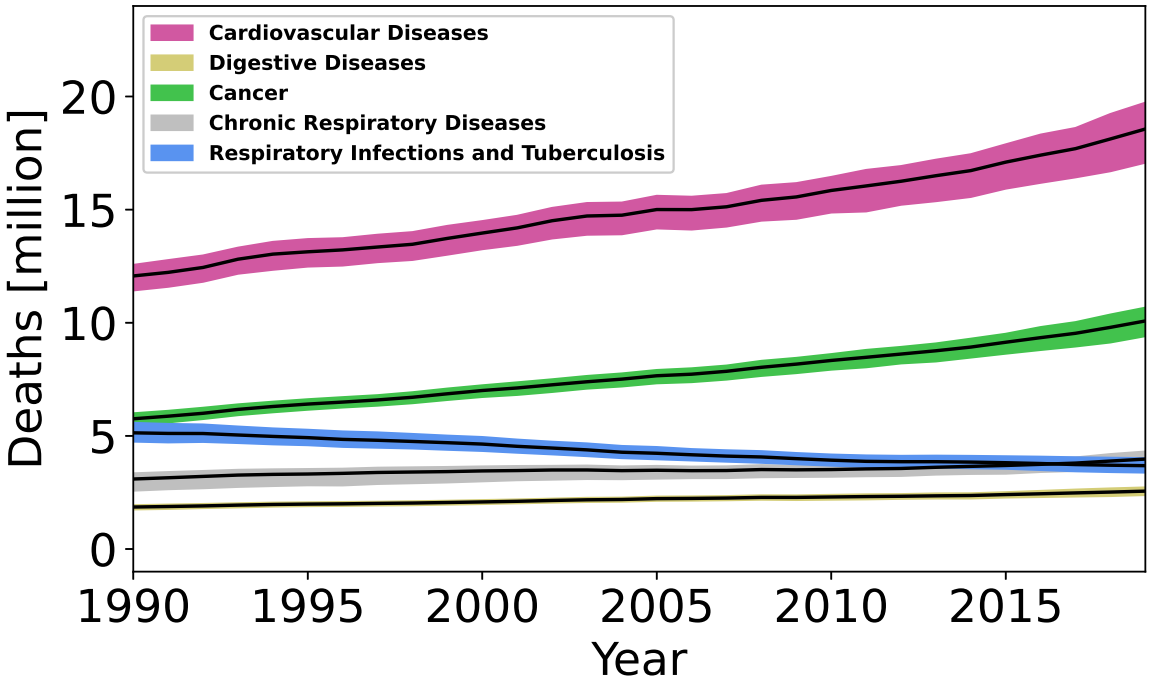

Figure 1.1: Leading causes of death globally from 1990 to 2019. During this period, cancer was second only to cardiovascular diseases in terms of the associated number of deaths. Data retrieved from the GBD study.[5]

Cancer treatments encompass a variety of different approaches and include surgery, radiation therapy, and chemotherapy and other systemic approaches. A treatment technique may be used on its own, but combining different kinds of treatment is also common. Utilization rates vary by country and depend on factors such as treatment site and stage. In the United States of America (USA), 3 in 10 cancer patients diagnosed between 2010 and 2019 received radiation therapy, be it by itself or in combination with surgery, chemotherapy, or other treatments.[6] The percentage of different first courses of treatment as provided by the National Cancer Database (NCDB) is shown in Figure 1.2.

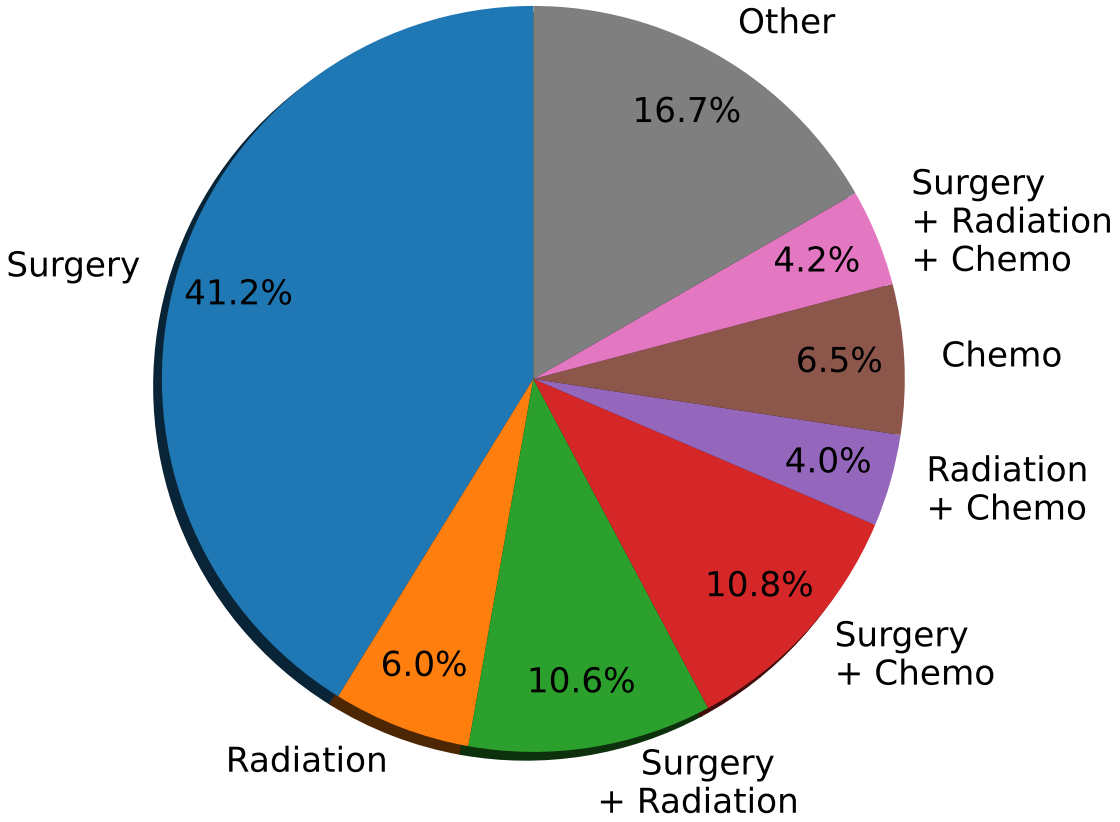

Figure 1.2: First courses of treatment prescribed to cancer patients in the USA who were diagnosed between 2010 and 2019. Data for all treatment sites retrieved from the NCDB.[6]

In radiotherapy, energy is delivered to the tumor via radiation, with the aim of damaging the genetic material contained in cancer cells and thereby preventing them from proliferating further.[7] Radiation dose is quantified in terms of the mean energy delivered per unit of mass. The corresponding unit is Gray (Gy), with 1 Gy = 1 $\frac{\text{J}}{\text{Kg}}$. Conventional radiotherapy treatments for which the patient is irradiated using an external beam are generally photon-based.

However, novel external beam radiotherapy techniques are slowly emerging as well. For example, delivering radiotherapy treatments using protons rather than photons was suggested as early as 1946.[1] The rationale behind proton radiotherapy is that proton depth-dose curves benefit from the Bragg peak, a localized region in which the majority of the radiation dose is deposited. The depth of the Bragg peak depends on the proton energy and can therefore be matched to the depth of the irradiated tumor. As a result, proton-based treatments allow for dose distributions with excellent conformality to the tumor. This improves sparing of organs-at-risk which are in close proximity to the irradiated target. An example of a proton depth-dose curve is shown in Figure 1.3.

Because of the aforementioned advantages, proton therapy has experienced rapidly growing interest in recent years. This is reflected in the number of proton therapy facilities in clinical operation globally, which has been growing exponentially. Figure 1.4 depicts the development of the number of proton therapy facilities in clinical operation globally, based on facilities which were still in clinical operation as of July 2022.

Nevertheless, proton therapy remains far from wide-spread. According to the Directory of Radiotherapy Centres (DIRAC) maintained by the International Atomic Energy Agency (IAEA), there are 4089 units for external radiotherapy with photons or electrons across Europe, compared to only 41 particle accelerators for light ion beam therapy.[9] Proton therapy also continues to face a variety of challenges, including uncertainties in the *in vivo* proton range. However, precise knowledge of the

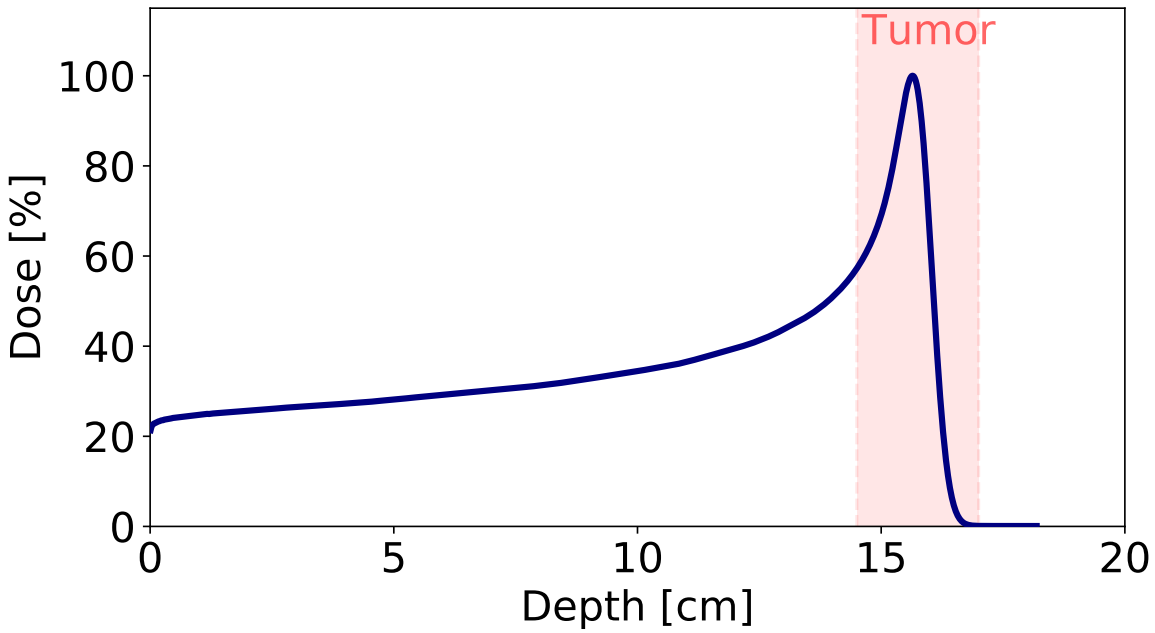

Figure 1.3: A proton depth-dose curve in water for a 150 MeV proton beam.

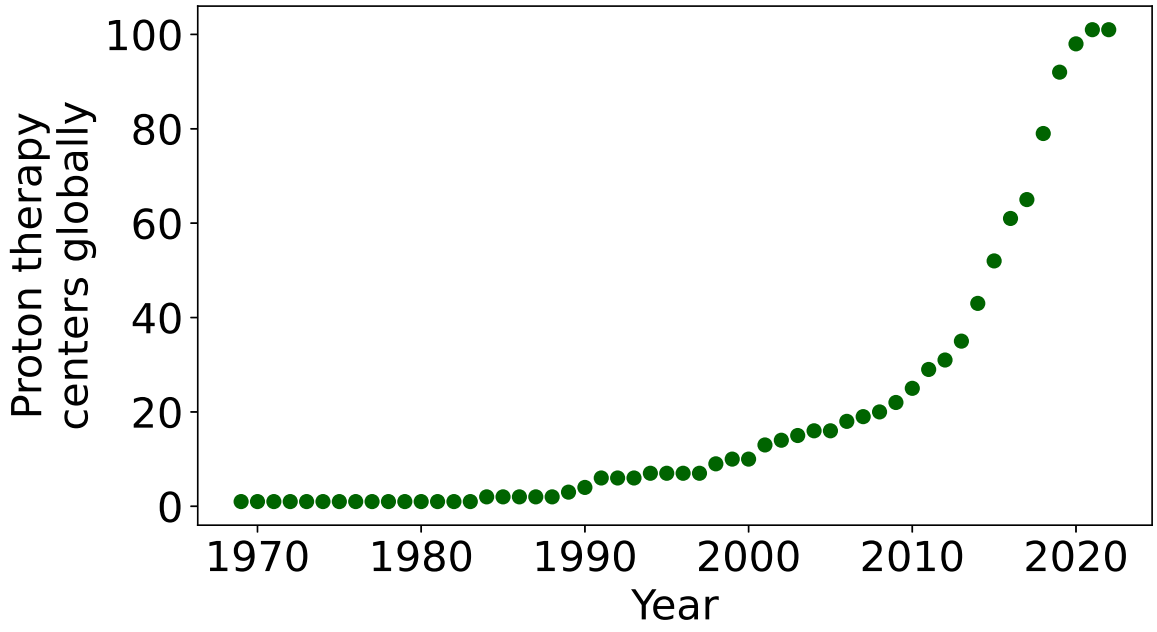

Figure 1.4: Proton therapy facilities in clinical operation globally. Data points indicate the year of the start of treatment and only include facilities which were still in clinical operation in July 2022. Data retrieved from the Particle Therapy Co-Operative Group (PTCOG).[8]

proton range is important because of the highly localized dose deposition associated with the use of protons. Proton range uncertainties can stem from a variety of different sources, including X-ray Computed Tomography (CT) images used for proton treatment planning, changes in patient anatomy, and variations in patient setup.[4] To reap the full benefits of proton therapy, a multitude of different range uncertainty reduction approaches are currently under investigation.

This thesis addresses a variety of different questions related to reducing range uncertainties in proton therapy and the benefits of range uncertainty reductions. Chapter 2 provides an introduction into proton therapy, including the underlying rationale, its clinical implementation, and proton range uncertainties and ways of reducing them. Chapter 3 then describes a study quantifying the direct benefits of range uncertainty reductions in terms of normal tissue and Organ-At-Risk (OAR) sparing, based on treatment plans for ten patients with clival tumors. The aforementioned study was conducted under the assumption of current clinical proton therapy practices. However, range uncertainty reductions also have additional indirect benefits. These include the feasibility of novel beam arrangements, which make greater use of the steep dose fall-off at the distal proton beam edge to conform the dose distribution to the target. At current levels of range uncertainty, such beam arrangements are often infeasible because they may risk unacceptably high doses to nearby OARs.[10] However, as range uncertainties are reduced, novel beam arrangements will become increasingly feasible and will allow for improved sparing of organs-at-risk which are in close proximity to the target. A further study quantifying the benefits of such novel beam arrangements was therefore also conducted, and is presented in Chapter 4. That study was based on treatment plans for ten patients with brain or skull base tumors.

The previously-quantified range uncertainty reduction benefits can be achieved in a multitude of different ways. This includes prompt gamma-ray spectroscopy, for which the proton range is validated based on the spectrum of prompt gamma-rays emitted during patient irradiation.[11,12] A detector prototope for prompt gamma-ray spectroscopy-based proton range verification has been developed at MGH in Boston.[13] Through measurements in a variety of tissue-mimicking and porcine samples, the performance of this detector prototype was validated for the study described in Chapter 5. A summary of the findings of this thesis is provided in Chapter 6, along with an overview over potential future research in the field.

CHAPTER 2

Proton therapy

Since the discovery of X-rays by Wilhelm Conrad Röntgen in 1895 and the first reported use of radiation as a cancer treatment in 1896, radiotherapy has come to play an essential role in the fight against cancer.[14,15] In the USA, 3 in 10 cancer patients diagnosed between 2010 and 2019 received radiotherapy.[6] Proton radiotherapy for cancer was suggested as early as 1946.[1] However, only recent technological developments rendered this treatment technique considerably more feasible.[2] Radiotherapy treatments for which the patient is irradiated with an external beam therefore remain largely photon-based. Due to its physical and biological advantages over conventional photon treatments, proton therapy has experienced growing interest in recent years, but the use of protons is also accompanied by a variety of unique challenges which have to be overcome for full use to be made of these advantages.[16–19]

2.1 Fundamentals of proton therapy

Proton therapy saw its first clinical application at the University of California in Berkeley in 1954, and a study reporting on the treatments of 26 metastatic breast cancer patients was published in 1957.[20,21] Even so, the first accelerator for clinical proton therapy was not installed at a hospital until the installation of a synchrotron at Loma Linda University Medical Center in Loma Linda, California in 1990.[22,23] The number of proton therapy centers in operation globally has been rising exponentially since, as has the number of patients receiving proton treatments, but technical challenges and the high costs associated with building and maintaining proton therapy facilities remain of concern.[8,18,19,22]

2.1.1 Physical rationale

As protons traverse matter, they undergo a variety of different interactions, including:[24]

- **Inelastic Coulomb scattering** with atomic electrons, mainly resulting in (quasi-continuous) energy loss
- **Elastic Coulomb scattering** with atomic nuclei, mainly resulting in lateral deflection
- **Non-elastic nuclear interactions**, which decrease the fluence of primary protons and result in the emission of secondary particles

One of the main advantages of proton therapy over conventional photon treatments is the high degree of conformality of the resulting dose distributions.[1] This is the result of the Bragg peak, a region of highly localized dose deposition near the proton end-of-range.
As charged particles such as protons traverse matter, they deposit energy in the medium through which they are moving. The stopping power S is defined as the mean amount of energy dE lost per unit length of traversed matter dx:[24]

$$S = -\frac{dE}{dx}. \tag{2.1}$$

For charged particles with masses much higher than the electron mass and energies above 1 MeV per atomic mass unit, the stopping power can be calculated using the Bethe-Bloch equation:[24–26]

$$S = -\frac{dE}{dx} = 4\pi N_A r_e^2 m_e c^2 \rho \frac{Z}{A}\frac{z^2}{\beta^2}\left(\ln\left(\frac{2m_e\gamma^2 v^2}{I}\right) - \beta^2 - \frac{\delta}{2} - \frac{C}{Z}\right), \tag{2.2}$$

where N_A = 6.022 x 10^{23} mol^{-1} is Avogadro's number, r_e and m_e are the radius and rest mass of the electron, and c is the speed of light. Furthermore, ρ is the mass density of the absorbing material with atomic number Z and mass number A, z is the charge of the projectile, and $\beta = \frac{v}{c}$, where v is the projectile's velocity. In addition, the Lorentz factor $\gamma = \frac{1}{\sqrt{1-\beta^2}}$, I is the mean excitation potential of the absorbing material, and δ and C are density and shell correction terms, respectively.[27] The shell correction is relevant at low proton energies because the Bethe-Bloch equation's assumption of orbital electrons being stationary is no longer valid in such scenarios. The density correction, on the other hand, is relevant at high proton energies and results from shielding of electrons which are further away from the incoming protons.
The energy transfer described above is mostly the result of excitation or ionization events of atomic electrons. Primary protons are removed from the beam through nuclear reactions, but the accompanying decrease in dose is largely compensated by the emission of secondary particles.[24] The percentage of the total dose that is delivered by secondary protons has been reported to be up to 10%.[28] As shown in Equation 2.2, the stopping power is inversely proportional to the square of the projectile's velocity:

$$S \propto \frac{1}{v^2}. \tag{2.3}$$

This is the result of lower projectile velocities allowing for longer interaction times between the incoming projectile and atomic electrons in the absorbing material.
A comparison of the depth-dose curves of a 150 MeV proton beam (as shown in Figure 1.4) and a 6 MeV photon beam traversing water is provided in Figure 2.1.

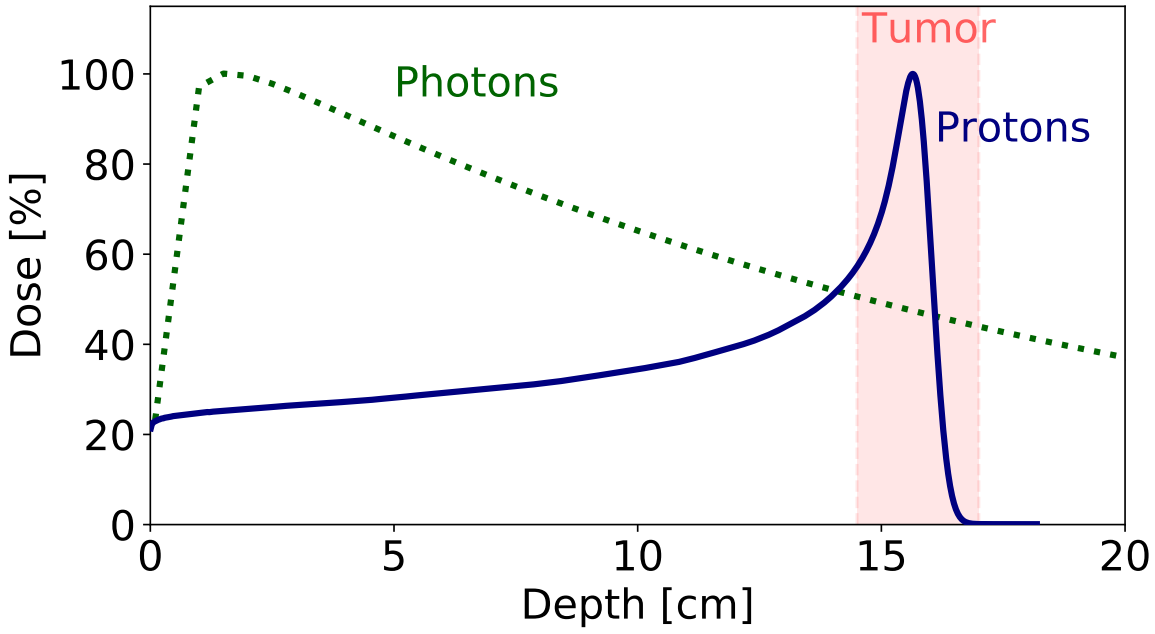

Figure 2.1: Proton and photon depth-dose curves in water for a 150 MeV proton (solid blue line) and a 6 MeV photon beam (dashed green line). Photon data modeled according to Li et al.[29]

Photon depth-dose curves exhibit an initial build-up region, which results from the range of secondary electrons through which dose is deposited. After said build-up region, attenuation results in the photon dose falling off exponentially as a function of depth. The proton depth-dose curve, on the other hand, exhibits a comparatively low plateau region until it reaches the Bragg peak, where the majority of the dose is deposited in a highly localized area.
The proton range R, which is defined as the depth at which half of the initial protons have come to rest, is strongly related to the initial kinetic energy E_{ini} and can be calculated numerically:[24]

$$R(E_{ini}) = \int_0^{E_{ini}} \left(\frac{dE}{dx}\right)^{-1} dE. \tag{2.4}$$

The range of the proton beam and the depth of the Bragg peak therefore increase with energy. This allows the depth of the Bragg peak to be tuned to the depth of the tumor, by selecting a higher initial kinetic energy for deeper-seated tumors. As a result, proton therapy is able to achieve superior dose conformality to the tumor and better normal tissue sparing than conventional photon treatments.[30–32]
Proton range as a function of kinetic energy is shown in Figure 2.2.

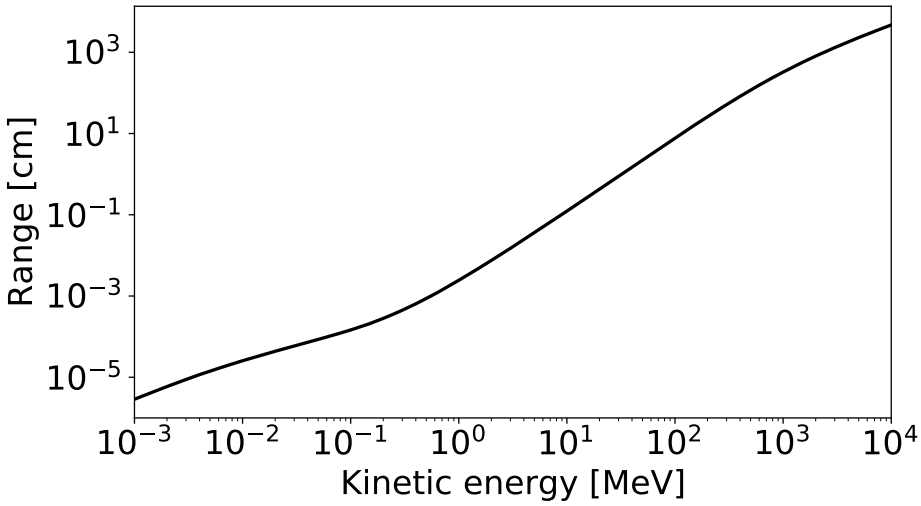

Figure 2.2: Proton range in water as a function of kinetic energy. Data was retrieved from the PSTAR database of the National Institute of Standards and Technology (NIST).[33]

However, the proton beam delivered to the treatment room is not truly mono-energetic, and there are small differences in the energy loss experienced by different protons within the beam.[24] Because of the relationship between kinetic energy and range, this energy straggling also translates into range straggling, helping to explain the shape of the Bragg peak. Since energy and range straggling accumulate as the beam traverses an increasing amount of material, higher-energy proton beams with a higher range also exhibit more pronounced range straggling.[24]
In addition to the dose which is deposited by secondary particles, protons undergoing nuclear reactions are also relevant because they enable many of the research efforts which will be discussed later in this thesis. A nuclear reaction may only occur if a proton has an energy sufficient to overcome the Coulomb barrier of the nucleus, which is on the order of 8 MeV for relevant elements.[24] Possible nuclear reactions are manifold, but the most relevant ones for this thesis lead to the emission of prompt gamma-rays (for example through $^{16}O(p, p'\gamma)^{16}O$) or the creation of positron emitters such as ^{15}O. This is because detection of emitted prompt gamma-rays or photons resulting from positron-electron annihilation enables verification of the proton range *in vivo*, either in real time or shortly after irradiation (cf. Section 2.2.3).

2.1.2 Biological rationale

Proton therapy dose calculations have to account for the difference in biological effectiveness between proton and photon irradiation. This difference is considered in the form of the Relative Biological Effectiveness (RBE) value, which is given by the ratio between the photon dose D_γ and the proton dose D_p which results in the same biological response:[34]

$$\mathrm{RBE} = \frac{D_\gamma}{D_p}. \tag{2.5}$$

Proton and photon cell survival curves and an exemplary RBE calculation are shown in Figure 2.3.

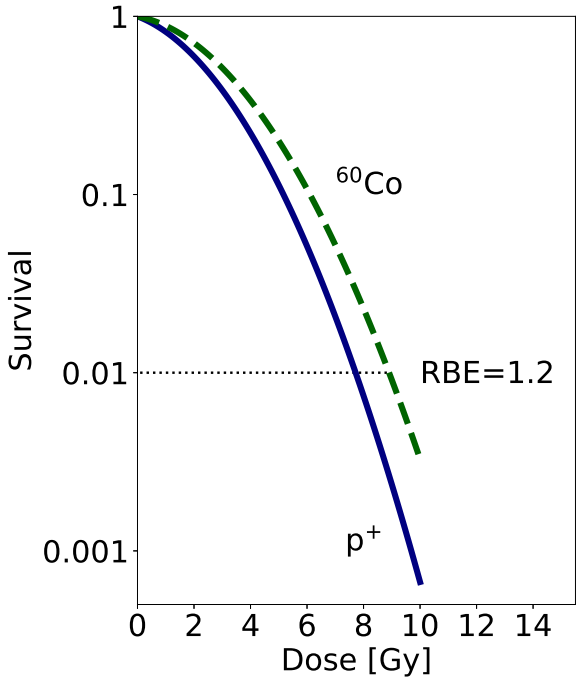

Figure 2.3: Proton and photon cell survival curves of Chinese hamster lung fibroblasts V79-379A irradiated with a 67 MeV proton beam (solid blue line) and gamma-rays from the decay of ^{60}Co (dashed green line). Figure adapted from parameters published by Blomquist et al.[35]

In current clinical practice, a constant RBE value of 1.1 is applied, which was chosen based on a range of considerations, including *in vivo* data.[34] However, evidence suggests that RBE may depend on a variety of parameters, including the biological endpoint considered, the delivered dose, the radiosensitivity of the irradiated cells in form of their $\frac{\alpha}{\beta}$ ratio, and the Linear Energy Transfer (LET), i.e., the mean amount of energy lost per unit length:[36–38]

- **Dose:** As shown in Figure 2.3, photon dose-response curves exhibit a shoulder region which results in larger differences between proton and photon irradiation being observed at lower doses. RBE is therefore higher at lower doses.

- $\frac{\alpha}{\beta}$ **ratio:** Cell survival S after irradiation with dose D is commonly modeled using the Linear-Quadratic (LQ) model:[39]

$$S = e^{-\alpha D - \beta D^2}. \tag{2.6}$$

Deoxyribonucleic acid (DNA) damage which was caused by a single incoming particle and leads to cell death can be interpreted as being described by α, while β can be interpreted as cell deaths which are the result of DNA damage caused by two different particles. The ratio $\frac{\alpha}{\beta}$ describes the dose at which the linear and the quadratic component are equal. Since the slope of the different sections of the dose-response curve affects RBE, the RBE also depends on the $\frac{\alpha}{\beta}$ ratio. Namely, a higher RBE is observed at lower $\frac{\alpha}{\beta}$ ratios.

- **LET:** RBE generally increases as a function of LET. This is the result of more local energy deposition increasing the probability of lethal DNA damage. At a very high LET, however, the overkill effect is observed - a higher local dose deposition does not cause a further biological effect, leading to a decrease in RBE. Figure 2.4 depicts RBE as a function of LET. The Dose-Averaged Linear Energy Transfer (LET_d) is sometimes used as a surrogate of biological effectiveness, and is defined as:[40]

$$\text{LET}_d = \frac{\sum_i d_i \text{LET}_i}{\sum_i d_i}, \tag{2.7}$$

where d_i is the dose deposited in a given volume element by particle i with LET_i.

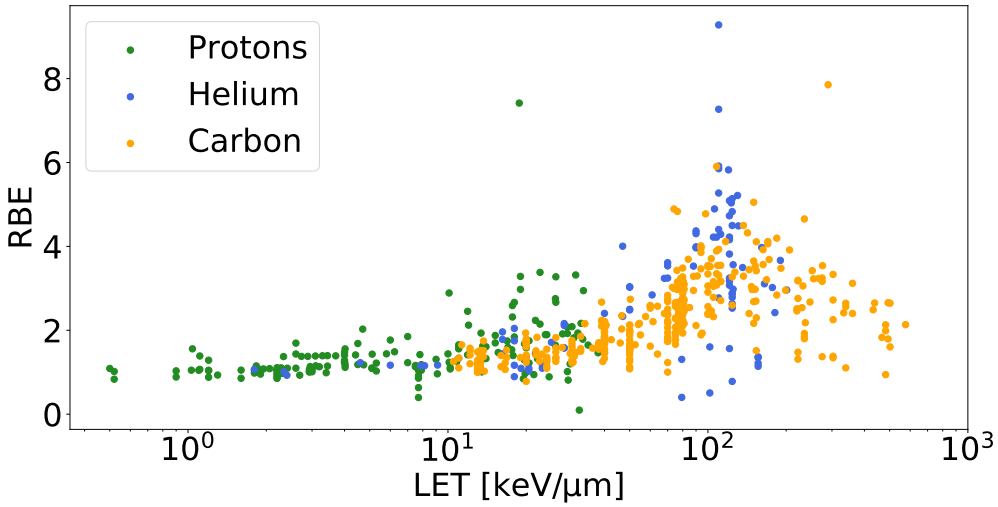

Figure 2.4: RBE as a function of LET. Data was retrieved from the Particle Irradiation Data Ensemble (PIDE) maintained by the GSI Helmholtz Center for Heavy Ion Research.[41]

A range of phenomenological approaches to model the variability of RBE have been developed, and the potential effects of variations in RBE have been investigated.[42,43] It has been suggested that, especially in cases with critical structures at the distal edge of the target, RBE deviations from a value of 1.1 may have considerable adverse effects on the dose to nearby OARs.[44,45] Variations in RBE may therefore have clinical implications, and variable RBE models may see clinical implementation in the future.

2.1.3 Clinical rationale

As discussed in Section 2.1.1, proton therapy is associated with superior dose conformality to the target than conventional photon treatments. Numerous (largely retrospective) studies have reported associated improvements in OAR and normal tissue sparing. Cases in which proton therapy has

been reported to markedly improve normal tissue and OAR sparing and/or reduce toxicities compared to traditional photon therapy include a range of tumors in the head & neck region and pediatric patients.[30–32,46–50] For patients with malignant tumors within the nasal cavity or paranasal sinuses, a meta-analysis linked proton therapy to considerably higher five-year disease-free survival and locoregional control at the longest follow-up than conventional Intensity-Modulated Radiation Therapy (IMRT).[51] Recent retrospective studies focusing on hepatocellular carcinoma patients treated with photon or proton therapy observed a lower risk of radiation-induced liver disease and increased overall survival in the proton cohort.[52,53]
Nevertheless, possibly due to factors including uncertainties during treatment delivery, technical challenges, and a lack of long-term experience and randomized trials, efforts to translate the physical advantages of proton therapy into clinical data showing clear superiority over photon treatments have been slow.[18,19] Various randomized trials are currently still ongoing, but a phase IIB randomized trial comparing proton therapy to photon-based IMRT for locally advanced esophageal cancer reported fewer and less severe adverse events in the proton than in the photon group.[54–59] Phase II trials aim to assess efficacy and determine potential side-effects, and a reduction in side effects was also reported by a randomized phase II trial which compared proton and photon therapy for glioblastoma and which observed lower rates of radiation-induced grade 3+ lymphopenia in the proton cohort.[60,61]

2.1.4 Clinical implementation

To achieve the required energies, proton therapy centers generally rely on an accelerator connected to multiple treatment rooms via a high-energy beam transport line, which contains several magnetic components for beam deflection and focusing and which may be dozens of meters in length.[18] Proton beams may enter the treatment room at a fixed position, but proton gantries capable of rotating up to a full 360°and which can weigh 120 tons or more are now more established.[62] However, a new generation of compact and cost-effective single-room systems were recently developed and commissioned as well.[63–65] Proton therapy is generally based on one of two delivery techniques: passive scattering and active Pencil-Beam Scanning (PBS). In the following section, both of these techniques will be reviewed after a brief introduction to the procedures through which a patient is positioned for treatment.

Patient positioning

Treatment couches in proton therapy may provide six degrees of freedom to allow for accurate patient positioning, but facility- or even treatment room-specific considerations can lead to limitations. An example of a proton therapy treatment room is shown in Figure 2.5. Proton therapy often relies on a laser system for the initial patient setup, followed by orthogonal X-ray imaging, Cone-Beam Computed Tomography (CBCT), or a scan with an X-ray CT scanner placed on rails for more accurate patient alignment.[66] However, alternative approaches including proton-based patient positioning are also under investigation.[62,67–69]

Passive scattering

In passive scattering, proton beam delivery to the entirety of the target is achieved through the use of multiple components which are placed in the beam path.[18,70] In depth, the mono-energetic proton beam is modulated using a rotating modulation wheel so that all parts of the target are covered. The wheel consists of sections of different thicknesses, so the range shift protons experience depends on upon which section of the modulation wheel they are incident. This allows a variety of different ranges to be achieved. An exemplary Spread-Out Bragg Peak (SOBP) achieved through superimposition of Bragg peaks of different energies is shown in Figure 2.6.

Figure 2.5: A treatment room in the Francis H. Burr Proton Therapy Center located at Massachusetts General Hospital in Boston, Massachusetts, USA.

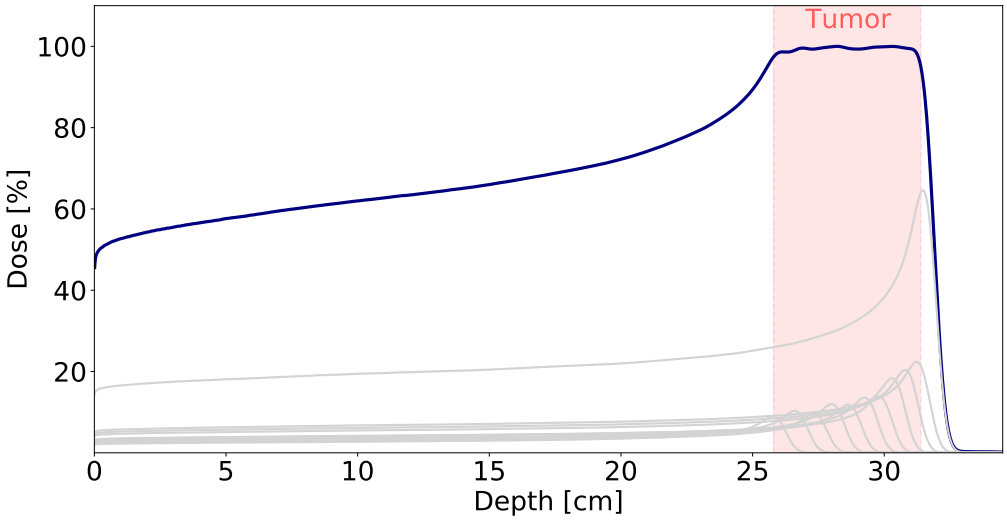

Figure 2.6: A spread-out Bragg peak resulting from superimposition of multiple pristine Bragg peaks. The pristine Bragg peaks through which the SOBP is achieved are shown in light grey. The energies of the Bragg peaks used ranged from 199.1 MeV to 223.6 MeV.

Lateral beam spreading is accomplished through the use of scatterers made from materials with a high atomic number. For all irradiation fields, dose conformality at the distal and lateral beam edges can be tailored to the patient-specific shape of the tumor through the use of a range compensator and an aperture, respectively. A schematic of passive scattering is shown in Figure 2.7.

Pencil-beam scanning

In PBS, on the other hand, different proton ranges are instead achieved through modulation of the proton beam's energy.[71,72] This process either occurs at the accelerator level (i.e., through the use of a synchrotron) or, in the case of cyclotrons, via an energy degrader system of variable thickness just after proton extraction. This results in an SOBP as already shown in Figure 2.6. Laterally, irradiation of different parts of the target is accomplished through beam steering by sweeper magnets. Unlike passive scattering, pencil-beam scanning does not rely on components being placed in the beam path, with the exception of minor components required for beam monitoring. Since it provides greater flexibility and reduces neutron contamination, active scanning is considered superior to passive scattering and has been reported to be able to improve dose conformality and OAR and normal tissue sparing.[73,74] A schematic of active PBS is also shown in Figure 2.7.

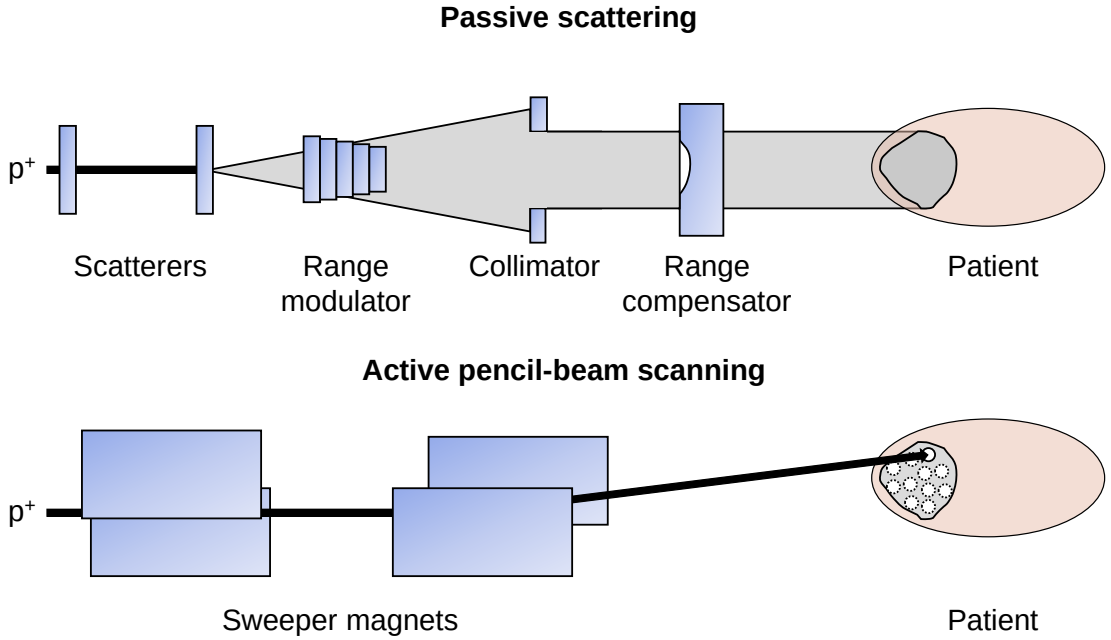

Figure 2.7: Passive scattering and active pencil-beam scanning in a simplified schematic drawing. The components shown are limited to beam-spreading devices and do not include monitoring components such as ionization chambers.

2.1.5 Treatment planning

As is the case for conventional photon treatments, proton therapy generally requires an X-ray CT scan of the patient to be acquired on a CT simulator. The unit of CT images is the Hounsfield Unit (HU), which depends on the linear attenuation coefficient of the volume element in question μ as well as the linear attenuation coefficient of water μ_w:[75]

$$\mathrm{HU} = 1000 \left(\frac{\mu - \mu_w}{\mu_w} \right). \tag{2.8}$$

The aforementioned CT scan is necessary for both treatment planning itself as well as for accurate patient positioning based on X-ray images acquired in the treatment room prior to patient treatment.[62] Organs-at-risk and target structures are delineated on the planning CT, generally supported by an additional imaging modality such as Magnetic Resonance Imaging (MRI) (for superior soft tissue contrast) or Positron Emission Tomography (PET) (for functional information)(cf. Section 2.2.1).[76] Treatment planning images are acquired with the same immobilization devices as will later be used during irradiation, and images acquired on different machines can be co-registered to each other using (deformable) image registration algorithms. Values of the proton Stopping Power Ratio (SPR) relative to water, which are required for treatment planning, are often determined from CT numbers via a heuristic approach.[77] Constraints and objectives are defined for doses delivered to the delineated target(s) as well as to any relevant OARs. An example of a treatment planning CT scan, with some of the delineated target and OAR structures overlaid on it, is shown in Figure 2.8.

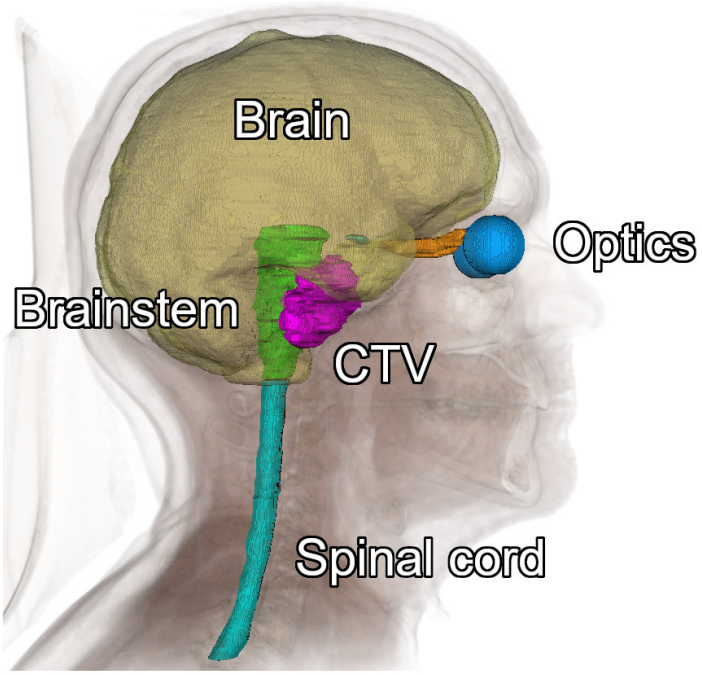

Figure 2.8: A treatment planning CT scan and delineated structures required for treatment planning. Structures are generally defined on discreet slices of the patient CT, but this figure depicts closed surfaces instead for clarity. CTV refers to the clinical target volume.

Efforts to replace treatment planning CT imaging with an MRI scan, motivated by advantages such as MRI's superior soft tissue contrast, are currently being undertaken.[78,79] However, accurately determining parameters necessary for proton therapy treatment planning solely based on images which are not themselves acquired using radiation remains a considerable obstacle.

Pencil-beam spot placement

In active pencil-beam scanning, spots to which protons will be delivered are generally placed at discrete positions throughout - and, to some extent, in close proximity to - the target, and treatment plan optimization takes the form of optimizing the proton fluence delivered to each pencil-beam spot. This is an inverse treatment planning approach, since the definition of requirements on the resulting dose distribution (in the form of dose constraints and objectives for target(s) and OARs) occurs first.[80] Pencil-beam spot weights capable of achieving a dose distribution which fulfills these requirements are only determined subsequently, through treatment plan optimization. An example of a map of proton pencil-beam spot positions is shown in Figure 2.9.

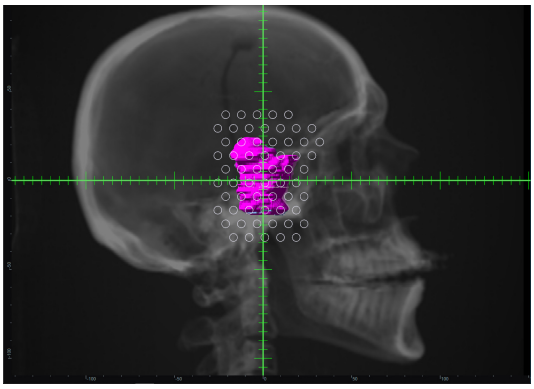

Figure 2.9: Proton pencil-beam spot placements for a single energy layer. The tumor is shown in pink, and the anatomy is shown as a two-dimensional projection of the treatment planning CT scan.

Spot placement approaches may differ between treatment plans. For three-dimensional modulation, proton pencil-beam spots are placed throughout the target.[81,82] Since this was the spot placement approach with which the selected patients had been treated clinically, this was also the method used for all treatment plans created for this thesis. Parameters such as the spacing between spots and the spacing between energy layers may be modified, but for this work, the default values also used for clinical treatments were chosen. An alternative spot placement approach is Distal Edge Tracking (DET), which limits spot positions to the target's distal edge. This approach potentially improves normal tissue sparing without comprising target coverage, but comes at the cost of higher susceptibility to uncertainties and delivery errors.[83]

Treatment plan optimization

Proton therapy treatment plans generally consist of one or a few treatment fields - i.e., treatment couch position and gantry angle combinations with which the patient is irradiated. Each treatment field is associated with its own pencil-beam spot map, and dose distributions delivered by the different fields may have restrictions placed upon them. As the name suggests, the Single Field, Uniform Dose (SFUD) approach requires every treatment field to deliver a uniform dose distribution.[84] In Intensity-Modulated Proton Therapy (IMPT), on the other hand, no such requirement is placed upon the dose distributions delivered by individual fields. Field-wise dose distributions can therefore be heterogeneous, and the desired total dose distribution, which is typically homogeneous within the target, is only achieved by combining all field-wise dose distributions, assuming correct patient alignment and treatment delivery. IMPT can allow for superior total dose distributions but is also more susceptible to the effects of potential uncertainties.[82,85–87] IMPT is used for two of the studies performed for this thesis and is only possible when proton therapy is delivered via PBS rather than passive scattering.
During treatment planning, planning constraints (which must be fulfilled) and planning objectives (which are fulfilled as far as possible, according to their relative weight) are defined for the target structure(s) as well as all relevant OARs. Multi-Criteria Optimization (MCO), which allows the treatment planner to choose from a range of potential treatment plans which all fulfill the specified constraints but vary in the weighting of planning objectives, is common.[88,89] Proton dose calculations commonly utilize the analytical pencil-beam algorithm originally developed by Hong et al., which calculates the total dose distribution as the sum of the dose distributions delivered by many individual pencil-beams.[90] However, dose calculations can also be performed using Monte Carlo simulations, which simulate the transport and interactions of particles within the patient based on information on patient anatomy (e.g., a CT scan) and the incoming particles (e.g., the generated treatment plan).[91] Knowledge of the probabilities of relevant physical processes, for example in the form of experimen-

tal cross-section data, is also required. Monte Carlo simulations have seen extensive use in a variety of different areas of medical physics, and Monte Carlo simulation tools tailored to the use in proton therapy specifically have been developed.[92,93] Dose calculations using Monte Carlo simulations have recently seen commissioning as well and especially provide higher accuracy compared to analytical methods when heterogeneities are present.[94]

Adaptive proton therapy

Proton therapy treatments are generally delivered in multiple treatment fractions, with the number of fractions depending on aspects such as the patient, the treatment site, and the treatment technique. Examples of fractionation schemes relevant to this thesis include a prescription dose of 54 Gy(RBE) delivered over the course of 30 treatment fractions. Historically, a proton therapy treatment plan is created based on the planning CT scan acquired prior to the first treatment fraction, and the same treatment plan is used for all treatment fractions. However, the use of a single planning CT scan is under investigation because significant inter-fractional anatomical changes may occur over the course of the treatment, especially for prostate cancer, head and neck tumors, and tumors in the thoracic or upper abdominal region, including the lungs and the liver.[95,96] Because of the highly localized dose deposition in the Bragg peak, proton therapy is much more susceptible to such anatomical changes than conventional photon treatments. Anatomical variations can therefore markedly affect the delivered dose distribution and even result in adverse effects.
To address such issues, adaptive radiotherapy utilizes patient images acquired over the course of treatment to re-optimize the treatment plan under consideration of inter- and intra-fractional anatomical changes.[97,98] Proton therapy treatment plan adaptation can occur weekly or even daily, and often relies on photon-based imaging techniques such as CT or CBCT, but the use of MRI is also under investigation.[99–101] Since treatment plan re-optimization is time-intensive, adaptation in proton therapy is currently done offline rather than online.[102–105] For the former, treatment plan adaption occurs between treatment fractions while for online adaption, the treatment plan is modified immediately prior to the delivery of a treatment fraction. Challenges include corrections of the CT numbers in the CBCT to make it suitable for proton dose calculations and, for MRI-based adaptation, design and magnetic shielding considerations as well as the conversion of the images into properties relevant for proton therapy dose calculations.[95]

2.2 Uncertainties in proton therapy

In clinical practice, proton therapy is subject to several considerable limitations.[4,106] These include uncertainties in the *in vivo* proton range, which are generally accounted for through use of a margin on the order of 2.5% + 1.5 mm to 3.5% + 3 mm.[4] Sources of range uncertainties are manifold and include the X-ray Single-Energy-Spectrum Computed Tomography (SECT) treatment planning images and their conversion to proton SPR values - i.e., the ratio of the stopping power of the relevant material and the stopping power of water.[107–109]
For proton therapy treatment planning, CT numbers in the treatment planning scan, which is generally acquired using a single energy spectrum, are often converted to the required SPR values using a heuristic, piece-wise linear conversion.[77] However, proton SPRs are a function of relative electron density and the mean ionization potential of the relevant material, and a single CT scan acquired using a single energy spectrum is not sufficient to fully resolve the resulting ambiguities.[110] For example, tissues may have different SPRs but exhibit the same HU value in the treatment planning images, or *vice versa*.[111]
Further sources of range uncertainty include inter- and intrafractional anatomical changes as already discussed in Section 2.1.5.[112,113] Variations in patient setup may also play a role. However, random setup errors are not expected to have a major impact over the course of all treatment fractions, at least in cases in which the treatment is divided into a considerable number of fractions.[114]

2.2.1 Including uncertainties during proton therapy treatment planning

A failure to account for uncertainties such as the ones discussed in Section 2.2 may result in underdosing of the target or excessive doses to nearby organs-at-risk, among other undesired outcomes. Taking into account uncertainties during treatment planning is therefore essential. This can be achieved in a variety of different ways, including through the use of conservative beam angles, the inclusion of margins, and optimization approaches assuring dose distribution robustness in a variety of error scenarios.

Conservative beam arrangements

The effects of uncertainties in the *in vivo* proton range are limited to the beam direction. In error scenarios, proton range uncertainties can only result in an under- or overshoot relative to the expected range. The potential effects of range uncertainties on doses to nearby sensitive structures can therefore be reduced through the choice of conservative beam arrangements.[10,85]
The dose fall-off at the distal beam edge is considerably steeper than the dose fall-off at the lateral edge of the proton beam. It would therefore be beneficial to conform the dose distribution to the target using the distal beam edge. This is especially true in cases in which an OAR is located just behind the distal end of the target, as it would allow for a particularly steep dose gradient at the target-OAR interface. However, in overshoot scenarios, this approach could cause almost the full target dose to be "pushed" into the OAR in question. In order to reduce the potential effects of range uncertainties, traditional proton therapy beam arrangements therefore rely more heavily on the lateral rather than the distal beam edge. In overshoot scenarios, greater reliance on the lateral beam edge causes dose to be delivered along rather than into the adjacent OAR. Use of the lateral and distal beam edge is depicted in Figure 2.10.

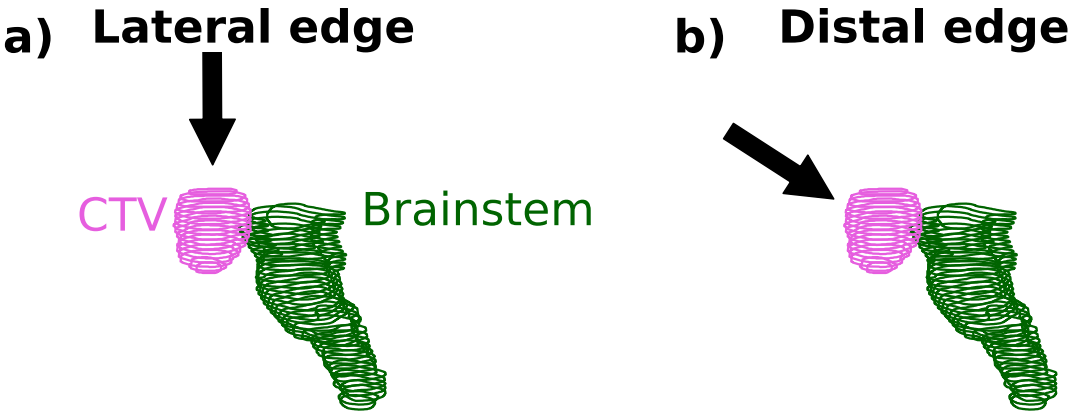

Figure 2.10: Use of the (a) lateral and (b) distal proton beam edge to conform the dose distribution to a clinical target volume (CTV) in close proximity to an OAR. The dose fall-off at the distal beam edge is steeper, but greater reliance on the distal beam edge is also more susceptible to the effects of uncertainties in the proton range.

Since use of the lateral beam edge can be considered safer in a wide range of scenarios, this approach is commonly utilized at current levels of range uncertainty.[18,115] However, since the dose fall-off at the lateral beam edge is considerably less steep than the distal dose fall-off, conforming the dose distribution to nearby OARs using the lateral beam edge comes at the cost of increased OAR doses in low range error scenarios. As range uncertainties are reduced, greater reliance on the distal beam edge may therefore improve OAR sparing, as addressed in Chapter 4 of this thesis.

Planning target volume (PTV)

Another approach to consider proton range uncertainties during treatment planning is to add margins accounting for such uncertainties to the target structure. The Gross Target Volume (GTV) contains the known tumor region and is expanded to the Clinical Target Volume (CTV) to account for microscopic tumor spread.[116] Margins can be added to the CTV to account for uncertainties from a variety of different sources, yielding the Planning Target Volume (PTV), which can be used as the target structure during treatment planning to assure sufficient target coverage of the CTV in a range of possible error scenarios.[117–119] Sources of error which can be considered in the form of PTV margins include variations in patient setup and uncertainties in the *in vivo* proton range, with margin magnitudes depending on considerations such as treatment site. As mentioned previously, typical range uncertainty margins range from 2.5% + 1.5 mm to 3.5% + 3 mm.[4]

Robust optimization

An alternative approach to account for uncertainties in proton therapy is to include them in the optimization directly. For conventional treatment planning, planning constraints and objectives are only defined in the nominal scenario in which no errors of any kind occur. Target coverage and OAR sparing in error scenarios are not included in the optimization. Robust treatment planning, on the other hand, allows planning constraints and objectives to be applied to error scenarios (in which e.g., setup and/or range errors occur) in addition to the nominal scenario.[120,121] This assures consistent target coverage and/or OAR sparing in a variety of error scenarios at the cost of compromised dose conformity to the target in the nominal scenario. Examples of dose distributions resulting from non-robust and robust optimization are shown in Figure 2.11.

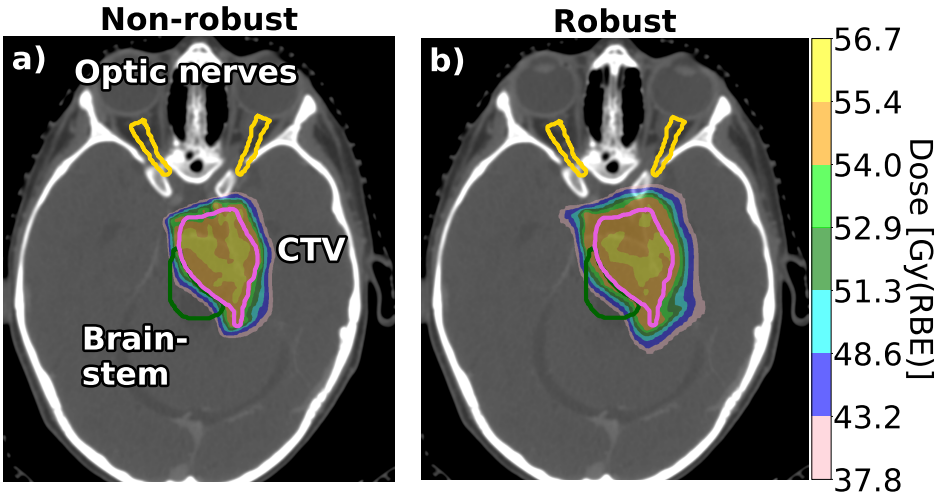

Figure 2.11: Dose distributions resulting from (a) non-robust and (b) robust optimization. The dose distribution in (b) results from a treatment plan for which setup errors of ±2 mm and range errors of 4% were included in the optimization. Both treatment plans are for the same patient, and both dose distributions concern the nominal scenario.

Implementations of robust optimization

Since robust optimization and the PTV are different ways of accounting for the same types of uncertainties, the target structure used for robust treatment planning is the CTV rather than the PTV. Robust optimization can be implemented in a variety of different ways, depending on which scenario one seeks to emphasize. In the stochastic or probabilistic approach, every scenario is assigned a weight according to the scenario's likelihood or relative importance.[120,121] The expected value of the

objective function is then minimized:[122]

$$\min_x \sum_{i=1}^{n} p_s f(d(x;s)), \tag{2.9}$$

where x is the proton fluence, p_s is the probability or weight of scenario s, f is the objective function, and d is the dose distribution in scenario s.
The minimax or worst-case approach, on the other hand, optimizes the worst-case scenario, independently of the scenario's likelihood:[122,123]

$$\min_x \max_s f(d(x;s)). \tag{2.10}$$

Different ways of implementing worst-case robust optimization have been investigated:[124]

- **Composite worst-case optimization**: optimizes the single worst-case scenario (with respect to all objective functions) that can actually occur; this is the approach most relevant to this thesis
- **Objective-wise worst-case optimization**: optimizes the worst-case scenario for every objective function separately
- **Voxel-wise worst-case optimization**: optimizes the worst-case scenario for every volume element (voxel); since different scenarios may be optimized even for neighboring voxels within the same structure, this approach may optimize an unphysical dose distribution that will not actually be delivered in any one scenario

Comparison to the PTV and considered uncertainties
Although robust optimization and the PTV are two alternate ways of accounting for the same types of uncertainties, the former has been shown to achieve superior target coverage, dose homogeneity, and OAR sparing than PTV-based treatment planning.[125,126] Robust optimization commonly accounts for positional and/or range uncertainties, but approaches to include other sources of uncertainty are also under investigation. These include RBE deviations from the constant value of 1.1 currently used clinically as well as changes in patient anatomy.[127–129]

2.2.2 Range uncertainty reduction approaches at the treatment planning stage

A variety of different approaches to reduce proton range uncertainties are currently under investigation. At the treatment planning stage, such efforts focus on reducing uncertainties stemming from the conventional SECT treatment planning scan. Range uncertainty reduction techniques at the treatment planning stage mainly focus on Dual-Energy Computed Tomography (DECT) and imaging using protons rather than photons.

Dual-energy computed tomography (DECT)

As discussed in the beginning of Section 2.2, conventional proton therapy treatment planning relies on SECT, with SPR values relative to water being determined based on a piece-wise linear fit of CT numbers and SPRs.[77] The relationship between CT number and SPR is not, however, always unambiguous, and tissue compositions can be patient-specific.[110,111] Some of this ambiguity can be resolved by combining multiple sources of information, thereby reducing proton range uncertainties. This can for example take the form of two CT scans acquired with two different tube voltages. DECT scans can be acquired sequentially on a standard CT scanner, but this approach is susceptible to timing-related issues such as patient motion.[130] However, systems designed to be capable of DECT have been commercially available since at least the mid-2000s.[131] Such systems can rely on a variety

of different technologies, including fast switching between different X-ray tube potentials, multiple X-ray source-detector pairs, and a detector with multiple layers to separate the detection of low- and high-energy photons.[132]
The benefits of DECT-based treatment planning have been investigated in homogeneous samples as well as in realistic, inhomogeneous geometries.[133–137] Clinical implementation of DECT-based proton treatment planning has also already been reported.[138] DECT has been shown to be able to reduce a current clinical range uncertainty of 3.5% + 2 mm, which was based on a conventional SECT-based approach, to 1.7% + 2 mm for brain cancer patients and 2.0% + 2 mm for prostate cancer patients.[138]

Proton radiography and proton computed tomography (pCT)

Range uncertainties in proton therapy may alternatively be reduced through proton-based imaging, as this renders the conversion of photon-based images to proton SPRs superfluous.[139,140] Proton imaging approaches such as proton Computed Tomography (pCT) require protons of a sufficiently high energy to fully traverse the patient so that the residual energy can be detected downstream and SPR maps can be determined based on the energy lost during transmission. Early studies comparing pCT to photon-based SECT reported a dosimetric advantage at the cost of a reduction in spatial resolution.[141,142] Dosimetric benefits mainly result from a high detection efficiency and the maximum dose deposition in the Bragg peak, which is placed beyond the patient, while a loss in spatial resolution is especially the result of multiple Coulomb scattering.
A variety of different prototypes for proton radiotherapy and pCT have seen development over the years. Results of scans of a range of tissue-mimicking samples and different phantoms have been reported.[143,144] The feasibility of proton imaging has therefore been established. A recent study comparing SPRs of tissue-mimicking samples determined using pCT and DECT reported higher accuracy for pCT-based SPRs.[145]

2.2.3 Range verification approaches

While range uncertainties can be considered at the treatment planning stage, verification of the *in vivo* proton range is also possible, potentially in real time. Proton range verification approaches rely on measurements conducted during treatment delivery or shortly thereafter, and can be based on PET, imaging of prompt gamma-rays emitted during patient irradiation, or acoustic methods, among others.[146]

Positron emission tomography (PET)

Proton irradiation partially results in nuclear reactions with irradiated tissues, leading to the creation of positron-emitting nuclei such as ^{11}C and ^{15}O which can be used to verify the *in vivo* proton range (cf. Section 2.1.1).[147–149] The half-lives of relevant positron emitters which are created range from 2.0 minutes for ^{15}O to 20.4 minutes for ^{11}C.[150] The mean energy of the emitted positron is 0.7 MeV for ^{15}O and 0.4 MeV for ^{11}C, corresponding to a range in water of 3.0 mm and 1.2 mm, respectively.[151] Emitted positrons therefore traverse a short distance of tissue before an annihilation event with a nearby electron occurs, resulting in the emission of two annihilation photons of an energy of 511 keV, which are emitted under an angle of approximately 180°. Analogously to diagnostic PET imaging, these annihilation photons can be detected outside of the patient, and the coincidence between them can be used to determine the position from which they were emitted as a surrogate of the *in vivo* proton range.
Initial PET-based proton range verification efforts relied on an offline approach utilizing a PET scanner which is not located in the treatment room. However, offline PET-based range verification is particularly susceptible to biological washout between irradiation and PET image acquisition, which constitutes one of the main challenges of PET-based proton range verification.[152,153] In-room and even in-beam PET imaging systems have been developed since and are able to reduce the time in

which biological washout can occur and increase the measured signal and therefore decrease the imaging time.[154–156]

PET-based proton range verification has been investigated in different treatment sites and has been shown to be able to provide an accuracy of a few millimeters when using a prediction model which is either analytical or based on Monte Carlo simulations.[152,157,158] When comparing PET measurements for proton range verification which were acquired in different sessions, the reproducibility has been shown to be better than 1 mm.[156] In addition to biological washout, challenges for range verification based on PET imaging include patient and organ motion as well as uncertainties in relevant cross-sections and the knowledge of elemental compositions.[153,159]

Prompt gamma-ray imaging

Nuclear reactions resulting from proton irradiation further lead to excited nuclei, which undergo de-excitation through prompt gamma-ray emission within 1 nanosecond or less (cf. Section 2.1.1).[160] In proton therapy, the relevant targets for this process are mainly ^{12}C and ^{16}O.[11,12] Analogously to PET-based range verification, prompt gamma-rays emitted through de-excitation of excited nuclei in irradiated tissues can be detected outside of the patient for *in vivo* proton range verification. However, since de-excitation by prompt gamma-ray emission occurs almost instantaneously, prompt gamma-ray imaging can be used for real-time range monitoring and does not suffer from biological washout, which constitutes a considerable advantage over PET-based methods.[161]

Prompt gamma-ray imaging can be implemented in a variety of different ways. Detector systems can, for example, consist of scintillation detectors and a collimator with a knife-edge shaped slit or a multi-parallel slit design for detection of the spatial distribution of emitted gamma-rays.[162] Compton cameras instead generally rely on Compton scattering within one or multiple scatterers, often prior to detection in an absorber.[163,164] By measuring interaction positions as well as the deposited energy at the different stages, a cone (or arc, if the Compton electron is tracked) of possible directions of the initial gamma-ray can be determined. Superimposition of different Compton cones or arcs then allows the gamma-ray's initial direction to be narrowed down further.

Prompt gamma-ray timing utilizes the time it takes protons to traverse the patient until the irradiated target, which is on the order of 1-2 nanoseconds.[165] Since this time is dependent on depth, time-resolved prompt gamma-ray profiles can be used for proton range verification as long as the detection system has a sufficiently high temporal resolution.

The prompt gamma-ray imaging technique most relevant to this thesis is prompt gamma-ray spectroscopy, for which measurements will be presented in Chapter 5.[11,12] In contrast to the aforementioned techniques, prompt gamma-ray spectroscopy relies on measurements of the spectrum of emitted prompt gamma-rays for real-time proton range monitoring. The energy of prompt gamma-rays emitted through nuclear de-excitation depends on the underlying nuclear transitions. Furthermore, the cross-sections of these nuclear interactions are energy-dependent. Prompt gamma-rays emitted as a result of different nuclear transitions therefore differ in terms of their depth profile as well as their energy. As a result, the *in vivo* proton range can be deduced from the spectrum of prompt gamma-rays emitted during irradiation. Since gamma-ray energies are transition- and therefore target-dependent, prompt gamma-ray spectroscopy has the advantage of allowing elemental compositions of irradiated tissues to be determined alongside the proton range.

Studies of prompt gamma-ray imaging for proton range verification have been conducted in both phantoms and patients.[13,166–171] Measurements conducted with a knife-edge shaped slit camera during seven consecutive treatment fractions of a cancer patient with a head and neck tumor treated with passive scattering were reported in 2016.[168] A slit camera was also used for proton range verification during treatment fractions of a brain cancer patient, five prostate cancer patients, and a patient with a base of skull tumor treated with PBS.[169–171] Results thus far indicate that prompt gamma-ray-based proton range verification is able to provide millimeter accuracy, even for clinical fraction sizes and in realistic patient geometries.

Acoustic methods

In addition to positron and prompt gamma-ray emission, pulsed proton irradiation also results in the thermal expansion of the irradiated material or tissue which, in turn, leads to the emission of acoustic waves.[172,173] Use of this ionoacoustic effect for *in vivo* proton range verification is currently also under investigation. Measurements in water conducted using clinical particle accelerators - albeit in some cases with pulses which deviated from those currently used for clinical patient treatments - indicate that acoustic proton range verification may be feasible.[174,175] Simulation studies suggest that expanding acoustic range verification to heterogeneous media such as patient anatomies may be possible, for favorable indications.[176,177] Range verification based on the detection of acoustic waves emitted during irradiation by gold fiducial markers implanted near or into the tumor for patient positioning has also been suggested.[178,179] Since ultrasonic waves are detected for ionoacoustic proton range verification, co-registering such measurements with ultrasound imaging is also inherently possible.[180,181] Such a co-registration would constitute combining information on dose deposition (from ionoacoustic measurements) with anatomical information (from the ultrasound images).

2.2.4 Objectives of this thesis

Uncertainties in the *in vivo* proton range remain considerable hurdles in proton therapy. To account for such uncertainties, margins ranging from 2.5% + 1.5 mm to 3.5% + 3 mm are currently included during treatment planning.[4] However, this approach increases doses to organs-at-risk which are in close proximity to the target.

A variety of different approaches to reduce proton range uncertainties are therefore under investigation. DECT has been shown to be capable of reducing range uncertainties to 1.7% + 2 mm or 2.0% + 2 mm for brain and prostate cancer patients, respectively (cf. Section 2.2.2). In addition, range verification techniques like prompt gamma-ray imaging already report millimeter accuracy (cf. Section 2.2.3). A range uncertainty reduction to a level of 2% or even 1% may therefore eventually be achievable. This would considerably reduce the necessary margins considered during treatment planning. Such range uncertainty reductions would therefore also translate into reductions in doses to nearby organs-at-risk and associated toxicities.

The work presented in this thesis aims to support ongoing efforts to translate proton range verification into routine clinical practice by evaluating associated benefits for patients with brain or skull base tumors and validating the performance of the prompt gamma-ray spectroscopy system developed at MGH. Benefits of reductions in proton range uncertainties will be quantified under the assumption of current clinical practices (cf. Chapter 3) as well as taking into account novel proton therapy beam arrangements which may only become feasible once range uncertainties have been sufficiently reduced (cf. Chapter 4). The performance of the prompt gamma-ray spectroscopy detector prototype for proton range verification developed at MGH will then be verified using a variety of tissue-mimicking and porcine samples (cf. Chapter 5). By doing so, this thesis seeks to contribute to promoting proton range uncertainty reductions and thereby the fuller clinical exploitation of benefits associated with proton radiotherapy treatments for cancer.

CHAPTER 3

Direct benefits of proton range uncertainty reductions for cancer patients with clival tumors

The work described in this Chapter was conducted for the purpose of this thesis and published in a 2021 article in *Medical Physics*.[182] This Chapter's Figures were included in said article, either as they are or in an adapted form. Tables 3.1, 3.2, and 3.4 and Equations 3.4 and 3.5 were added to provide additional information, and the text was expanded upon for the same purpose.
The study presented in this Chapter quantifies the direct benefits of proton range uncertainty reductions for a set of ten cancer patients with clival tumors. The rationale for this work is laid out in Section 3.1. Information on the data set, treatment plan optimizations, and dose distribution calculations and evaluations is provided in Section 3.2. Section 3.3 quantifies range uncertainty reduction benefits, both in general terms and as a function of patient-specific parameters like target volume, prescription dose, and an organ-at-risk's proximity to the target. Section 3.4 discusses range uncertainty reduction benefit magnitudes, the effects of patient-specific factors, and additional considerations like the impact of the chosen beam arrangement. Section 3.5 concludes this Chapter and provides a brief outlook.

3.1 Motivation for quantifying range uncertainty reduction benefits

Even though more than sixty years have passed since the first patient treatment, proton therapy still faces considerable hurdles, out of which uncertainties in the *in vivo* proton range are among the most significant ones (cf. Section 2.2). Such uncertainties result from a variety of different sources, including the CT scan which is used to create a patient's clinical treatment plan, variations in patient setup, and changes in patient anatomy.[4] A multitude of different projects to reduce proton range uncertainties are currently being pursued (cf. Section 2.2.2 and Section 2.2.3). In current clinical practice, proton range uncertainties are often addressed using approaches which deliver suboptimal dose distributions in the nominal scenario in which no errors occur but are able to maintain target coverage and/or organ-at-risk sparing in a variety of error scenarios (cf. Section 2.2.1). This includes robust optimization, which allows planning constraints and objectives to be applied in error scenarios in addition to the nominal one.[124]
Robustness to higher levels of range uncertainty degrades dose conformality to the target. Doses to nearby organs-at-risk may increase as a result. Range uncertainty reductions result in improved dose conformality to the target and better sparing of nearby OARs. The potential benefits of range uncertainty reduction techniques can therefore be quantified in terms of the associated reductions in doses to organs-at-risk which are in close proximity to the target.

To the best of the author's knowledge, there were two previous studies which quantified OAR sparing as a function of range uncertainty, both of which focused on head & neck cases. A 2016 paper by Van de Water et al. quantified Normal Tissue Complication Probability (NTCP) as a function of setup error and range uncertainty for 20 oropharyngeal cases and came to the conclusion that setup error reductions should be prioritized over reductions in proton range uncertainties.[183] A 2021 study by Wagenaar et al. encompassed ten head & neck cases with a variety of tumor sites, including oropharynx, hypopharynx, nasopharynx, gingiva, and retromolar trigone.[184] Their study likewise quantified OAR doses and NTCPs as a function of setup and range error and observed larger changes as a function of setup error than range uncertainty. As is the case in the study presented in this Chapter, both works focused on IMPT and applied worst-case robust optimization.
Because of MGH's focus on range uncertainty reduction techniques - initially based on PET, more recently using prompt gamma-ray spectroscopy - NTCPs were quantified as a function of range uncertainties and there was no focus on the effects of changes in setup uncertainties.[13,152] The data set included treatment plans of ten skull base cancer patients with clival tumors, since, to the best of the author's knowledge, the effects of range uncertainty reductions had not yet been quantified for such patients. Clival tumors were also of particular interest due to their proximity to the brainstem, optic chiasm, and optic nerves, and the severity of the associated toxicities of brainstem necrosis and blindness which may result from this proximity.

3.2 Materials and methods

3.2.1 Patient data set

The study included treatment plans for ten skull base cancer patients with clival tumors who had previously received PBS proton therapy at MGH in Boston, Massachusetts, USA. The Treatment Planning System (TPS) used was MGH's in-house Astroid system.[185] All optimizations used the same planning constraints and objectives as the original treatment plan with which a given patient had been treated. The planning objectives used were:

- **Target structures:**
  - Maximize minimum dose
  - Maximize mean dose
  - Minimize underdose with respect to a specified threshold
- **Organs-at-risk:**
  - Minimize maximum dose
  - Minimize mean dose
  - Minimize overdose with respect to a specified threshold

The minimize underdose and minimize overdose objectives were used similarly to constraints on the minimum or maximum dose. However, planning constraints must be fulfilled, while planning objectives are only fulfilled as far as possible. Under- and overdose objectives therefore help achieve a similar goal as the corresponding constraints without the severity of a planning constraint, which may render an optimization infeasible. For a typical case, the location of the target structure and nearby organs-at-risk is shown in Figure 3.1.

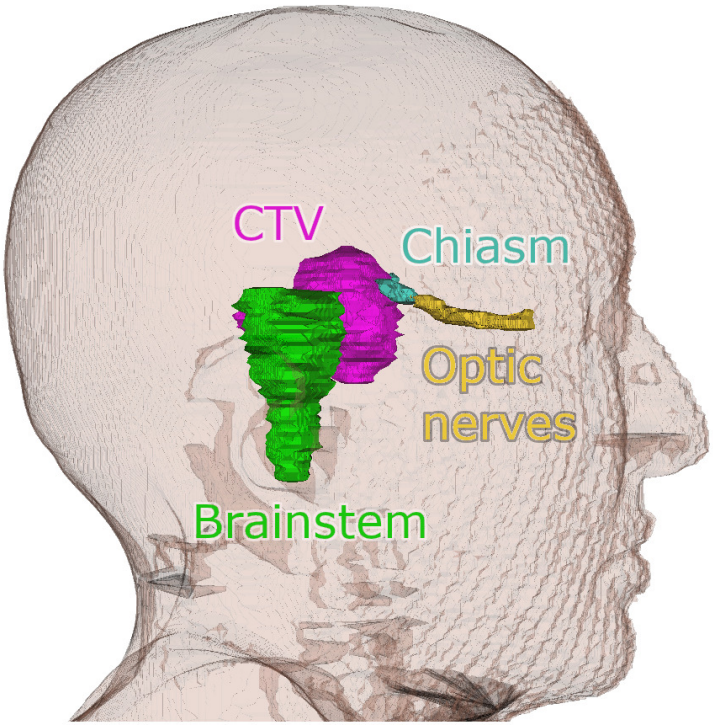

Figure 3.1: Clinical target volume (CTV) and nearby organ-at-risk positions for a patient with a clival tumor. Because of the shared treatment site, the target abutted the brainstem in all ten cases. The distance between the target structure and the optic chiasm and optic nerves depended on patient-specific factors such as exact target location and tumor volume.

Since all patient cases included in this study were selected based on their shared tumor location, the brainstem abutted the clinical target volume in all ten cases. The relevance of other OARs such as the optic chiasm and optic nerves, however, depended on patient-specific factors such as tumor location and size. Patient-specific aspects which were particularly relevant to this study included the volume of the target structure and the prescription dose. Table 3.1 contains target volume and prescription dose information for all ten cases included in this study.

Table 3.1: Patient-specific parameters for patients with clival tumors included in this study. V_{CTV} and $D_{pre,max}$ indicate the volume of the CTV and the highest dose prescribed to any part of the target, respectively.

Patient ID	V_{CTV} **[cm^3]**	$D_{pre,max}$ **[Gy(RBE)]**
1	17.6	50.0
2	64.9	58.2
3	16.6	70.0
4	13.3	62.0
5	29.7	54.0
6	12.4	72.0
7	25.4	76.0
8	22.7	75.6
9	35.2	76.0
10	8.2	76.0

3.2.2 Treatment plan optimization

Six robust optimizations were performed for every patient. All optimizations included robustness to setup errors of ± 2 mm in every dimension (seven scenarios) as well as robustness to range uncertainties of 0-5%, in increments of 1% (three scenarios: nominal, overshoot, and undershoot). Throughout this work, scenario refers to situations in which a setup and/or range error occurs as well as to the nominal scenario in which this is not the case. A setup error margin of 2 mm was considered to be realistic by the time range uncertainty reduction techniques may see clinical implementation.[184] Scenarios in which setup and range errors occurred simultaneously were included in the optimizations so that the interplay between different sources of error could be considered. A total of 21 scenarios were included in the optimizations (21 scenarios = 7 setup error scenarios x 3 range error scenarios). In the case of the 0% range uncertainty robustness treatment plans, optimizations only included seven scenarios because of the lack of over- and undershoot scenarios.
As is the norm, setup and range errors were simulated through isocenter shifts and uniform scaling of the HU values in the patient CT, respectively.[183,184] Overshoot and undershoot scenarios are defined as range error scenarios in which the HU scaling factor was smaller than 1.0 and greater than 1.0, respectively. All fluence optimizations were performed using the Nymph optimizer, a primal-dual infeasible interior point algorithm.[186,187] Nymph guarantees a solution after a number of iterations in the order of $\sqrt{n} \times ln(\frac{1}{\epsilon})$, where n is the dimension of the problem and ϵ is the distance from the global optimum. For this study, ϵ = 0.1 Gy(RBE) was used for all optimizations, meaning that the algorithm would stop when the objective value was at most 0.1 Gy(RBE) from the optimum. Nymph's run time is approximately linearly proportional to the number of voxels, and it solves convex optimization problems by reducing the Newton equations to a linear system containing spot weights and objective values.
Nymph determines the weights of all proton pencil-beam spots x using the planning constraints c, the planning objectives f, and the vector of D matrices for every scenario D as inputs:

$$x = x(c, f, D). \tag{3.1}$$

For scenario s, the matrix element D_{ij}^{s} denotes the dose deposited in voxel i per unit of fluence from proton pencil-beam j.
Since planning constraints must be fulfilled, it was not necessary to implement a manner of prioritization of different planning constraints or constraints from different scenarios. All constraints for all scenarios could simply be contained by a single vector c. Planning objectives, on the other hand, are only fulfilled as far as possible, according to their relative importance. Planning objectives from different scenarios were therefore implemented using composite worst-case optimization:[124]

$$\min_{x \geq 0} \max_{s \in S} \sum_{i=1}^{n} \omega_i f_i(d(x; s)) : c(x) \leq 0, \tag{3.2}$$

where f_i is an objective function with weight ω_i, and d is the resulting dose distribution. In composite worst-case optimiziation, the single worst-case scenario is optimized, and the worst-case scenarios for different objectives or voxels are not considered separately. All target constraints and objectives were applied in all scenarios. To indicate the associated computational burden, Table 3.2 contains the number of variables and constraints for the 0% range uncertainty robustness treatment plans of all ten patients.
IMPT was applied throughout this study. Field-wise dose distributions were therefore allowed to be non-uniform as long as the uniformity of the total dose distribution was maintained (cf. Section 2.1.5).[82,85] Target coverage was kept consistent between all levels of range uncertainty robustness and all scenarios, and clinical planning constraints assured that the maximum dose did not exceed 106% of the prescription dose in any of the cases. Dose hot spots therefore did not pose an issue, and a potential trade-off between the maximum dose to the target and normal tissue doses did not have to

Table 3.2: Variables and constraints for patients with clival tumors included in this study. Values concern the 0% range uncertainty robustness treatment plans. Due to the higher number of scenarios, the numbers of variables and constraints for treatment plans optimized using higher levels of range uncertainty were higher than the values shown in this Table.

Patient ID	# of variables [x10^3]	# of constraints [x10^3]
1	157.1	585.8
2	61.1	462.9
3	98.3	957.4
4	21.0	363.8
5	359.9	1310.2
6	20.9	582.0
7	278.5	654.7
8	92.9	377.9
9	31.5	351.7
10	30.7	696.2

be taken into account.[188]
All optimizations used the machine model of the ProTom Radiance 330 system as installed in MGH's recently opened Gordon-Browne Proton Therapy Center. For this model, the proton spot size in air ranged from about $\sigma = 7$ mm at a proton energy of 70 MeV to about $\sigma = 3.5$ mm at 230 MeV. Use of a modern machine model was necessary because the techniques which may achieve the range uncertainty reductions studied may only see clinical implementation in a few years.

3.2.3 Dose distribution calculation and evaluation

All scenarios included in the optimization were evaluated, with dose distributions being calculated according to the pencil-beam algorithm developed by Hong et al.[90] To account for differences between proton and photon irradiation, dose calculations assumed a constant RBE value of 1.1, as is the norm in current clinical practice (cf. Section 2.1.2). For a given scenario, the dose distribution d_s resulted from multiplying the D matrix with the vector of pencil-beam spot weights:

$$d_s = D^s x. \tag{3.3}$$

Target coverage metrics were determined to assure that the target coverage was consistent between all levels of range uncertainty robustness and in all scenarios. The normal tissue volume receiving at least 70% of the prescription dose was determined to quantify dose conformality to the target and to provide a general normal tissue dose metric. Doses to organs at risk were evaluated in terms of the normal tissue complication probability - i.e., the probability of organ-specific toxicities arising as a result of the organ being irradiated with the dose in question. NTCPs were calculated using the Lyman-Kutcher-Burman (LKB) model:[189]

$$\mathrm{NTCP} = \frac{1}{\sqrt{2\pi}} \int_{-\infty}^{t} e^{-\frac{t'^2}{2}} dt', \tag{3.4}$$

where $t = \frac{D - \mathrm{TD}_{50}(v)}{m\mathrm{TD}_{50}(v)}$, in which m is the slope of the curve depicting NTCP as a function of dose and $v = \frac{V}{V_{ref}}$ is the fraction of the OAR that is being irradiated. Furthermore, TD_{50} is the tolerance dose corresponding to an NTCP value of 50%, and $\mathrm{TD}(v) = \frac{\mathrm{TD}(1)}{v^n}$, where n is the volume-dependence of the NTCP which is determined via the NTCP changes observed for different values of v. For this work, the dose delivered to the OAR was modeled as the entire OAR being irradiated with

the same effective dose D_{eff}, as suggested by Mohan et al.:[190]

$$D_{eff} = (\sum_i \Delta V_i (D_i)^{\frac{1}{n}})^n, \tag{3.5}$$

where D_i is the dose delivered to volume element ΔV_i.

NTCPs were calculated for all OARs within 1 cm of the CTV. OARs which were located further than 1 cm from the target were not considered in the evaluation as they were regarded as irrelevant to the range uncertainties studied. This proximity criterion was fulfilled by the brainstem in all cases and by the optic chiasm in six cases (Patient 1 to Patient 6). OARs that were only relevant in a single or a few cases will not be discussed. The LKB model parameters used for the different OARs are shown in Table 3.3.

Table 3.3: LKB model parameters for the OARs relevant to this study. The parameters n and m describe the NTCP's volume-dependence and the slope of the curve depicting NTCP as a function of dose, respectively. The parameter TD50 is the tolerance dose at which an NTCP of 50% is observed.

Organ-at-risk	**Endpoint**	**n**	**m**	**TD50 [Gy(RBE)]**
Brainstem	Necrosis	0.16	0.14	65.0
Optic chiasm	Blindness	0.25	0.14	72.0

Burman et al. originally determined a value of TD50 = 65 Gy(RBE) for the optic chiasm, but later studies suggested values of 70 Gy(RBE), 72 Gy(RBE), and 75 Gy(RBE), and a value of TD50 = 72 Gy(RBE) was chosen in an attempt to compromise between the findings of these studies.[189,191,192]

The clinical range uncertainty margin is institution-dependent, with values currently spanning from 2.5% + 1.5 mm to 3.5% + 3 mm.[4,193] This study approximated the clinical range uncertainty margin as 4%. Range uncertainty reduction techniques, on the other hand, already report millimeter accuracy.[13,168] The potential benefits of range uncertainty reductions can therefore be quantified in terms of the NTCP and normal tissue dose decreases resulting from a range uncertainty reduction from 4% to 1%.

3.3 Results

3.3.1 Overview over range uncertainty reduction benefits

Figure 3.2 depicts the brainstem NTCP with the endpoint of brainstem necrosis, the optic chiasm NTCP with the endpoint of blindness, and the normal tissue volume receiving at least 70% of the prescription dose for all patients for whom the metric was considered relevant. As anticipated, NTCPs and general normal tissue metrics generally increased with range uncertainty.

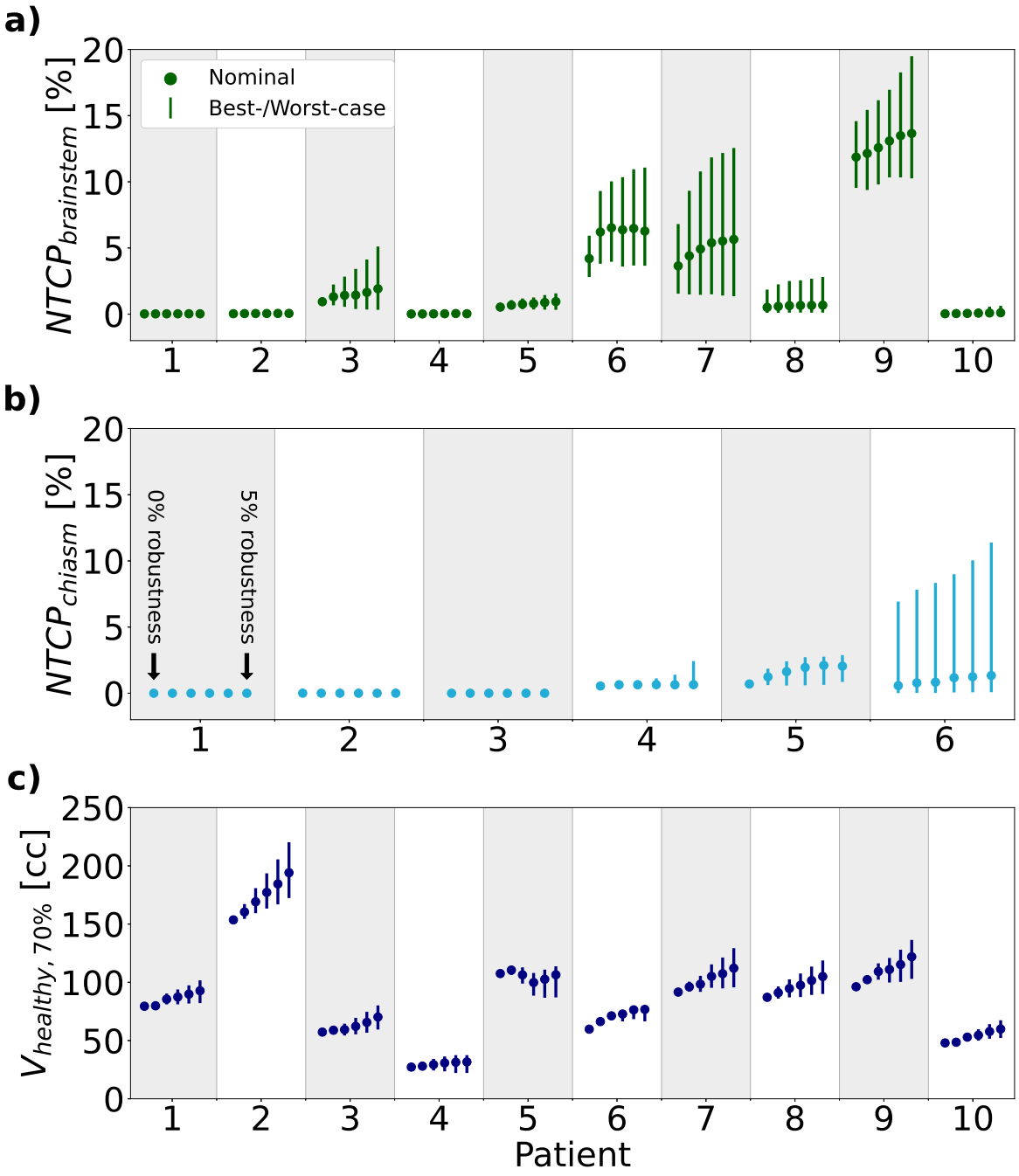

Figure 3.2: Normal tissue metrics in terms of the NTCP for the (a) brainstem (endpoint: brainstem necrosis) and (b) optic chiasm (endpoint: blindness) as well as (c) the volume of normal tissue receiving at least 70% of the prescription dose as a function of range uncertainty. Data points depict values in the nominal scenario while error bars indicate values in the best- and worst-case scenario. The lower number of cases shown in (b) resulted from an OAR only being considered relevant in cases in which it was within 1 cm of the target.

3.3.2 Patient-specific factors indicating range uncertainty reduction benefits

For different OARs, observed range uncertainty reduction benefits depended on a variety of patient-specific factors.

Brainstem

A range uncertainty reduction from 4% to 1% was accompanied by brainstem NTCP reductions of up to 1.3 percentage points in the nominal scenario and 2.9 percentage points in the worst-case scenario. The patient-specific factor most relevant to the brainstem NTCP reduction observed in a given case was the highest dose prescribed to any part of the target. In terms of the associated changes in brainstem NTCP, range uncertainty reduction benefits as a function of prescription dose are shown in Figure 3.3.

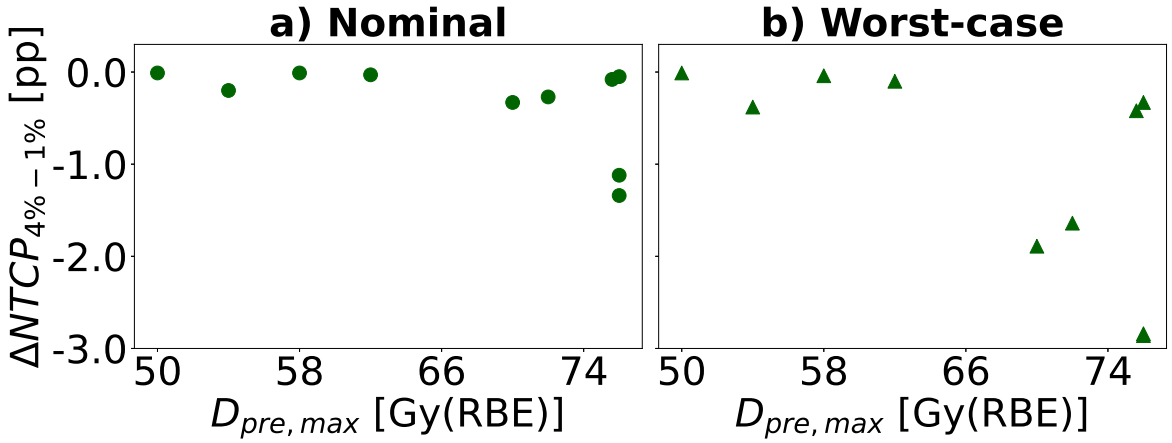

Figure 3.3: Range uncertainty reduction benefits in terms of the brainstem NTCP reduction caused by reducing range uncertainties from 4% to 1% as a function of prescription dose in the (a) nominal and (b) worst-case scenario. $D_{pre,max}$ refers to the highest dose prescribed to any part of the target. For each scenario, every data point represents one patient. The unit pp refers to percentage points.

As shown in Figure 3.3, brainstem NTCP reductions greater than 0.4 percentage points were only observed in cases in which the highest prescription dose to any part of the target was at least 70 Gy(RBE). However, even in such cases, range uncertainty reduction benefits varied, largely depending on the fraction of the target volume receiving the highest prescription dose. Table 3.4 shows the amount of target volume receiving the highest prescription dose as well as the brainstem NTCP reductions observed for the six cases in which a dose of at least 70 Gy(RBE) was prescribed to any part of the target.

Optic chiasm

Figure 3.4 depicts range uncertainty reduction benefits as a function of distance between optic chiasm and target for the six cases in which the optic chiasm was within 1 cm of the target. A range uncertainty reduction from 4% to 1% lowered the optic chiasm NTCP with the endpoint of blindness by up to 0.9 percentage points in the nominal scenario and by up to 2.2 percentage points in the worst-case scenario.

Table 3.4: Target parameters for patients with clival tumors. $D_{pre,max}$ and $V_{pre,max}$ denote the highest dose prescribed to any part of the target and the volume receiving this prescription dose, respectively. Values are provided for the six cases in which $D_{pre,max} \geq 70.0$ Gy(RBE). Cases are ordered according to descending $V_{pre,max}$. $\Delta NTCP_{4\%-1\%}$ indicates the brainstem NTCP reductions achieved in the nominal and worst-case scenario by reducing range uncertainties from 4% to 1%. The lowest reductions in brainstem NTCP were observed in the two cases in which $V_{pre,max}$ was particularly small.

Patient ID	$V_{pre,max}$ **[cc]**	$D_{pre,max}$ **[Gy(RBE)]**	$\Delta NTCP_{4\%-1\%}$ **[pp]**	
			Nominal	**Worst-case**
7	15.6	76.0	1.1	2.9
6	12.4	72.0	0.3	1.6
9	10.0	76.0	1.3	2.8
3	9.0	70.0	0.3	1.9
8	5.7	75.6	0.1	0.4
10	4.7	76.0	0.1	0.3

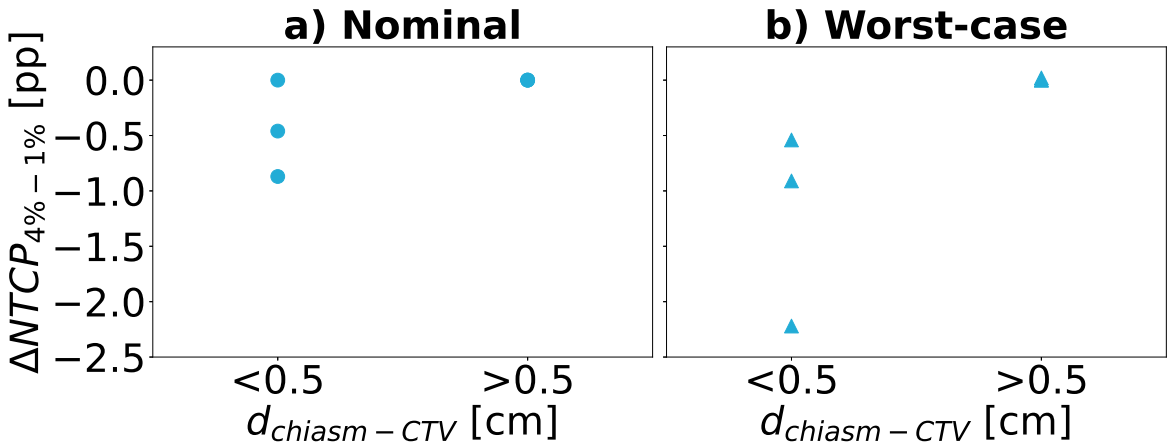

Figure 3.4: Range uncertainty reduction benefits in terms of the reduction in optic chiasm NTCP (endpoint: blindness) as a function of the distance between optic chiasm and target for the six cases in which the optic chiasm was within 1 cm of the target in the (a) nominal and (b) worst-case scenario.

As reflected in Figure 3.4, the only cases in which changes in optic chiasm NTCP were observed were those in which the optic chiasm was within 0.5 cm of the CTV. Large variations in NTCP observed in patient 6 were explained by the high dose of 72.0 Gy(RBE) which was prescribed to 12.4 cubic centimeters of target volume.

General normal tissue

A 4% to 1% range uncertainty reduction was accompanied by a reduction in the volume of normal tissue receiving at least 70% of the prescription dose of up to 24.1 cubic centimeters in the nominal scenario and 38.4 cubic centimeters in the worst-case scenario. The main factor indicating the magnitude of the benefit that was observed in a given case was the volume of the target structure. For all patients, the effects of a 4% to 1% range uncertainty reduction as a function of target volume are shown in Figure 3.5

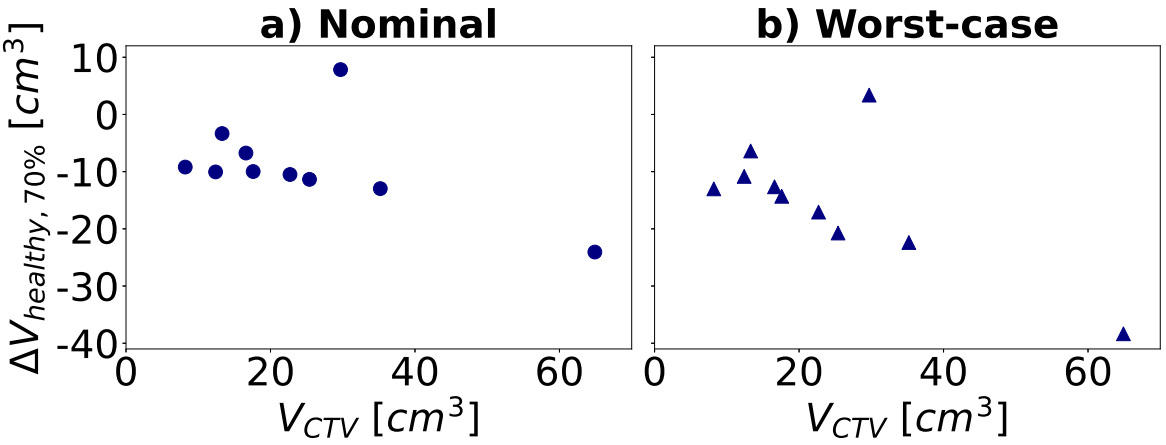

Figure 3.5: Range uncertainty reduction benefits in terms of changes in the volume of normal tissue receiving at least 70% of the prescription dose as a function of target volume in the (a) nominal and (b) worst-case scenario.

3.4 Discussion

3.4.1 Benefits and relevance of range uncertainty reductions

Even though the study presented in this Chapter quantified the potential benefits of range uncertainty reductions as the NTCP and normal tissue dose reductions achieved by reducing range uncertainties from 4% to 1% (cf. Section 3.3.2), changes in NTCPs and normal tissue doses were observed between all levels of range uncertainty. Range uncertainty reductions smaller than three percentage points may therefore also be beneficial.

Previous studies suggested that the benefits of setup error reductions may exceed the benefits of reducing proton range uncertainties. Based on 20 oropharyngeal cases, van de Water et al. reported that a setup error reduction from 3 mm to 1 mm resulted in an average NTCP reduction of 1.9 percentage points, compared to 0.4 percentage points for a range uncertainty reduction from 3% to 1%.[183] Wagenaar et al. reported similar findings based on a set of ten head & neck cases, five of which were also oropharyngeal. They reported a 2.0% NTCP decrease per mm reduction in setup margin, compared to a 0.9% change in NTCP per percentage point of range uncertainty reduction.[184]

Since this study focused on a different treatment site and different OARs than the aforementioned works, a direct comparison is not possible. Because of the focus on range uncertainties specifically, it cannot be commented on whether reductions in setup error robustness would have been associated with smaller or larger benefits than reductions in proton range uncertainties for the cases studied. However, the quantified changes in NTCPs as function of range uncertainty do indicate marked range uncertainty reduction benefits. The results of this study are especially to be viewed under consideration of the severity of the evaluated endpoints of brainstem necrosis and blindness.

3.4.2 Patient-specific factors indicating range uncertainty reduction benefits

Range uncertainty reduction benefits observed in a given case were generally linked to a variety of patient-specific parameters. The importance of patient-specific factors differed between the three evaluated metrics.

Brainstem

Marked changes in brainstem NTCP were only observed in cases in which the highest dose prescribed to any part of the target was at least 70 Gy(RBE). This was partially the result of the comparatively large size of the brainstem, which was generally larger than or at most of equal size as the CTV. This

resulted in a large part of the brainstem receiving no or little dose. The dose delivered to the irradiated part of the brainstem therefore had to be comparatively high for changes in brainstem NTCP to be observed.
This was, however, generally not the case. The tolerance dose used in the underlying LKB model was TD50 = 65 Gy(RBE), which is to say that the entire brainstem would have to be irradiated with a dose of 65 Gy(RBE) in order for an NTCP of 50% to be observed. However, in most cases, this tolerance dose was high compared to the prescription dose, causing the brainstem NTCP to remain at or near 0% at all levels of range uncertainty. Only when the prescription dose was sufficiently high were changes in brainstem NTCP observed. Even in such cases, the portion of the CTV to which a dose of at least 70 Gy(RBE) was prescribed may have been small, with the remainder of the CTV being prescribed a dose of around 50 Gy(RBE). The highest changes in brainstem NTCP were observed in cases in which the portion of the CTV with a prescription dose of at least 70 Gy(RBE) was comparatively large. In terms of brainstem sparing, range uncertainty reductions were therefore especially beneficial in cases with high prescription doses, with the volume to which this high dose was prescribed also being a factor. The brainstem abutted the target in all ten cases, so proximity to the target was not sufficient to indicate range uncertainty reduction benefits in terms of changes in brainstem NTCP.

Optic chiasm

The distance between OAR and target played a much greater role in helping predict benefits in terms of sparing of the optic chiasm. Changes in optic chiasm NTCP with the endpoint of blindness were only observed in cases in which the optic chiasm was within half a centimeter of the CTV. This was because the optic chiasm received no or little dose in cases in which it was further than 0.5 cm from the target, resulting in an NTCP of 0% at all levels of range uncertainty. When the optic chiasm was within half a centimeter of the CTV, on the other hand, the dose it received was generally sufficient for changes in NTCP to be observed. The volume of the optic chiasm was smaller than or equal to 0.7 cubic centimeters in all cases, so the irradiated OAR volume did not have to be large for changes in NTCP to be observed.
Prescription dose also played a role, with the largest changes in optic chiasm NTCP being observed in a case in which the highest dose prescribed to any part of the target was 72.0 Gy(RBE). This was the result of the comparatively high tolerance dose used in the underlying LKB model, which was TD50 = 72.0 Gy(RBE). For a prescription dose of 50.0 Gy(RBE) - the lowest prescription dose included in this study - these parameters would translate into an NTCP of only 1.5% even if the entire optic chiasm was irradiated with the prescription dose.

General normal tissue

In terms of the normal tissue volume receiving at least 70% of the prescription dose, the benefits of range uncertainty reductions generally increased with the volume of the CTV. As this metric was only used to quantify dose conformality and general normal tissue doses, this pattern was anticipated. In terms of general normal tissue sparing, range uncertainty reductions were therefore especially beneficial in cases with larger target structures.

3.4.3 Effects of the clinical beam arrangement

Another patient-specific aspect which influenced range uncertainty reduction benefits observed in a given case were the beam angles chosen for a patient's clinical beam arrangement. To help explain this effect, Figure 3.6 depicts the dose distributions for two plans that are not robust to any range uncertainties as well as the changes in dose distributions resulting from increasing range uncertainty robustness from 0% to 5%. Both cases were comparable in terms of target size and doses prescribed to the higher- and lower-dose part of the target.
However, as shown in Figure 3.2, Patient 3 exhibited much larger changes in brainstem NTCP as a

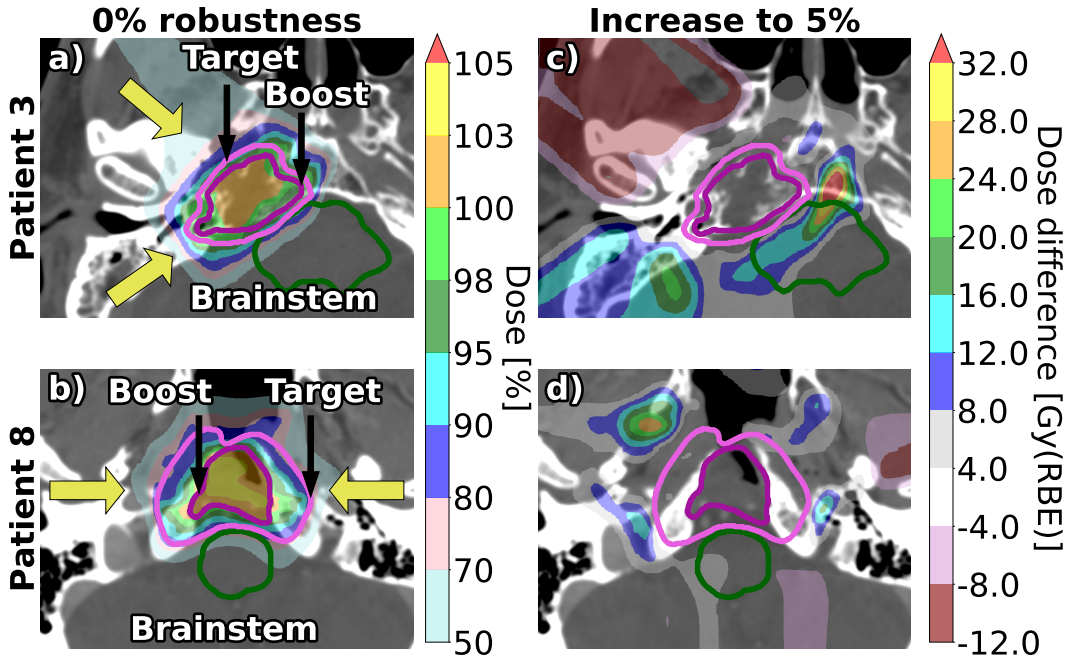

Figure 3.6: Dose distributions and beam arrangements for Patient 3 and Patient 8. Dose distributions are depicted for (a,b) treatment plans not robust to any range uncertainties and (c,d) the dose increases caused by increasing range uncertainty robustness from 0% to 5%. All dose distributions depicted concern the nominal scenario, and yellow arrows indicate beam directions.

function of range uncertainty robustness. Figure 3.6 helps explain why this was the case: the clinical beam arrangement for Patient 3 utilized the sharper dose fall-off at the distal proton beam edge to conform the dose distribution to the brainstem. Increasing range uncertainty robustness caused additional dose to be "pushed" into the brainstem. In the case of Patient 8, greater use was made of the shallower dose fall-off at the lateral beam edge to conform the dose distribution to the brainstem. As the effects of range uncertainties are limited to the beam directions, an increase in range uncertainty robustness did not cause additional dose to be delivered to the brainstem in this case, causing the brainstem NTCP to be largely unaffected by changes in range uncertainty.

Current clinical beam arrangements frequently utilize conservative beam arrangements making greater use of the lateral rather than the distal beam edge to conform the dose distribution to nearby OARs to reduce the potential effects of range uncertainties.[10] This effect was therefore anticipated. However, as proton range uncertainties are reduced, novel beam arrangements making greater use of the sharper dose fall-off at the distal beam edge may become feasible. Due to the effect outlined above, this may increase the benefits of further range uncertainty reductions and will be addressed in the next Chapter.

3.4.4 Additional considerations

Neither evaluated NTCPs nor the volume of normal tissue receiving at least 70% of the prescription dose were optimized directly. Optimizations included objectives to reduce the mean and/or maximum doses to OARs and general normal tissue, and reductions in OAR and normal tissue metrics were generally observed as range uncertainty was reduced, but small, counter-intuitive changes in these metrics between range uncertainty levels were nevertheless possible. Furthermore, considerable uncertainties in LKB model parameters also translate into uncertainties in calculated NTCPs. The parameters used to calculate brainstem NTCPs, for example, may be conservative, potentially leading to elevated brainstem NTCP values.[194]

A constant RBE value of 1.1 was applied for all dose calculations. This approach was chosen be-

cause it is in line with current clinical practice. Variable RBE models are, however, being studied as well.[42–45] Since variable RBE models exhibit an increase in RBE in high-LET regions like the distal beam edge, such models may have a considerable effect on the doses to some OARs which are in close proximity to the target.

3.5 Conclusion and outlook

The direct benefits of range uncertainty reductions were quantified based on a set of treatment plans for ten skull base cancer patients with clival tumors. Particularly high brainstem NTCP reductions were observed in cases in which the highest dose prescribed to any part of the target was at least 70 Gy(RBE). In terms of sparing of the optic chiasm, range uncertainty reduction benefits were observed in all cases in which the optic chiasm was within half a centimeter of the target, and were particularly high in the case with the highest prescription dose. General normal tissue benefits increased as a function of target volume. Range uncertainty reduction benefits were observed between all levels of range uncertainty, so range uncertainty reductions of any magnitude may be beneficial.
The chosen clinical beam angles had a considerable impact on the magnitude of the range uncertainty reduction benefits observed in a given case. Cases which generally utilized the less steep dose fall-off at the lateral beam edge to conform the dose distribution to nearby OARs, as is commonly done in clinical practice to reduce the potential effects of range uncertainties, generally exhibited smaller benefits. Cases which made greater use of the sharper dose fall-off at the distal beam edge, on the other hand, generally exhibited higher benefits. As proton range uncertainties are reduced, such beam arrangements will become increasingly feasible, in turn potentially increasing the benefits of further range uncertainty reductions. This effect will be addressed in the next Chapter.

CHAPTER 4

Benefits of novel beam arrangements made feasible by reducing proton range uncertainties

This study was conducted for the purpose of this thesis and was published in a 2022 article in *Medical Physics*.[195] Figures 4.1, 4.3, 4.5, 4.6, and 4.7 and Tables 4.2 and 4.3 were contained in the aforementioned article. The text was re-written for clarity and to provide additional information, and all remaining Figures and Tables were added for the same purpose.
This study quantifies the benefits of novel proton therapy beam arrangements made feasible by reductions in proton range uncertainties. Section 4.1 explains the importance of considering indirect range uncertainty reduction benefits like the feasibility of novel beam arrangements in addition to the direct benefits of reducing range uncertainties. Section 4.2 provides information on the data set used, the treatment plan optimization and evaluation methodology, and the Monte Carlo simulation workflow. Range uncertainty reduction benefits are quantified in Section 4.3, both in general terms and as a function of patient-specific parameters like prescription dose. The feasibility and importance of novel beam arrangements, the impact of patient-specific parameters, and radiobiological effects at the proton end-of-range are discussed in Section 4.4, and Section 4.5 concludes this Chapter and provides a brief outlook.

4.1 Motivation for investigating novel beam arrangements

Uncertainties in the *in vivo* proton range remain considerable hurdles for proton therapy, and various projects to reduce range uncertainties are therefore currently being pursued (cf. Section 2.2.2 and Section 2.2.3).[4] The potential benefits of such projects have been quantified previously, including in the study presented in Chapter 3.[182–184] However, such studies have generally worked under the assumption of current clinical practices. This includes the use of traditional clinical beam arrangements. Such beam arrangements are, however, generally conservative.[10] The dose fall-off at the distal proton beam edge is considerably steeper than the dose fall-off at the lateral edge. In cases in which the target is in close proximity to an organ-at-risk, conforming the dose distribution to the target using the steep dose fall-off at the distal beam edge would therefore allow for a sharper dose gradient at the target-OAR interface. In the absence of setup and range uncertainties, this approach would improve OAR sparing.
Greater reliance on the distal beam edge is also, however, more susceptible to uncertainties in the *in vivo* proton range. As discussed previously, the effects of range uncertainties are limited to the proton beam direction. In overshoot scenarios, for example, additional dose is delivered beyond the intended target structure. If the distal proton beam edge was used to conform the dose distribution to the target, this would lead to additional dose being "pushed" into any OARs located behind the target. In order

to reduce the potential effects of range uncertainties, traditional proton therapy beam arrangements generally make greater use of the less steep dose fall-off at the lateral beam edge to conform the dose distribution to OARs abutting the target.[10] This reduces the potential effects of range uncertainties while compromising OAR sparing in the nominal and some error scenarios.
However, as proton range uncertainties are reduced, so are their potential effects. At sufficiently low levels of range uncertainty, novel beam arrangements making greater use of the distal beam edge to conform the dose distribution to the target will become feasible. To the best of the author's knowledge, previous studies largely focused on the direct benefits of range uncertainty reductions in terms of associated OAR and general normal tissue sparing.[182–184] However, indirect benefits such as the feasilibity of novel beam arrangements at lower levels of range uncertainty also have to be taken into account. For the study presented in this Chapter, direct and indirect benefits of range uncertainty reductions were therefore quantified for a set of treatment plans for ten cancer patients with skull base or brain tumors.

4.2 Materials and methods

4.2.1 Patient data set

The data set consisted of IMPT treatment plans for ten cancer patients with skull base or brain tumors. The data set included patients with suprasellar, posterior fossa, and clival tumors who had received PBS proton therapy at MGH in Boston, Massachusetts, USA. Since this study focused on range uncertainty reduction benefits in terms of brainstem sparing, only cases in which the target structure was in close proximity to the brainstem were included. For all ten patients, the target volume and prescription dose are shown in Table 4.1. The TPS used was MGH's in-house Astroid system.[185]

Table 4.1: Target parameters for patients with brain or skull base tumors included in this study. V_{CTV} and $D_{pre,max}$ refer to the volume of the CTV and the highest dose prescribed to any part of the target, respectively.

Patient ID	$\boldsymbol{V_{CTV}[cm^3]}$	$\boldsymbol{D_{pre,max}}$ **[Gy(RBE)]**
1	6.2	50.4
2	17.2	51.0
3	64.5	50.4
4	33.9	52.2
5	38.9	54.0
6	42.7	54.0
7	34.1	70.0
8	65.3	54.0
9	63.4	54.0
10	69.2	55.8

4.2.2 Beam arrangement definitions

Two beam arrangements were considered for every case included in this study:

- The **traditional clinical beam arrangement** with which a given patient had been treated
- A **novel beam arrangement** making greater use of the steep dose fall-off at the distal beam edge to conform the dose distribution to the target

For every case, an initial novel beam arrangement was defined based on its reliance on the distal beam edge. The novel beam arrangement consisted of the same number of treatment fields as the

traditional clinical beam arrangement. During beam angle selection, care was taken to maintain a comparable separation between gantry angles to avoid overlap between doses delivered from different directions, which may result in an increase in the volume of normal tissue receiving a high dose. Other considerations which were relevant to the definition of the novel beam arrangement were:

- **Doses to nearby organs-at-risk** other than the brainstem were required to be comparable for both beam arrangements; especially relevant in this regard were the cochlea and the temporal lobes, but this also included the general dose to the brain
- A potential reduction in the **path length of brain exposure**
- Avoiding **air cavities** such as the ones in the mastoid region

After an initial novel beam arrangement had been defined, optimizations which included robustness to setup errors of ±2 mm and range uncertainties of 4% were performed for both beam arrangements. If the initial novel beam arrangement was found to create an unintended trade-off between the dose to the brainstem and doses to other OARs, the initial novel beam arrangement was adapted, and the optimization was re-run. For two cases, the traditional and novel beam arrangement are shown in Figure 4.1.

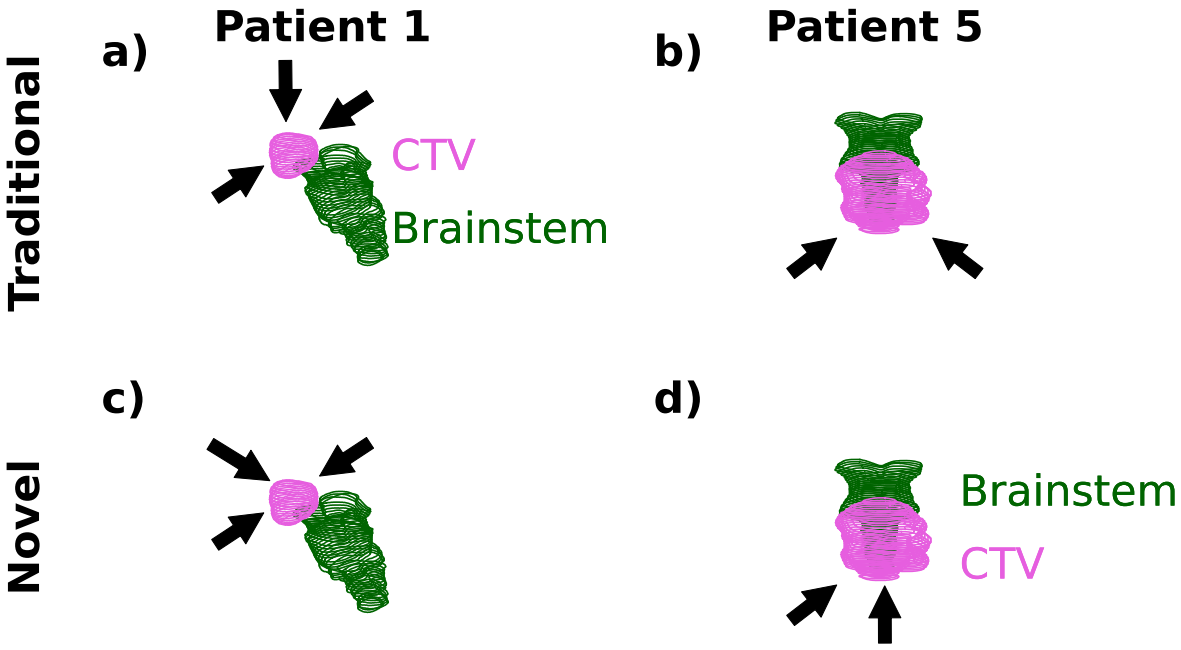

Figure 4.1: Traditional and novel beam arrangements for (a,c) Patient 1 and (b,d) Patient 5. The clinical target volume and brainstem are shown in pink and green, respectively. Arrows indicate beam directions.

4.2.3 Treatment plan optimization and dose distribution evaluation

For each of the ten patients, a total of five different treatment plans were created per beam arrangement. All treatment plans included robustness to setup errors of ±2 mm in every direction as well as robustness to range uncertainties of 0-4%, in increments of 1%. Setup and range errors were implemented by shifting the isocenter and uniform scaling of the HUs in the patient CT, respectively.[183,184] All treatment plans used the same planning constraints and objectives as a patient's clinical treatment plan. As an estimate of computational burden, the number of variables and constraints for the 0%

Table 4.2: Variables and constraints for patients with brain or skull base tumors included in this study. Values concern the 0% range uncertainty robustness treatment plans of the traditional beam arrangements. As a result of the higher number of scenarios, the numbers of variables and constraints for treatment plans optimized using higher levels of range uncertainty robustness were higher than the values shown in this Table.

Patient ID	# of variables [x10^3]	# of constraints [x10^3]
1	75.2	586.4
2	162.6	866.1
3	598.9	831.1
4	310.1	1113.3
5	355.3	894.6
6	394.0	492.1
7	492.8	655.4
8	596.7	1796.0
9	576.1	1060.3
10	697.3	1221.8

range uncertainty robustness treatment plans of all patients are provided in Table 4.2.
All optimizations were performed using the Nymph optimizer.[186,187] Planning objectives were implemented using composite worst-case optimization, which optimizes a single worst-case scenario rather than regarding objective- or voxel-wise worst-case scenarios separately.[124] A total of 7 setup error scenarios x 3 range error scenarios = 21 scenarios were included in all optimizations. For 0% range uncertainty robustness treatment plans, optimizations only contained seven scenarios due to the lack of undershoot and overshoot scenarios. The optimization approach was in line with the previous work, which was presented in the preceding Chapter (cf. Section 3.2.2).
Dose distributions for all scenarios included in the optimization were evaluated using a Python script. A variety of target coverage metrics were determined to assure that target coverage remained consistent between all levels of range uncertainty and in all scenarios. OAR doses were quantified in terms of NTCPs using the LKB model (cf. Section 3.2.3).[189] Results will be limited to OARs which were within 1 cm of the CTV in at least five cases, a condition which was only fulfilled by the brainstem. The parameters used in the underlying LKB model, which was used to calculate the probability of brainstem necrosis, were TD50 = 65 Gy(RBE), n = 0.16, and m = 0.14.[189] In terms of dose distribution analyses, this study applied the same methodology as the work presented in the preceding Chapter (cf. Section 3.2.3).

4.2.4 Monte Carlo simulation workflow

For all cases, an optimized treatment plan was re-calculated via a Monte Carlo simulation. The rationale was to validate the pencil-beam algorithm on which TPS dose calculations relied and to provide information on LET distributions in addition to dose.[90] Monte Carlo simulations were performed using the TOPAS Monte Carlo tool.[93] Monte Carlo simulations only required a patient's planning CT and the relevant treatment plan as inputs. Monte Carlo simulations were performed for the 0% range uncertainty robustness treatment plans of all ten cases. Simulations were performed for the traditional clinical as well as the novel beam arrangements. As was the case for TPS-based dose distributions, Monte Carlo simulations were evaluated in terms of brainstem NTCP with the endpoint of brainstem necrosis. Simulated LET_d distributions were analyzed with respect to the mean LET_d within the brainstem. Examples of a simulated dose- and LET_d distribution are shown in Figure 4.2.

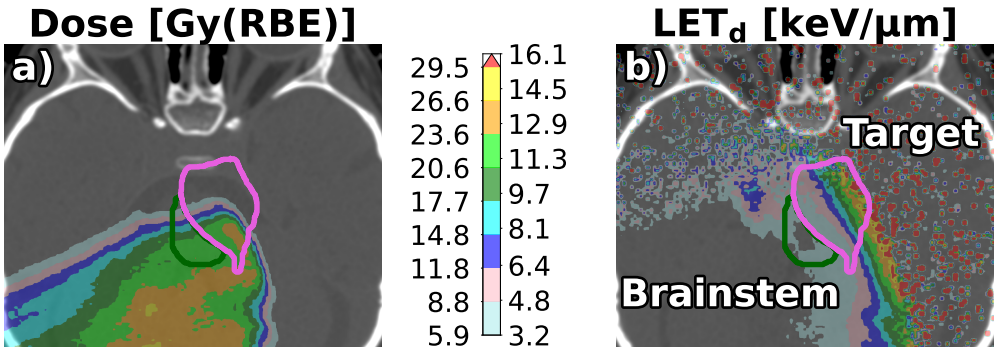

Figure 4.2: A beam-wise (a) dose [Gy(RBE)] and (b) dose-averaged linear energy transfer (LET$_d$) [keV/μm] distribution simulated using the TOPAS Monte Carlo tool.

4.3 Results

4.3.1 Treatment planning system-based results

Overview over range uncertainty reduction benefits

Brainstem NTCPs as a function of range uncertainty are shown in Figure 4.3. The traditional clinical beam arrangement generally achieved lower brainstem NTCPs at current levels of range uncertainty. However, as range uncertainties were reduced, the novel beam arrangement was increasingly able to reduce brainstem NTCPs compared to the traditional clinical beam arrangement.

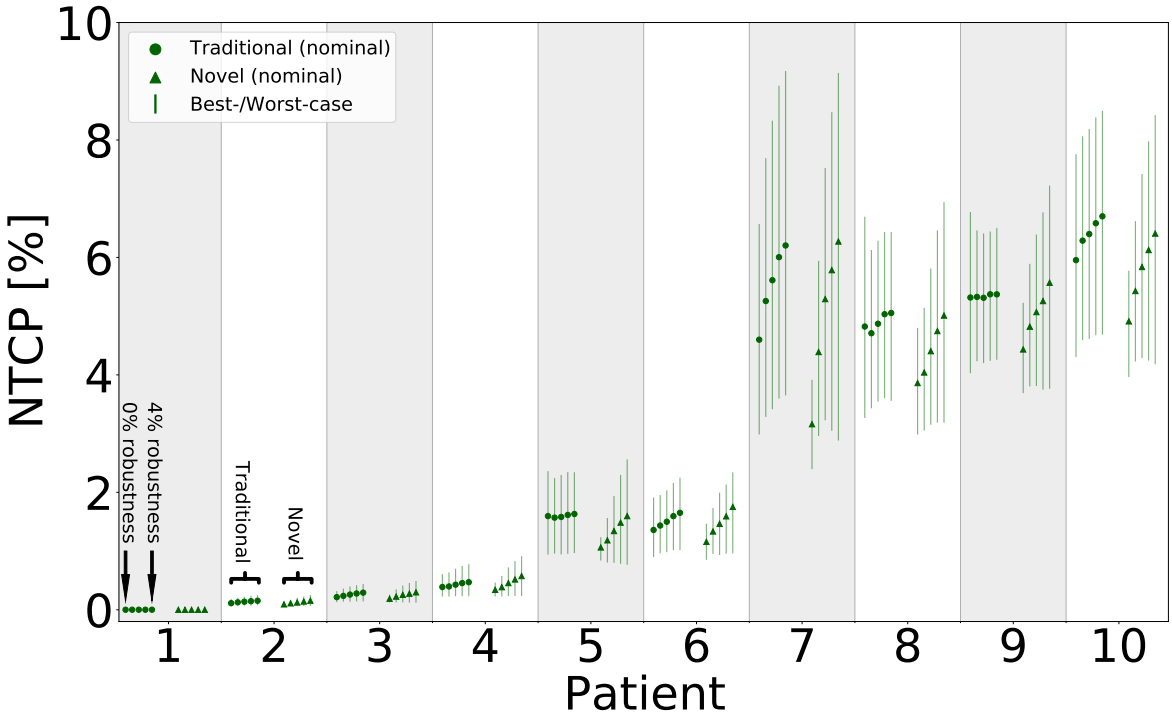

Figure 4.3: Brainstem NTCPs (endpoint: brainstem necrosis) as a function of range uncertainty. Circles and triangles indicate values for the traditional and novel beam arrangement, respectively. Data points concern the nominal scenario, and error bars indicate values in the best- and worst-case scenario. Within each beam arrangement column, range uncertainty robustness ranges from 0% on the left to 4% on the right.

Compared to the traditional beam arrangement, the novel beam arrangement generally increased brainstem NTCPs at current range uncertainties but became increasingly favorable as range uncertainties were reduced. Figure 4.4 depicts the percentage of favorable novel beam arrangements as a function of range uncertainty.

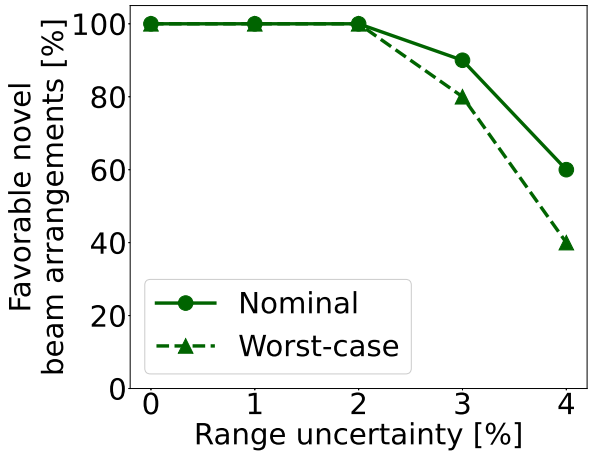

Figure 4.4: Favorable novel beam arrangements as a function of range uncertainty in the nominal (circles) and worst-case scenario (triangles). Data points depict the percentage of the 10 cases in which the novel beam arrangement maintained or reduced the brainstem NTCP compared to the traditional beam arrangement. Lines were plotted to guide the eye.

The novel beam arrangement's favorability at lower range uncertainties was the result of its reliance on the distal beam edge. Figure 4.5 depicts dose distributions for both beam arrangements for treatment plans for Patient 8.

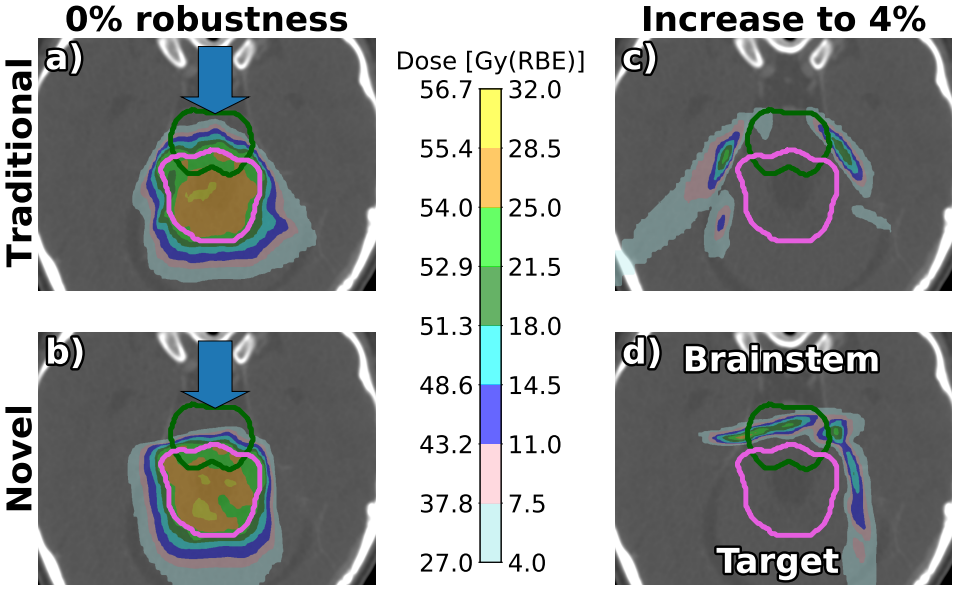

Figure 4.5: Dose distributions for the (a,c) traditional and (b,d) novel beam arrangement for 0% range uncertainty robustness and an increase to 4%, all in the nominal scenario. Blue arrows emphasize dose distribution differences while the green and pink structures are the brainstem and the CTV.

At low range uncertainties, use of the steeper dose fall-off at the distal beam edge allowed the novel

beam arrangement to achieve a sharper dose gradient at the target-brainstem interface. At higher range uncertainties, however, additional dose was "pushed" into the brainstem, which was located behind the target volume. Since the effects of range uncertainties are limited to the beam directions, the traditional beam arrangement, which relied more heavily on the shallower fall-off at the lateral beam edge, did not exhibit this behavior.

Patient-specific factors indicating higher range uncertainty reduction benefits

Range uncertainty reduction benefits observed in a given case were linked to various patient-specific parameters. In terms of brainstem sparing, the most relevant patient-specific factor was the highest dose prescribed to any part of the CTV. Figure 4.6 depicts the benefits of range uncertainty reductions as a function of prescription dose. With respect to brainstem sparing, range uncertainty reduction benefits increased with the highest dose prescribed to any part of the target.

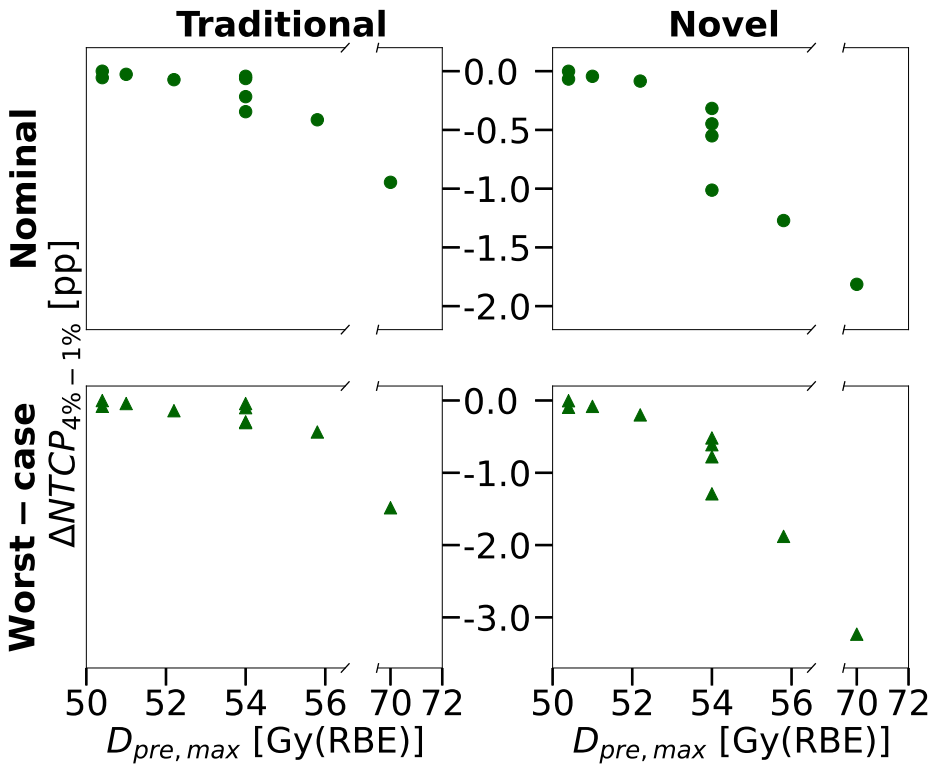

Figure 4.6: Range uncertainty reduction benefits in terms of brainstem NTCP reductions achieved by reducing range uncertainties from 4% to 1% $\Delta NTCP_{4\%-1\%}$ as a function of the maximum prescription dose to any part of the target $D_{pre,max}$. The left and right column show results for the traditional and the novel beam arrangement, respectively, while the top and bottom row depict values in the nominal and the worst-case scenario.

4.3.2 Pencil-beam model validation through Monte Carlo simulations

Figure 4.7 depicts TPS- and Monte Carlo simulation-based brainstem NTCPs for all patients and both beam arrangements. Good agreement was observed between TPS- and Monte Carlo simulation-based dose distributions. Slight differences in brainstem NTCPs were the result of more accurate modeling of multiple Coulomb scattering by Monte Carlo simulations.

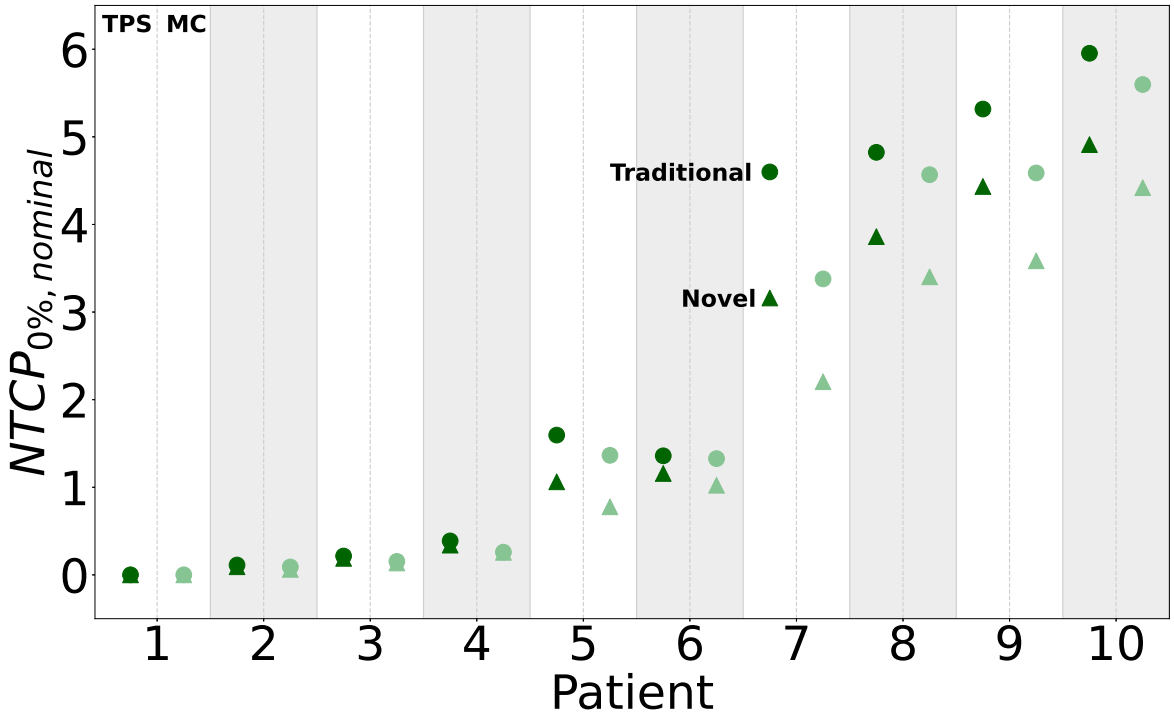

Figure 4.7: TPS- and Monte Carlo simulation-based brainstem NTCPs for the traditional (circle) and novel (triangle) beam arrangement. All values concern the nominal scenario of the 0% range uncertainty robustness treatment plan.

For all performed simulations, the mean dose-averaged linear energy transfer LET_d within the brainstem is shown in Table 4.3. The novel beam arrangement generally exhibited a slightly higher mean LET_d within the brainstem than the traditional clinical beam arrangement.

Table 4.3: Mean dose-averaged linear energy transfers LET_d within the brainstem for both beam arrangements and all cases included in this study. Values concern the nominal scenario of the 0% range uncertainty robustness treatment plan.

Patient ID	$\boldsymbol{LET_d}$ **[keV/μm]**	
	Traditional	**Novel**
1	5.5	5.2
2	3.3	3.3
3	3.1	3.7
4	5.2	5.1
5	4.6	6.1
6	2.7	3.1
7	2.5	2.7
8	4.0	5.7
9	4.0	5.7
10	4.0	4.3

4.4 Discussion

4.4.1 Feasibility of novel beam arrangements

To help determine the potential benefits of novel proton therapy beam arrangements, the level of range uncertainty at which such beam arrangements become favorable relative to the traditional clinical beam arrangement is essential. In the cases included in this study, all novel beam arrangements were favorable at a range uncertainty of 2% in both the nominal and the worst-case scenario. Since range verification techniques already report millimeter accuracy, a reduction to such a level of range uncertainty may be realistic.[13,168]

In eight out of ten cases, the novel beam arrangement became favorable at a range uncertainty higher than 2%. In some cases, even range uncertainty reductions of less than 2% may therefore enable the use of novel beam arrangements. For four out of ten patients, the novel beam arrangement was feasible even at the current level of clinical range uncertainties. This was the result of the brainstem NTCP remaining at or close to 0% at all levels of range uncertainty. In these cases, the novel beam arrangement was not associated with marked benefits, but it was also not inferior to the traditional clinical beam arrangement according to any of the evaluated metrics.

4.4.2 Patient-specific factors indicating higher range uncertainty reduction benefits

In terms of brainstem sparing, range uncertainty reduction benefits increased with the highest prescription dose to any part of the target. This is in line with the results of the study presented in Chapter 3, in which the same effect was observed in a data set based on treatment plans for ten skull base cancer patients with clival tumors.[182] As already discussed in the previous Chapter, this pattern was the result of the size of the brainstem and the LKB model parameters used to calculate brainstem NTCPs. The brainstem was generally larger than or of the same size as the CTV, so a considerable part of the brainstem received no or little dose. At the same time, the LKB model tolerance dose parameter of TD50 = 65 Gy(RBE) was high compared to most prescription doses. For a prescription dose of 50.4 Gy(RBE) - the lowest of any of the cases included in this study - LKB model parameters result in a brainstem NTCP of 5.4% even if the entire brainstem was to be irradiated with the prescription dose.

The work presented in the preceding Chapter indicated that, in terms of brainstem sparing, direct range uncertainty reduction benefits increase with prescription dose (cf. Chapter 3). This study confirms that the benefits of novel beam arrangements are also more pronounced for higher prescription doses. With respect to brainstem sparing, cases with higher prescription doses or dose boosts to any part of the target are therefore expected to especially benefit from range uncertainty reductions.

4.4.3 The relative importance of considering novel beam arrangements

As discussed in Section 3.4.1, previous studies have suggested that the benefits of setup error reductions exceed the benefits of reducing range uncertainties. Based on 20 oropharyngeal cases, van de Water et al. reported that a 2 mm reduction in setup error margin - from 3 mm to 1 mm - was accompanied by a decrease in the average NTCP of 1.9 percentage points.[183] A 3% to 1% range uncertainty reduction, on the other hand, only reduced the average NTCP by 0.4 percentage points. Based on ten head & neck cases, Wagenaar et al. quantified the benefits of a 1 mm setup error reduction as a reduction in average NTCPs of 2.0 percentage points.[184] A 1% range uncertainty reduction, on the other hand, only lowered the average NTCP by 0.9 percentage points.

Because of MGH's background in range uncertainty reduction techniques, the focus lay on quantifying the benefits of range uncertainty reductions. The impact of changes in setup error were not quantified and therefore cannot be used for a comparison. Range uncertainty reduction benefits were, however, markedly higher when the effects of novel beam arrangements were considered in addition

to the direct benefits of reducing range uncertainties.
The aforementioned studies worked under the assumption of current clinical practices, including traditional clinical beam arrangements. Future projects comparing the benefits of reductions in setup margin and range uncertainty should therefore include indirect benefits of range uncertainty reductions such as the feasibility of novel beam arrangements at lower levels of range uncertainty. Since range uncertainty reduction benefits were markedly higher when such effects were considered, indirect effects like the feasibility of novel beam arrangements may constitute a significant part of the total benefits of reductions in proton range uncertainties.

4.4.4 Radiobiological effects near the proton end-of-range

Dose calculations applied a constant RBE value of 1.1, as is current clinical practice. However, models in which RBE varies as a function of dose, LET, and other parameters are being investigated as well.[42–45] Such models exhibit an increase in RBE in high-LET regions, including the distal proton beam edge. This is because higher LET values are associated with denser ionization tracks, increasing the likelihood of complex, hard-to-repair damage to the DNA in irradiated cells. In this study, the novel beam arrangement often increased the mean dose-averaged linear energy transfer within the brainstem compared to the traditional clinical beam arrangement. The potential effects of variations in RBE therefore have to be considered.
However, to what extent variable RBE models apply to the quantified endpoints is unclear. Variable RBE models are generally based on data for clonogenic cell survival. They are therefore more applicable to target structures than organs-at-risk, in addition to being associated with considerable uncertainties.[36,196] For brainstem necrosis specifically, clinical studies which included patients with Central Nervous System (CNS) malignancies, low-grade glioma, posterior fossa tumors, and medulloblastoma reported that proton therapy is associated with reduced or comparable toxicity rates compared to conventional photon treatments[197–200] The medulloblastoma study also observed higher LET values than in the target but statistically not significant RBE differences in eight out of ten treatment change areas identified using MRI.[200]
Range uncertainties induced by variations in RBE have been reported to be on the scale of a few mm or smaller than 2%.[4,44,201] In this study, the novel beam arrangement was favorable at a range uncertainty of 2% in all cases. In most cases, the novel beam arrangement became feasible at range uncertainties higher than 2%. This indicates that novel beam arrangements would have remained favorable even if the potential effects of variations in RBE had been considered, provided that range uncertainties can be reduced to a sufficiently low level.
This study applied the same dose-based planning constraints and objectives as the patients' clinical treatment plans. However, approaches to optimize LET in addition to dose are under investigation as well.[202] Optimizing LET may reduce the potential risks of radiobiological effects at the proton end-of-range. Including LET-based objectives in the optimizations may affect the NTCP benefits of novel beam arrangement as quantified in this study. However, the benefits associated with the novel beam arrangement exceeded the direct benefits of range uncertainty reductions, by a factor of 2 or more in some cases. Novel beam arrangements may therefore be able to achieve benefits in terms of NTCP reduction even if LET is optimized in addition to dose. Previously-quantified RBE-induced proton range shifts could alternative be included in the optimization directly, for example by applying them to the proton range as a modifier.[4,44,201]
Once range uncertainties have been reduced to a sufficiently low level and the potential effects of novel beam arrangements have been studied in greater detail, a clinical study can be conducted to compare the effects of traditional and novel proton therapy beam arrangements. Brainstem necrosis is a very severe side effect, and care is taken to keep brainstem necrosis rates very low as a result. To quantify the effect in terms of brainstem sparing, a clinical trial would therefore have to be sufficiently large to assure that differences in brainstem necrosis rates can be observed.

4.4.5 Beam angle optimization

For this study, novel beam arrangements were chosen manually. However, beam angle optimization approaches are also under investigation.[203,204] The existence of novel beam arrangements which may have been even more favorable relative to the traditional beam arrangement can therefore not be ruled out.
For all cases, the traditional beam arrangement was defined as the beam arrangement with which a given patient had been treated clinically. It was therefore not considered necessary to investigate alternative beam arrangements chosen following current clinical practices. If beam angle optimization was applied to determine novel beam arrangements, however, the same methodology should be used to determine traditional beam arrangements to assure a fair comparison.

4.5 Conclusion and outlook

The benefits of novel beam arrangements which will be made feasible by proton range uncertainty reductions were quantified based on a data set consisting of treatment plans for ten cancer patients with brain or skull base tumors. In terms of brainstem sparing, range uncertainty reduction benefits increased with the highest dose prescribed to any part of the target. This is in agreement with the findings of the study presented in Chapter 3, which observed the same pattern for patients with clival tumors.
Compared to the traditional clinical beam arrangement, the novel beam arrangement was favorable in all cases starting at a range uncertainty of 2%. In many cases, the novel beam arrangement became favorable at range uncertainties higher than 2%. In some cases, the benefits associated with novel beam arrangements may therefore be achieved even before range uncertainties can be reduced to a level of 2%.
Range uncertainty reductions are associated with NTCP and normal tissue dose decreases even under the assumption of traditional clinical beam arrangements.[182–184] However, in some cases, the benefits of novel beam arrangements exceeded the direct benefits of range uncertainty reductions by a factor of two or more. Indirect effects like the feasibility of novel beam arrangements at lower levels of range uncertainty may therefore constitute a considerable part of total range uncertainty reduction benefits.
This study was conducted under the assumption of a constant RBE value of 1.1, as is current clinical practice. However, due to their greater reliance on the distal beam edge, novel beam arrangements may be especially affected by radiobiological effects near the proton end-of-range. In this study, all novel beam arrangements were favorable at a range uncertainty of 2%. The LET-induced range shift, on the other hand, has been estimated to be smaller than 2%. Novel beam arrangements therefore remained favorable even when radiobiological effects near the end-of-range are considered, provided range uncertainties can be reduced to a sufficiently low level.
Further studies are required to investigate the potential effects of LET-based optimization and whether novel beam arrangements may be able to achieve similar benefits in terms of LET as in terms of NTCP. Including LET in addition to dose-based objectives in the optimization may reduce the benefits of novel beam arrangements as quantified in this study. However, since the benefits of novel beam arrangements exceeded the direct benefits of range uncertainty reductions markedly, novel beam arrangements may remain beneficial even when the potential risks of radiobiological effects are mitigated.

CHAPTER 5

Validation of prompt gamma-ray spectroscopy for proton range verification

The measurements described in this Chapter were conducted for the purpose of this thesis and accepted for publication in *Physics in Medicine and Biology*.[205] Figure 5.1 and Figure 5.3 to Figure 5.6 as well as Table 5.2 to Table 5.7 were included in said article, either as they are or in an adapted form. The text was re-written for clarity and to provide additional information, and all remaining Figures and Tables were added for the same reason.
This study validates the performance of the detector prototype for proton range verification via prompt gamma-ray spectroscopy developed at MGH using a variety of tissue-mimicking and porcine samples. Section 5.1 provides an overview over prompt gamma-ray-based proton range verification methods and puts this work into the context of previously-reported measurements. Section 5.2 provides information on the detector prototype, the samples used, and the measurement and data evaluation workflow. Section 5.3 presents measured sample SPRs relative to water as well as prompt gamma-ray spectroscopy-based assessments of proton ranges and elemental compositions of samples. The accuracy of these results and related aspects such as measurement uncertainties are discussed in Section 5.4, and the Chapter is concluded by Section 5.5.

5.1 Motivation for prompt gamma-ray spectroscopy measurements of tissue-mimicking and porcine samples

As discussed in Section 2.2, proton therapy still faces considerable hurdles, out of which uncertainties in the *in vivo* proton range are among the most significant ones. The benefits of reductions in proton range uncertainties were quantified by studies such as the ones presented in Chapter 3 and Chapter 4.[182–184] A variety of different approaches to reduce range uncertainties in proton therapy are currently under investigation. At the treatment planning stage, dual-energy computed tomography and proton imaging have both been shown to be capable of reducing uncertainties stemming from conventional CT treatment planning images (cf. Section 2.2.2).
In vivo proton range monitoring can be achieved through measurements performed during or shortly after patient irradiation (cf. Section 2.2.3). This includes PET imaging of activated nuclei during or shortly after patient treatment as well as measurements of acoustic waves emitted as a result of pulsed proton irradiation. Since they are emitted nearly instantaneously, prompt gamma-rays emitted through nuclear reactions occurring during patient treatment allow the *in vivo* proton range to be verified in real time.
Systems for prompt gamma-ray-based proton range verification differ in terms of implementation (cf. Section 2.2.3). Approaches include passively-collimated cameras with knife-edge or multi-parallel slit designs as well as Compton cameras and systems which utilize the depth-dependence of the time it takes protons to stop within the patient.[162–165] Phantom measurements have been performed with a

variety of different systems, and range verification measurements performed with a knife-edge shaped slit camera during clinical patient treatments have also already been reported.[168–171]
Prompt gamma-ray spectroscopy relies on measurements of the spectrum of emitted prompt gamma-rays for proton range verification in real time (cf. Section 2.2.3).[11,12] Energies of prompt gamma-rays emitted during proton irradiation depend on the underlying nuclear reactions and therefore the elemental composition of the irradiated tissue. In addition, gamma-ray lines of different energies exhibit different depth profiles. Through measurements of the emitted prompt gamma-rays, proton range and elemental composition of the irradiated tissue can therefore be determined simultaneously and in real time.
MGH previously constructed a detector prototype for proton range verification via prompt gamma-ray spectroscopy. Results of some experimental measurements were already reported.[13] For the study presented in this Chapter, prompt gamma-ray spectroscopy measurements were performed for a variety of non-plastic tissue-mimicking and porcine samples. Irradiated samples varied in terms of elemental composition and included a variety of soft tissues, spongiosa, and cortical bone. By validating the detector prototype's performance in a range of realistic materials, this work bridges the gap between previously reported experimental measurements and clinical range verification performed during patient treatment.

5.2 Materials and methods

5.2.1 Prompt gamma-ray spectroscopy detector prototype

The prompt gamma-ray spectroscopy detector prototype is shown in Figure 5.1. The prototype consisted of a detection system mounted on a hexapod for high-accuracy positioning.

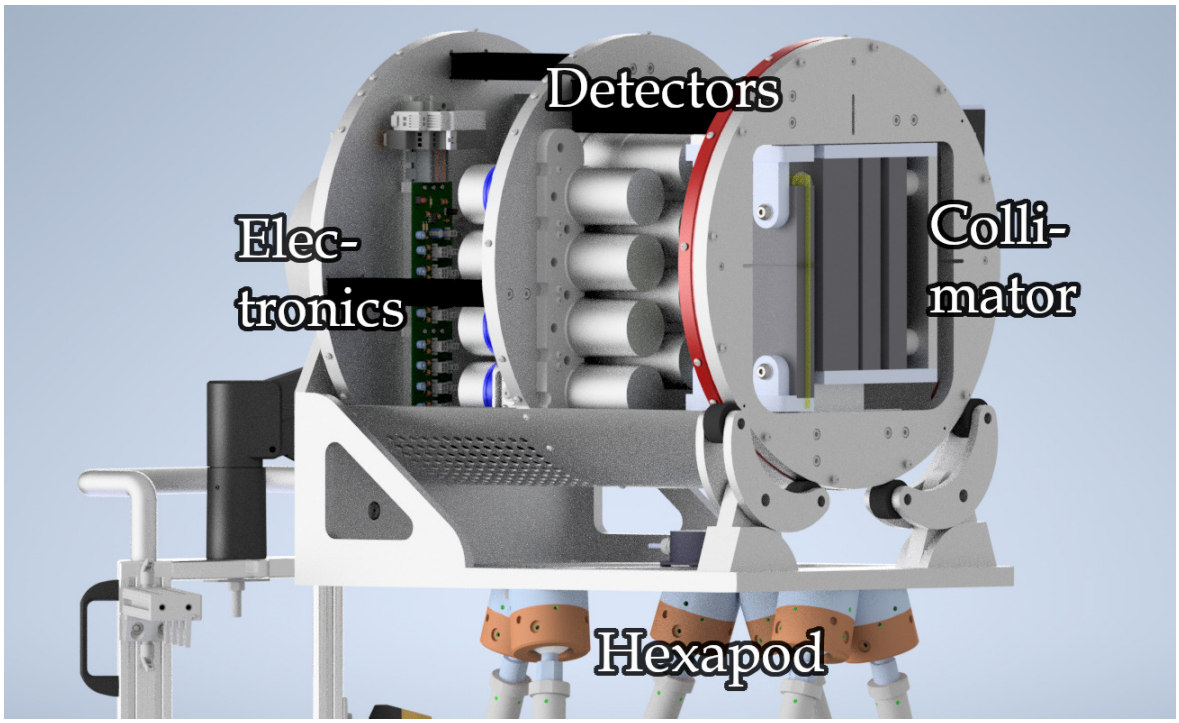

Figure 5.1: The prompt gamma-ray spectroscopy detector prototype developed at MGH, Boston, USA. The detector system is mounted on a hexapod with six degrees of freedom for positioning with sub-millimeter accuracy.

Detector system

Prompt gamma-rays were detected by eight detector modules arranged in a closely packed configuration. Each detector module consisted of a Cerium-Doped Lanthanum Bromide (LaBr3:Ce) scintillation crystal (Saint-Gobain, Saint-Pierre-lès-Nemours, France) coupled to a Photomultiplier Tube (PMT). The scintillation material had been chosen because of its high interaction probability with gamma-rays in the relevant energy range, and its excellent energy and time resolution. The high energy resolution of LaBr3:Ce was relevant because it allowed for superior differentiation between discrete prompt gamma-ray lines of different energies. Each scintillation crystal had a diameter of 51 mm and was 76 mm long. The total volume of scintillation material was therefore 1236 cm^3.
The detector prototype's field-of-view was 12 cm $\times$ 32 cm $\times$ 32 cm, divided into voxels of 1 mm $\times$ 2 mm $\times$ 2 mm. The field-of-view dimension of 12 cm refers to the direction along the proton beam. Since the prototype's purpose was to determine proton ranges, having the highest resolution in this dimension was important. The detection system was collimated by five slabs of tungsten, each of which was 25.4 mm wide and 127 mm thick. The tungsten collimator contained two openings 25.4 mm apart. This allowed the detector to focus on two different positions along the proton beam simultaneously.

Hexapod

The detector system is mounted on a hexapod (Mikrolar, Hampton, New Hampshire, USA) for positioning with sub-millimeter accuracy. Sensors determined pitch and roll corrections so that the detection system could be leveled automatically. The detector prototype was aligned to the measurement setup through its alignment lasers. The hexapod was able to position the detection system through movements in three-dimensional space as well as changes in pitch, roll, and yaw. A more detailed description of the entire system is provided in a previous publication by the developers.[13]

Data acquisition and processing

The detector prototype was connected to a data acquisition system in the treatment control room. The system's sample rate of 212.6 MHz was equal to double the radiofrequency of the cyclotron. A variety of minor corrections were applied. These included a correction for the signal amplitude's dependence on count rate, which was corrected using the 2.22 MeV prompt gamma-ray line resulting from neutron capture by hydrogen. Corrected data was separated into three different components: the neutron-induced continuum, the proton-induced continuum, and the resolved prompt gamma-ray lines.

- **Neutron-induced continuum:** neutron-induced prompt gamma-rays, which may be scattered before or within the detector or can result from unresolved cascades from the decay of higher-energy states; discrete neutron-induced prompt gamma-rays such as the 2.22 MeV line resulting from neutron capture by hydrogen also contribute

- **Proton-induced continuum:** proton-induced prompt gamma-rays, which may also be scattered before or within the detector or result from high-energy excitation states leading to cascades of unresolvable prompt gamma-ray lines

- **Resolved prompt gamma-ray lines:** determined by subtracting the neutron- and proton-induced continua from the corrected data; this includes prompt gamma-rays which deposit their full energy minus one or two escape photons of energy E = 511 keV, since many prompt gamma-rays will interact via pair production and one or both of the resulting annihilation photons may escape detection

An overview over the energy- and time characteristics of the three components is provided in Table 5.1. Since the detection system was phase-locked to the cyclotron, proton-induced prompt gamma-

rays, which are associated with the time during which protons are delivered, were able to be differentiated from the neutron-induced continuum, for which this was not the case. Resolved lines were then separated from the proton-induced continuum using the Statistics-Sensitive Non-Linear Iterative Peak-Clipping (SNIP) algorithm.

Table 5.1: Energy-time histogram components into which prompt gamma-ray spectroscopy data was separated. Unlike proton-induced components, the neutron-induced continuum was not resolved in time.

Component	Resolved in energy?	Resolved in time?
Neutron-induced continuum	No	No
Proton-induced continuum	No	Yes
Resolved prompt gamma-ray lines	Yes	Yes

5.2.2 Sample preparation

Measurements were performed in water, four tissue-mimicking samples, and two porcine samples. Measurements in water were necessary so that SPRs relative to water could be determined for all samples. Irradiated samples encompassed a variety of different tissues, including a range of soft tissues, spongiosa, and cortical bone. Two tissue-mimicking samples are shown in Figure 5.2.

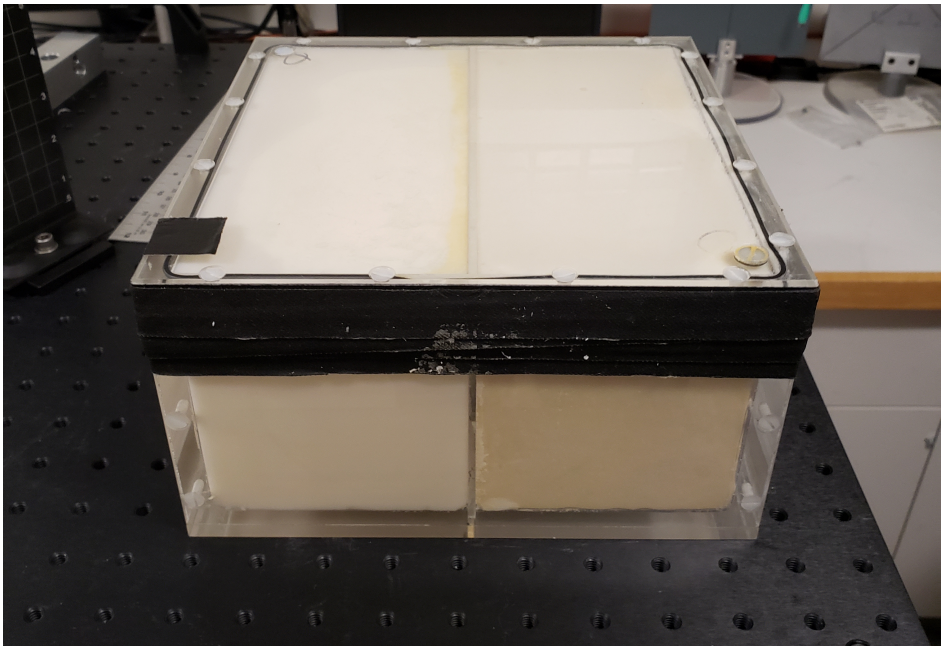

Figure 5.2: Spongiosa and adipose tissue samples. These two samples were placed in a double container with a small divider in the middle so that measurements at the interface between the samples could be performed.

Tissue-mimicking samples

This study included four different tissue-mimicking samples: muscle, spongiosa, adipose tissue, and cortical bone. Tissue-mimicking samples consisted of mixtures of water, protein, fat, Hydroxyapatite (HA), and Sodium Dodecyl Sulfate (SDS). Collaborators who participated in this project established the tissue-mimicking sample recipes in a previous publication, which was guided by the tissue compositions published in Report 44 of the International Commission on Radiation Units and

Measurements (ICRU) and Publication 23 of the International Commission on Radiological Protection (ICRP).[206–208] Tissue-mimicking sample recipes are provided in Table 5.2.

Table 5.2: Tissue-mimicking sample recipes in terms of the percentage of water, protein (gelatin), fat (porcine lard), hydroxyapatite (HA), and sodium dodecyl sulfate (SDS) (by mass). Collaborators who participated in this project established the tissue-mimicking sample recipes in a previous publication, which was guided by the tissue compositions published in Report 44 of the ICRU and Publication 23 of the ICRP.[206–208]

Sample	**Composition [% by mass]**				
	Water	**Protein**	**Fat**	**HA**	**SDS**
Muscle	74.8	20.0	5.0	0.0	0.3
Adipose tissue	0.0	0.0	100.0	0.0	0.0
Spongiosa	27.9	11.8	47.4	11.5	1.3
Cortical bone	59.5	0.0	0.0	40.5	0.0

Low-bloom gelatin, which was used to mimic protein and which was found to produce fewer clumps than high-bloom gelatin, was mixed into hot water until fully dissolved. Ultrapure water was used since it was observed to result in fewer air bubbles than tap water. Initial samples used coconut oil to mimic fat, but porcine lard was found to achieve comparable sample homogeneity and stability while being animal- rather than plant-derived. Small amounts of SDS were added to tissue-mimicking samples which contained fat to promote mixing of oil with water, improving sample homogeneity.
Elemental compositions of tissue-mimicking samples were determined based on the elemental compositions of their constituents. Elemental compositions of protein and fat components were determined using CHNS combustion analysis to determine the carbon (C), hydrogen (H), nitrogen (N), and sulfur (S) content in addition to the oxygen concentration. Combustion analysis was performed at the Berkeley College of Chemistry Microanalytical Facility (Berkeley, California, USA).[209] Trace elements such as phosphorus, calcium, and sodium were assumed to be negligible, and protein and fat components were assumed to only consist of oxygen, carbon, hydrogen, nitrogen, and sulfur.[207] Since HA and SDS were analytical-grade and therefore of high purity, their elemental compositions were already known with a high degree of accuracy. For all four tissue-mimicking samples, elemental compositions are shown in Table 5.3.

Table 5.3: Elemental compositions and mass densities of tissue-mimicking samples. Elemental compositions are given in terms of the percentage of hydrogen (H), carbon (C), nitrogen (N), oxygen (O), phosphorus (P), sulfur (S), calcium (Ca), and sodium (Na).

Sample	**Elemental composition [%]**								$\rho\,[\frac{g}{cm^3}]$
	H	**C**	**N**	**O**	**P**	**S**	**Ca**	**Na**	
Muscle	10.4	12.3	3.0	74.2	0.0	0.1	0.0	0.0	1.06
Adipose tissue	12.3	78.0	0.0	9.7	0.0	0.0	0.0	0.0	0.94
Spongiosa	9.9	42.5	1.8	38.7	2.1	0.2	4.6	0.1	1.08
Cortical bone	6.7	0.0	0.0	69.6	7.5	0.0	16.2	0.0	1.40

Porcine samples

Porcine brain and liver samples were acquired and processed by Animal Technologies, Inc. (Tyler, Texas, USA). Heparin was added to porcine blood as an anticoagulant, and porcine brain and liver samples were cut into pieces of 1 cm or smaller in size. For irradiation, all seven samples were filled into Polymethyl Methacrylate (PMMA) containers with inner dimensions 20 cm (l)$\times$ 10 cm (h) $\times$ 10 cm (w). Air bubbles in porcine phantoms were filled with porcine blood to reduce their potential

effects during measurements.
To determine ground truth elemental compositions, three small sections of each porcine sample were fully dehydrated, ground into a fine, homogeneous powder, and sent off for CHNS combustion analysis. Trace elements were again assumed to be negligible. For each sample, combustion analysis results were averaged. However, variations between different sections of the porcine samples were small, with mean differences of 0.3% for the porcine brain sample and 0.2% for the porcine liver sample. Elemental compositions of the final porcine phantoms were determined based on the results of combustion analysis and the elemental composition of porcine blood in addition to the amount of hydrated tissue and blood in each container.[207] Resulting ground truth elemental compositions of porcine samples are provided in Table 5.4.

Table 5.4: Elemental compositions and mass densities of porcine samples. Elemental compositions are given in terms of the percentage of hydrogen (H), carbon (C), nitrogen (N), oxygen (O), phosphorus (P), sulfur (S), calcium (Ca), and sodium (Na).

Sample	**Elemental composition [%]**								$\rho\,[\frac{g}{cm^3}]$
	H	**C**	**N**	**O**	**P**	**S**	**Ca**	**Na**	
Brain	10.8	7.8	1.3	80.0	0.0	0.1	0.0	0.0	1.01
Liver	10.4	10.6	2.6	76.1	0.0	0.2	0.0	0.0	1.06

CT scans of irradiated samples

Prompt gamma-ray spectroscopy data evaluation required a CT scan of all samples to be acquired so that Monte Carlo simulations of the irradiation could be performed on said scans. All scans were acquired on the same GE Discovery CT590 RT (GE Healthcare, Chicago, Illinois, USA) CT scanner in the radiation oncology department at MGH. The settings used for all seven scans were as follows:

- **Tube voltage:** 140 kVp
- **Tube current:** 250 mAs
- **Slice thickness:** 1.25 mm
- **Pixel size:** 0.68 mm $\times$ 0.68 mm
- **Pitch:** 0.56

All CT scans were reconstructed using Adaptive Statistical Iterative Reconstruction (ASIR).[210] All sample containers were oriented such that the proton beam would traverse the sample from left to right rather than inferior to posterior. This was done to achieve a higher spatial resolution along the beam direction, which was relevant for the accuracy of the proton range verification measurements.

Treatment planning

To determine ground truth proton ranges, Multi-Layer Ionization Chamber (MLIC) measurements were performed with the Zebra (IBA Dosimetry, Schwarzenbruck, Germany), which contains 180 ionization chambers read out simultaneously.[211] The Zebra's detector spacing along the beam axis was 2 mm, with a collecting electrode of diameter 2.5 cm. All MLIC measurements were performed with a 223.6 MeV proton beam. This energy was high enough to fully traverse all samples with some residual range in the detector, as is required for MLIC measurements. Since higher-energy proton beams exhibit more pronounced range straggling, the high energy required for MLIC measurements likely somewhat reduced the impact of the Zebra's detector spacing along the beam axis (cf. Section 2.1.1).
For prompt gamma-ray spectroscopy measurements, three separate treatment plans were created.

Treatment planning assumed that the sample consisted of water and was performed in Astroid, MGH's in-house proton therapy treatment planning system.[185] For two of the created treatment plans, a 5 cm $\times$ 5 cm $\times$ 5 cm target structure was defined at a depth of 12.5 cm to 17.5 cm and centrally in height and width. The third treatment plan was created for measurements at the interface between two samples and therefore positioned the target with the interface in its center (in terms of width) rather than centrally within a single container. In accordance with clinically realistic doses, the dose delivered to the aforementioned target structure was 0.9 Gy in all three cases, and the gantry angle was 270°. The irradiation time was less than a minute in all cases.
All prompt gamma-ray spectroscopy measurements of single samples except for the measurement of the cortical bone sample utilized the same treatment plan. This was because the cortical bone sample was the only tissue for which the expected SPR differed markedly from a value of 1.0. Delivering the same treatment plan for all measurements would therefore have required the prompt gamma-ray spectroscopy detector prototype to be re-positioned before the measurement of the cortical bone sample. An alternative treatment plan with higher proton energies allowed proton ranges to be comparable between all measurements, so the detector prototype's position did not have to be adjusted at any point. For all three treatment plans, information such as minimum and maximum proton energies and the number of energy layers and proton pencil-beam spots is provided in Table 5.5. The delivery technique for all treatment plans was pencil-beam scanning.

Table 5.5: Treatment plan parameters for prompt gamma-ray spectroscopy. A separate treatment plan with higher proton energies was created for measurements of the cortical bone sample so that proton ranges were comparable between all measurements. This prevented the prompt gamma-ray spectroscopy detector prototype from having to be repositioned between measurements. E_{min} and E_{max} refer to the minimum and maximum proton energies, and N_{layers} and N_{spots} refer to the number of energy layers and the total number of proton pencil-beam spots. N_{p^+} indicates the total number of protons delivered to all spots (in gigaprotons).

Treatment plan	$\boldsymbol{E_{min}}$ **[MeV]**	$\boldsymbol{E_{max}}$ **[MeV]**	$\boldsymbol{N_{layers}}$	$\boldsymbol{N_{spots}}$	$\boldsymbol{N_{p^+}}$ **[x10^9]**
Cortical bone	153.7	191.3	12	476	39.4
Other samples	132.7	161.6	11	276	33.8
Sample interface	132.7	164.4	12	253	31.0

5.2.3 Measurement setup

The measurement setup is shown in Figure 5.3. For MLIC measurements, protons have to fully traverse the sample and stop somewhere in the MLIC. The Zebra was therefore positioned downstream of the sample. For prompt gamma-ray spectroscopy, protons stop within the sample instead. The prompt gamma-ray spectroscopy detector prototype was therefore positioned perpendicularly to the proton beam direction. Due to the two openings in the tungsten collimator, the detector focused on a more distal and more proximal position along the proton beam simultaneously. The air gap between the outer wall of the sample containers and the detector's front plate was 20 cm, and samples were positioned using orthogonal X-ray imaging.
To improve setup reproducibility, the platform on which samples were placed was clamped to the platform on which the Zebra was positioned. The Zebra platform was, in turn, attached to an indexing bar on the treatment couch. Measurements were performed at MGH's Francis H. Burr Proton Therapy Center in Boston, Massachusetts. The center uses a C230 cyclotron (Ion Beam Applications, Louvain-la-Neuve, Belgium) for particle acceleration. The maximum possible proton energy was 230 MeV. Proton energies were degraded through an energy selection system, and the magnetic beamline connecting the cyclotron to the treatment room at which measurements were performed was approximately 35 meters long.

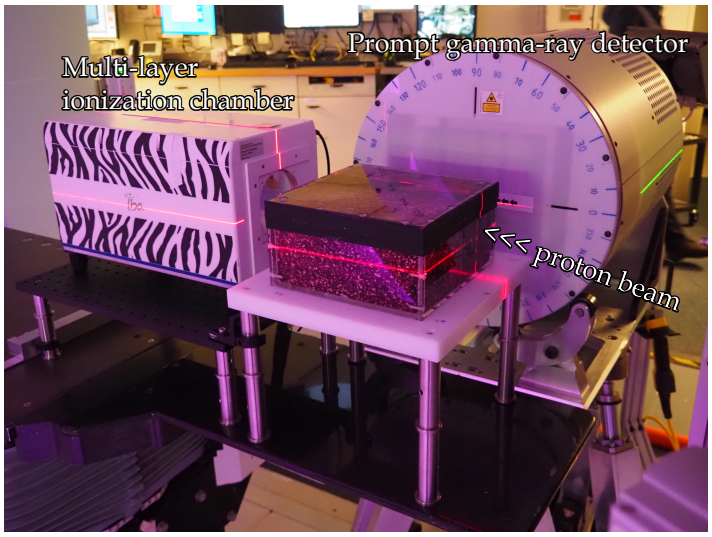

Figure 5.3: MLIC and prompt gamma-ray spectroscopy measurement setup. Protons exited the nozzle on the right and, for multi-layer ionization chamber measurements, fully traversed the sample before stopping in the Zebra detector. For prompt gamma-ray spectroscopy, protons were required to stop within the sample instead.

5.2.4 Data evaluation workflow

Stopping power measurements

Multi-layer ionization chamber measurements were performed for all tissue-mimicking and porcine samples as well as water and an empty container. The latter measurement allowed the impact of the walls of the containers in which samples were placed to be accounted for more accurately. The stopping power ratio relative to water SPR_{sample} was calculated for every sample:[212]

$$\mathrm{SPR}_{sample} = \frac{R^{80}_{sample} - R^{80}_{air}}{R^{80}_{water} - R^{80}_{air}} \left(1 - \mathrm{SPR}_{air}\right) + \mathrm{SPR}_{air}, \tag{5.1}$$

where R^{80} is the distal position at which the measured dose falls off to 80% of its maximum, and the indices *sample*, *water*, and *air* indicate range measurements for the relevant sample, water, and the empty container, respectively. Measurements for water and air were performed for a single container rather than all containers, but caliper measurements of inner and outer container dimensions confirmed that, along the beam axis, the dimensions of all containers were within 0.4 mm of each other. For all measurements, R^{80} was read out of the OmniPro-Incline software with which MLIC measurements were performed, which determines the proton range by interpolating an analytical Bragg peak formula. SPR_{air} is the stopping power ratio of air relative to water and was retrieved from the PSTAR database of NIST, which computes values according to the methodology laid out in ICRU Report 37 and Report 49.[33]

Prompt gamma-ray spectroscopy

Prompt gamma-ray spectroscopy data evaluation focused on nuclear reactions with oxygen and carbon, the two most abundant elements in human tissues.[213] The prompt gamma-ray lines considered and the nuclear reactions through which prompt gamma-rays of the relevant energies are emitted were:

- **Oxygen:**

1.63 MeV: ^{16}O(p,xγ)^{14}N
2.00 MeV: ^{16}O(p,xγ)^{11}C
2.04 MeV: ^{16}O(p,xγ)^{15}O
2.31 MeV: ^{16}O(p,xγ)^{14}N
2.74 MeV: ^{16}O(p,p'γ)^{16}O
2.79 MeV: ^{16}O(p,xγ)^{14}N
2.80 MeV: ^{16}O(p,xγ)^{11}C
2.87 MeV: ^{16}O(p,xγ)^{10}B
4.44 MeV: ^{16}O(p,xγ)^{12}C
4.44 MeV: ^{16}O(p,xγ)^{11}B
5.18 MeV: ^{16}O(p,xγ)^{15}O
5.24 MeV: ^{16}O(p,xγ)^{15}O
5.27 MeV: ^{16}O(p,ppγ)^{15}N
5.30 MeV: ^{16}O(p,ppγ)^{15}N
6.13 MeV: ^{16}O(p,p'γ)^{16}O
6.18 MeV: ^{16}O(p,xγ)^{15}O

- **Carbon:**

2.00 MeV: ^{12}C(p,xγ)^{11}C
2.80 MeV: ^{12}C(p,xγ)^{11}C
2.87 MeV: ^{12}C(p,xγ)^{10}B
4.44 MeV: ^{12}C(p,p'γ)^{12}C
4.44 MeV: ^{12}C(p,xγ)^{11}B

Using a Tesla 40K GPU accelerator (NVIDIA Corporation, Santa Clara, California, USA), treatment plan delivery for all samples was simulated in gPMC, which was designed for proton therapy simulations.[214] For every sample, 17 different range error scenarios were simulated, ranging from an undershoot of 16 mm to an overshoot of 16 mm, in increments of 2 mm. Discrete scenarios were interpolated between to allow the resulting model to be continuous. Measured proton ranges were then determined by minimizing the discrepancy between measurement and model. Optimizations left proton range as well as oxygen and carbon concentrations as free parameters. Prompt gamma-ray spectroscopy therefore allowed elemental compositions to be determined in addition to proton range. Overall, prompt gamma-ray detection models relied on three vital components:

- **Prompt gamma-ray emission models** based on proton energy spectra simulated with gPMC and experimentally-determined nuclear reaction cross-sections
- **Prompt gamma-ray transmission probabilities** determined via ray tracing on the relevant CT scan
- **Prompt gamma-ray detection probabilities** determined via previously-performed TOPAS Monte Carlo simulations of the detection system's geometry

Since Monte Carlo simulations incorporated SPRs relative to water measured with the Zebra MLIC, proton range shifts were determined relative to a ground truth based on measured SPRs. Measurements at the sample interface were performed for adipose tissue and spongiosa because of the considerable differences in SPR and elemental composition between these two samples. For the interface measurement, ground truth proton ranges assumed that the entire irradiated sample consisted of adipose tissue.
Measured oxygen and carbon concentrations were determined on an absolute basis and compared to ground truth values largely based on combustion analysis. Prompt gamma-ray spectroscopy results were evaluated on a proton pencil-beam spot-wise basis. To improve statistics but at the cost of a reduction in spatial resolution, data of pencil-beam spots within a radius of 15 mm were aggregated. All pencil-beam spots within this radius were included, and approaches such as Gaussian-like weighting were not applied. This approach was in part justified by the overlap which already exists between neighboring spots near the proton end-of-range as a result of multiple Coulomb scattering. A detailed overview over all aspects of the prompt gamma-ray spectroscopy data analysis workflow is provided in a previous publication by the research group at MGH.[13]

5.3 Results

5.3.1 Measurements of sample stopping power ratios (SPRs)

Sample SPRs relative to water were determined based on MLIC measurements of the relevant sample, water, and an empty container (for a more accurate correction of the container walls). For all samples, stopping power ratios relative to water are shown in Table 5.6.

Table 5.6: Measured sample SPRs relative to water. Values were calculated based on MLIC measurements of the relevant sample, water, and an empty container.

Sample	SPR (± 0.005)
Muscle	1.055
Adipose tissue	0.964
Spongiosa	1.064
Cortical bone	1.308
Brain	1.014
Liver	1.061

5.3.2 Proton range verification via prompt gamma-ray spectroscopy

Prompt gamma-ray spectroscopy measurements allowed proton range differences between measurement and ground truth to be determined for all pencil-beam spots. For the example of the porcine liver sample, pencil-beam spot-wise range deviations are shown in Figure 5.4.

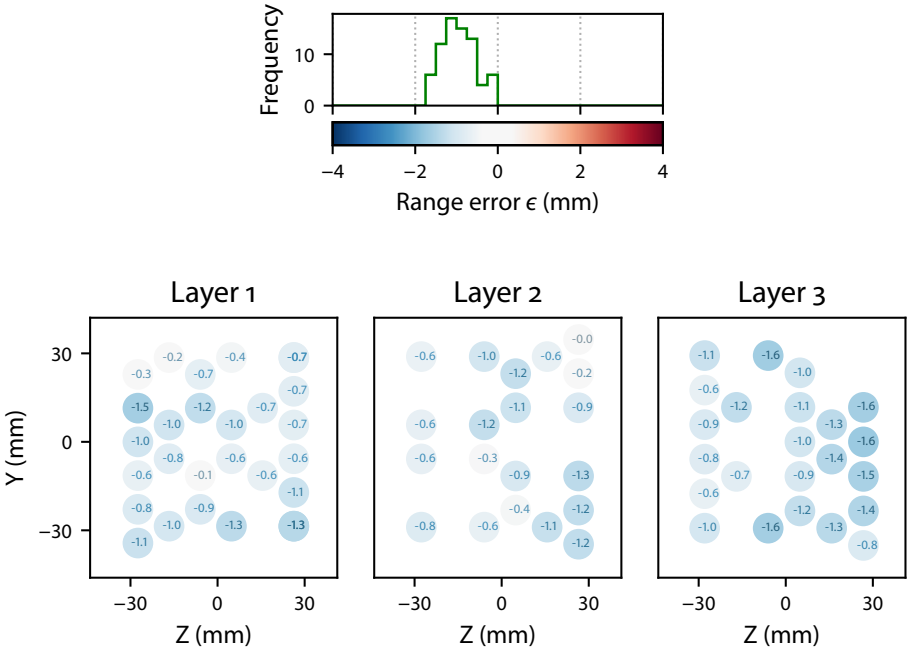

Figure 5.4: Pencil-beam spot-wise range deviations between measurement and ground truth for the porcine liver sample. The histogram at the top depicts the frequency of range deviations of different magnitudes. The three scatter plots depict the three most distal energy layers. Within an energy layer, every circle corresponds to a pencil-beam spot, with the number inside the circle indicating the corresponding measured range difference (considering spot aggregation).

Over all proton pencil-beam spots, the mean difference between measured proton ranges and the ground truth was 1.2 mm or less. The mean standard deviation over all samples was 0.9 mm (range: 0.4 mm to 1.6 mm). Differences between ground truth proton ranges and proton ranges determined using prompt gamma-ray spectroscopy are shown in Figure 5.5.

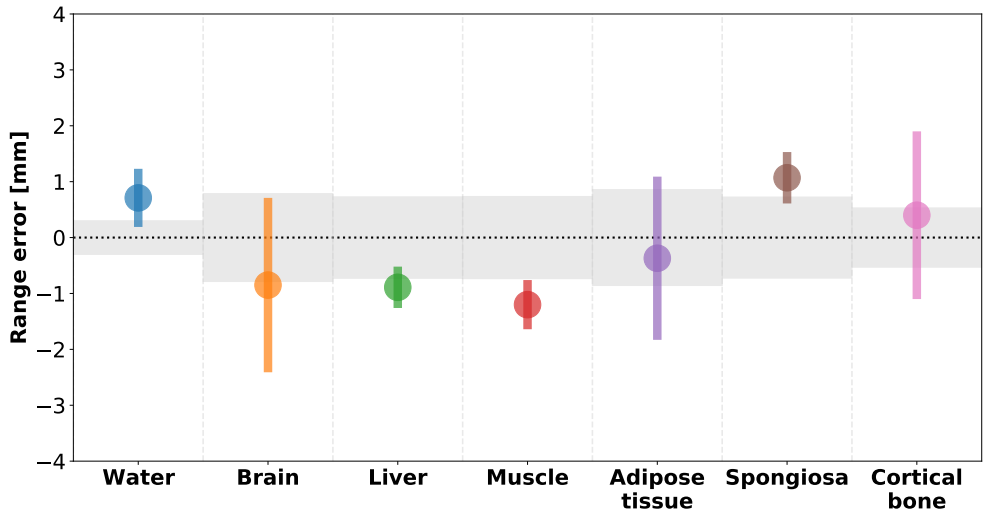

Figure 5.5: Range deviations measured using prompt gamma-ray spectroscopy relative to the ground truth, which was determined using MLIC measurements. Data points indicate the mean value over all proton pencil-beam spots, while error bars depict the corresponding standard deviation. The uncertainty band around the y-axis indicates setup uncertainties of the prompt gamma-ray detector as well as uncertainties in SPR values. The smaller uncertainty band for the water sample is explained by SPR values being defined relative to water.

5.3.3 Determination of elemental compositions

Prompt gamma-ray spectroscopy measurements allowed elemental compositions of all samples to be determined in addition to the proton range. For the example of the porcine liver sample, the elemental composition in terms of the oxygen and carbon concentration is shown in Figure 5.6.
Ground truth elemental compositions were determined using combustion analysis or tissue-mimicking sample components of known compositions. Over all samples, the mean difference between elemental compositions measured using prompt gamma-ray spectroscopy and the ground truth was 0.06 $\frac{g}{cm^3}$ (range: 0.00 $\frac{g}{cm^3}$ to 0.12 $\frac{g}{cm^3}$). For all samples, ground truth and measured elemental compositions are provided in Table 5.7.

5.3.4 Prompt gamma-ray spectroscopy performed at a tissue interface

To test the detector system's ability to differentiate between samples, the spongiosa and adipose tissue sample were placed on the sample platform together, and a prompt gamma-ray spectroscopy measurement was performed at the interface between the samples. The resulting differences between measured proton ranges and the ground truth are shown in Figure 5.7. As shown in Table 5.6, the stopping power ratio of adipose tissue is smaller than that of spongiosa. Since the ground truth assumed that the entire sample consisted of adipose tissue, this resulted in the detection of considerably undershoots in the irradiated area that was filled with spongiosa instead. Measured range errors in adipose tissue, on the other hand, were markedly lower. Intermediate values in the center of the field reflect the effects of the sample interface and of the merging of data from different proton pencil-beam

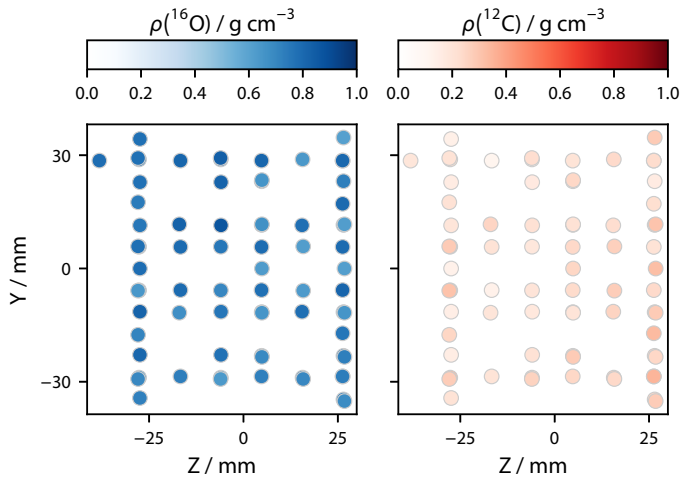

Figure 5.6: Pencil-beam spot-wise derivation of the oxygen and carbon concentrations for the porcine liver sample.

Table 5.7: Measured and ground truth elemental compositions for all samples. Ground truth values were determined using combustion analysis or tissue-mimicking sample components of known compositions. Measured values concern the mean value over all proton pencil-beam spots.

	Oxygen $[\frac{g}{cm^3}]$		**Carbon** $[\frac{g}{cm^3}]$	
Sample	**Ground truth**	**PG spectroscopy**	**Ground truth**	**PG spectroscopy**
Water	0.89	0.91	0.00	0.07
Muscle	0.78	0.82	0.13	0.16
Adipose tissue	0.09	0.09	0.74	0.67
Spongiosa	0.41	0.42	0.45	0.49
Cortical bone	0.98	0.93	0.00	0.10
Brain	0.81	0.77	0.08	0.18
Liver	0.81	0.74	0.11	0.23

spots.

Figure 5.8 depicts measured oxygen and carbon concentrations for the prompt gamma-ray spectroscopy measurement performed at the interface between the adipose tissue and spongiosa sample. As shown in Table 5.7, the adipose tissue sample contained a considerable amount of carbon, while the spongiosa sample's oxygen concentration was markedly higher. This is reflected in the measured elemental compositions.

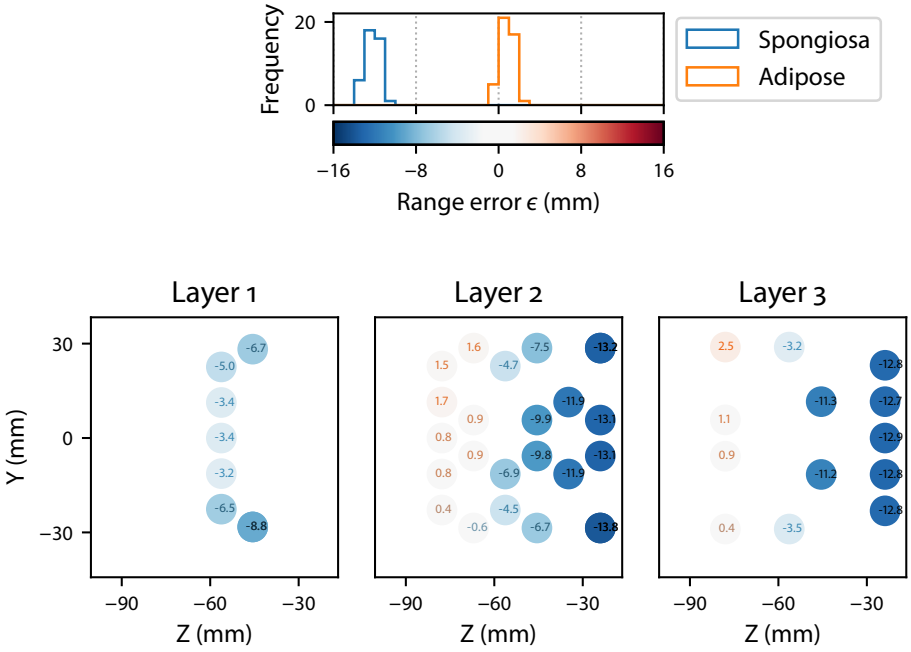

Figure 5.7: Pencil-beam spot-wise range deviations between measurement and ground truth at the interface between the adipose tissue and spongiosa sample. Ground truth proton ranges assumed the stopping power ratio of adipose tissue in the entire irradiated area, leading to the detection of considerable undershoots in spongiosa.

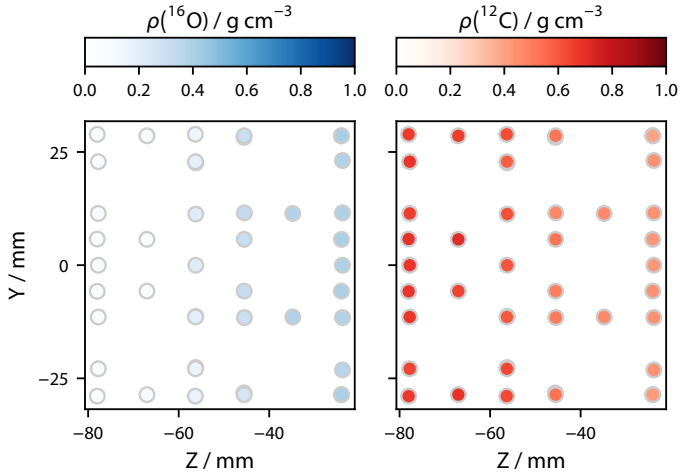

Figure 5.8: Pencil-beam spot-wise oxygen and carbon concentrations at the interface between the adipose tissue and spongiosa sample.

5.4 Discussion

5.4.1 Prompt gamma-ray spectroscopy-based proton range verification

Differences between measured proton ranges and the ground truth were small. For all samples, the mean difference over all proton pencil-beam spots was 1.2 mm or smaller. The uncertainty in the ground truth proton range was estimated to be lower than 0.9 mm for all samples. Contributions included uncertainties in the detector setup as well as uncertainties in the determined SPR values. The system was able to detect range shifts induced by two different samples when a measurement at the sample interface was performed. The highest standard deviation over all pencil-beam spots was observed in the case of the porcine brain sample. This was likely the result of small inhomogeneities in the form of microbubbles of air, which were specific to and quite pronounced in said sample. The high standard deviation observed for the adipose tissue sample is explained by its low oxygen and high carbon content, since the prompt gamma-ray yield from carbon is lower than that from oxygen.[12]
Measured proton range deviations were determined relative to the ground truth, which was based on multi-layer ionization chamber measurements. Uncertainties in measured sample SPRs relative to water may therefore have contributed to slightly higher measured proton range deviations. Sources of uncertainties in measured sample SPRs include variations in the thickness of the container walls and minor inhomogeneities such as the aforementioned air bubbles in the porcine brain sample.

5.4.2 Elemental compositions determined using prompt gamma-ray spectroscopy

For all samples, elemental compositions determined using prompt gamma-ray spectroscopy were in good agreement with the ground truth. Over all samples, the mean difference between elemental compositions measured using prompt gamma-ray spectroscopy and the ground truth was 0.06 $\frac{g}{cm^3}$ (range: 0.00 $\frac{g}{cm^3}$ to 0.12 $\frac{g}{cm^3}$). Furthermore, the detector was able to accurately distinguish between samples of different elemental compositions when a measurement at the sample interface was performed. Samples with low carbon concentrations exhibited a small bias in the determined carbon concentrations. This was likely the result of the fit of the 4.44 MeV prompt gamma-ray line when the relevant prompt gamma-ray counts were low compared to the background. The resulting effect on the determined proton range was confirmed to be below 0.1 mm.
The highest differences between measured and ground truth elemental compositions were observed in the porcine brain and liver samples. Porcine phantoms consisted of samples taken from 25 different animals, and elemental compositions between different samples may have differed slightly. However, combustion analysis was conducted on three different sections of the porcine samples, and agreement was excellent between different sections. The effects of such variations in elemental compositions are therefore expected to have been limited.
Ground truth elemental compositions were largely determined using CHNS combustion analysis, for which trace elements were assumed to be negligible. This assumption contributed to uncertainties in the ground truth oxygen concentration. The brain and liver sample, for example, are expected to consist of trace elements such as sodium, phosphorus, chlorine, and potassium by approximately 1%.[207] Since they were determined explicitly, ground truth concentrations of carbon, hydrogen, nitrogen, and sulfur were not affected by this assumption.
The only components for which ground truth elemental compositions were not determined using combustion analysis were HA and SDS used in some of the tissue-mimicking samples. However, analytical-grade HA and SDS were used, with a guaranteed purity higher than 99%. The elemental composition of both of these components was therefore already known with a high degree of accuracy. In addition, tissue-mimicking samples generally contained no or only a small percentage of HA and SDS. Uncertainties in ground truth elemental compositions were therefore expected to be small.

5.4.3 Methodological considerations

Measurements were performed using a clinical system, and no measurement-specific restrictions were placed on aspects such as beam current. For prompt gamma-ray spectroscopy, a dose of 0.9 Gy was delivered to the target structure. This is in line with the conventional dose delivered for clinical treatments per treatment field per day.
A data aggregation radius of 15 mm was used for the analyses of all prompt gamma-ray spectroscopy measurements. That is to say that results of pencil-beam spots within 15 mm of each other were merged. This approach was chosen to improve statistics, albeit at the cost of a reduction in spatial resolution. The data aggregation radius of 15 mm was considered to constitute a fair balance between these two factors.

5.5 Conclusion and outlook

The performance of MGH's prompt gamma-ray spectroscopy detector prototype for proton range verification was verified using a variety of tissue-mimicking and porcine samples. Agreement between proton ranges measured using prompt gamma-ray spectroscopy and the ground truth, which was determined based on MLIC measurements, was excellent. Sources of uncertainty included the accuracy of the sample setup and the alignment of the prompt gamma-ray spectroscopy detector prototype. The highest standard deviation over all pencil-beam spots was observed in the porcine brain sample. This was likely the result of microbubbles of air, which were specific to and quite pronounced in the aforementioned sample.
Prompt gamma-ray spectroscopy allowed elemental compositions of samples to be determined simultaneously with proton range. Ground truth elemental compositions of all samples were determined using combustion analysis or, in the case of tissue-mimicking samples, analytical-grade components of high guaranteed purity. Oxygen and carbon concentrations determined using prompt gamma-ray spectroscopy were in excellent agreement with the ground truth.
The reported measurements confirm the performance of the prompt gamma-ray spectroscopy detector prototype in a variety of different materials. Samples included a range of different soft tissues as well as spongiosa and cortical bone. The measurements reported in this study therefore bridge the gap between previously-reported experimental measurements and clinical *in vivo* measurements performed during patient treatment.

CHAPTER 6

Summary, conclusion, and outlook

Uncertainties in the *in vivo* proton range remain some of the most considerable hurdles for proton therapy.[4] One of the main advantages of proton therapy over conventional photon treatments is the conformality of the resulting dose distribution to the target and the associated sparing of normal tissues.[1] However, taking proton range uncertainties into account during treatment planning results in a degrading of the dose conformality to the target, increasing doses to nearby OARs. The full potential of proton therapy can therefore only be achieved through proton range uncertainty reductions.

This dissertation focused on both the benefits of proton range uncertainty reductions as well as the manner in which they can be achieved. For the study presented in Chapter 3, the direct benefits of range uncertainty reductions were quantified in terms of the associated reductions in NTCPs and normal tissue doses.[182] The data set for this study consisted of treatment plans for ten cancer patients with clival tumors, and relevant organs-at-risk included the brainstem and the optic chiasm. Reductions in the general normal tissue volume receiving at least 70% of the prescription dose were also quantified.

In terms of brainstem sparing, range uncertainty reduction benefits increased with the highest dose prescribed to any part of the target. The brainstem was generally larger than or at most of the same size as the CTV. The majority of the brainstem therefore received little or no dose. The dose to the irradiated part of the brainstem therefore had to be comparatively high for changes in brainstem NTCP to be observed. Range uncertainty reduction benefits were therefore especially pronounced in cases in which the maximum prescription dose was higher than the tolerance value of TD50 = 65 Gy(RBE) used in the LKB model based on which brainstem NTCP values were calculated.[189] LKB model parameters for brainstem NTCP calculations may have been conservative, potentially resulting in elevated NTCPs.[194] The brainstem abutted the target structure in all ten cases.

Distance between the optic chiasm and the target, on the other hand, varied between cases. Range uncertainty reduction benefits with respect to sparing of the optic chiasm were only observed in cases in which the optic chiasm was within half a centimeter of the CTV. Due to the optic chiasm's small volume, a large portion of the chiasm received a considerable dose in all cases in which the chiasm was sufficiently close to the target. The largest changes in NTCP were observed in a case with a particularly high prescription dose. This was the result of the tolerance dose of TD50 = 72 Gy(RBE) used in the underlying LKB model, which was high compared to most prescription doses studied.[189,191,192] In terms of the general normal tissue volume receiving at least 70% of the prescription dose, range uncertainty reduction benefits increased with target volume.

The aforementioned range uncertainty reduction benefits only considered NTCP and normal tissue dose reductions achieved under the assumption of current clinical practices. However, range uncertainty reductions have additional indirect benefits, including the feasibility of novel beam arrangements at lower levels of range uncertainty. Current proton therapy beam arrangements are often chosen conservatively to limit the potential effects of range uncertainties.[10] As range uncertainties are reduced, novel beam arrangements which are currently infeasible will become favorable.

The study presented in Chapter 4 quantified the benefits of novel proton therapy beam arrangements,

based on treatment plans for ten cancer patients with brain or skull base tumors.[195] As was the case in the study presented in Chapter 3, range uncertainty reduction benefits with respect to brainstem sparing increased with prescription dose. It has been suggested that the benefits associated with reductions in setup margins exceed the direct benefits of range uncertainty reductions.[183,184] However, the benefits of novel beam arrangements exceeded the direct benefits of range uncertainty reductions, by a factor of 2 or more in some cases. Indirect range uncertainty reduction benefits such as the feasibility of novel beam arrangements at lower levels of range uncertainty may therefore play an important role and have to be taken into account when quantifying the total benefits of range uncertainty reductions.

Radiobiological effects near the proton end-of-range remain an important consideration. Variable RBE models generally exhibit an increase in RBE as a function of LET, since the associated denser ionization tracks lead to more complex forms of DNA damage such as DNA double strand breaks, which are more difficult to repair correctly.[42–45] Since novel beam arrangements may place the proton end-of-range near organs-at-risk which are in close proximity to the target, such beam arrangements are expected to be especially affected by elevated RBEs in regions of high LET. In the study presented in Chapter 4, all novel beam arrangements were favorable at a range uncertainty of 2% or lower. Novel beam arrangements would therefore have remained favorable even under consideration of RBE-induced range shifts. Nevertheless, further studies are needed to help fully understand the potential radiobiological risks associated with novel beam arrangements and to what extent they may be mitigated, for example through the use of LET-based optimization.[202]

Efforts to quantify range uncertainty reduction benefits have thus far focused on patients with head & neck or brain tumors.[182–184] In the future, it would therefore be of interest to expand the developed methodology to a variety of different treatment sites to determined patient subsets which would most benefit from reductions in proton range uncertainties. Implementing novel approaches such as beam angle- and LET- or RBE-guided optimization would also be highly valuable, especially when considering cases in which considerable variations in RBE in or in close proximity to nearby organs-at-risk are expected.[202–204] Future clinical developments may not only include the feasibility of novel beam arrangements but also the implementation of proton arc therapy, for which the target is irradiated from a considerably higher number of beam directions.[10,215,216] It would therefore also be of interest to investigate how the development of such novel irradiation techniques will affect the importance of proton range uncertainties and the benefits associated with reducing them.

The study presented in Chapter 5 validated the performance of the prompt gamma-ray spectroscopy detector prototype developed at MGH using a variety of tissue-mimicking and porcine samples.[13,205] Tissue-mimicking samples consisted of varying amounts of water, gelatin, porcine lard, HA, and SDS, and were created according to recipes guided by ICRU Report 44 and ICRP Publication 23.[206–208] Measurements were performed at a clinical proton therapy facility and without measurement-specific restrictions being placed on aspects such as dose or beam current. For all samples, ground truth elemental compositions were determined via combustion analysis or through the use of components of known elemental compositions.[209] MLIC measurements were performed such that SPRs relative to water as well as ground truth proton ranges could be determined for all samples.

The mean difference between proton ranges measured using prompt gamma-ray spectroscopy and the ground truth was smaller than or equal to 1.2 mm for all samples. This was 0.9% of the depth of the center of the target structure, compared to current clinical range uncertainties of 2.5% + 1.5 mm to 3.5% + 3 mm.[4,193] Relevant considerations included uncertainties in the setup of the sample as well as the setup of the detector prototype. The highest standard deviation over all proton pencil-beam spots was observed in the porcine brain sample and was likely the result of minor inhomogeneities such as microbubbles of air. When a measurement was performed at the interface between two samples, prompt gamma-ray spectroscopy was able to detect the difference in the proton range shifts induced by the two different samples.

Agreement between elemental compositions determined using prompt gamma-ray spectroscopy and ground truth elemental compositions was likewise excellent. The prompt gamma-ray spectroscopy

detector prototype was therefore able to differentiate between samples of different elemental compositions accurately. This was reflected in a measurement performed at an interface between two samples, during which the system was able to detect marked differences in oxygen and carbon concentrations.

Some experimental proton range verification measurements via prompt gamma-ray spectroscopy have been reported previously, and the results of the first prompt gamma-ray spectroscopy measurements performed during clinical treatment fractions are currently being prepared for publication.[13] However, it remains to be determined how the results of range verification measurements can best be implemented into routine clinical practice. Potential implementations may include the delivery of a test beam for range verification prior to the delivery of the full treatment fraction. For the prompt gamma-ray spectroscopy detector prototype developed at MGH, a further integration of the system into the treatment room can also be considered. The detection system is currently mounted on a wheeled hexapod for easy maneuvering into and out of the treatment room. However, a future integration into the treatment room itself, for example through a detection system mounted onto the proton gantry directly, may also eventually be possible and help reduce errors in the setup of the detection system.

The work performed for this thesis, both in terms of treatment planning studies and range verification measurements via prompt gamma-ray spectroscopy, supports ongoing efforts to translate proton range verification into routine clinical practice. Clinical range verification implementations may take the form of prompt gamma-ray spectroscopy, but the quantified range uncertainty reduction benefits equally apply to the other numerous techniques which are currently under investigation. Since proton range uncertainties remain a considerable hurdle, reducing them would allow the advantages of proton therapy treatments to be more fully exploited in clinical practice.

Bibliography

[1] R. R. Wilson, "Radiological Use of Fast Protons," *Radiology*, vol. 47, no. 5, pp. 487–491, Nov. 1946.

[2] P. P. Connell and S. Hellman, "Advances in Radiotherapy and Implications for the Next Century: A Historical Perspective," *Cancer Res.*, vol. 69, no. 2, pp. 383–392, Jan. 2009.

[3] S. Gianfaldoni, R. Gianfaldoni, U. Wollina, J. Lotti, G. Tchernev, and T. Lotti, "An Overview on Radiotherapy: From Its History to Its Current Applications in Dermatology," *Open Access Maced. J. Med. Sci.*, vol. 5, no. 4, pp. 521–525, Jul. 2017.

[4] H. Paganetti, "Range uncertainties in proton therapy and the role of Monte Carlo simulations," *Phys. Med. Biol.*, vol. 57, no. 11, R99–R117, Jun. 2012.

[5] *GBD Results Tool | GHDx*, `https://ghdx.healthdata.org/gbd-results-tool`, Accessed: 2022-03-22.

[6] *American College of Surgeons - Cancer Department - NCDB Hospital Public Benchmark Reports*, `https://reportsncdb.facs.org/BMPub/index.cfm`, Accessed: 2022-03-21.

[7] R. Baskar, K. A. Lee, R. Yeo, and K.-W. Yeoh, "Cancer and Radiation Therapy: Current Advances and Future Directions," *Int. J. Med. Sci.*, vol. 9, no. 3, pp. 193–199, Feb. 2012.

[8] *PTCOG - Facilities in Operation*, `https://www.ptcog.ch/index.php/facilities-in-operation`, Accessed: 2022-03-22.

[9] *Division for Human Health: DIRAC (DIrectory of RAdiotherapy Centres*, `https://dirac.iaea.org/Query/Countries`, Accessed: 2022-07-19.

[10] A.-C. Knopf and A. J. Lomax, "In vivo proton range verification: a review," *Phys. Med. Biol.*, vol. 58, no. 15, R131–R160, Aug. 2013.

[11] J. M. Verburg, K. Riley, T. Bortfeld, and J. Seco, "Energy- and time-resolved detection of prompt gamma-rays for proton range verification," *Phys. Med. Biol.*, vol. 58, no. 20, pp. L37–L49, Oct. 2013.

[12] J. M. Verburg and J. Seco, "Proton range verification through prompt gamma-ray spectroscopy," *Phys. Med. Biol.*, vol. 59, no. 23, pp. 7089–7106, Oct. 2014.

[13] F. Hueso-González, M. Rabe, T. A. Ruggieri, T. Bortfeld, and J. M. Verburg, "A full-scale clinical prototype for proton range verification using prompt gamma-ray spectroscopy," *Phys. Med. Biol.*, vol. 63, no. 18, Sep. 2018.

[14] W. C. Röntgen, "Ueber eine neue Art von Strahlen," *Ann. Phys.*, vol. 300, no. 1, pp. 12–17, Jan. 1898.

[15] E. H. Grubbé, "Priority in the Therapeutic Use of X-rays," *Radiology*, vol. 21, no. 2, Aug. 1933.

[16] W. P. Levin, H. Kooy, J. S. Loeffler, and T. F. DeLaney, "Proton beam therapy," *Br. J. Cancer*, vol. 93, no. 8, pp. 849–854, Oct. 2005.

[17] H. Liu and J. Y. Chang, "Proton therapy in clinical practice," *Chin. J. Cancer*, vol. 30, no. 5, pp. 315–326, May 2011.

[18] R. Mohan and D. Grosshans, "Proton Therapy – Present and Future," *Adv. Drug. Deliv. Rev.*, vol. 109, pp. 26–44, Dec. 2017.

[19] X. Tian, K. Liu, Y. Hou, J. Cheng, and J. Zhang, "The evolution of proton beam therapy: Current and future status," *Mol. Clin. Oncol.*, vol. 8, no. 1, pp. 15–21, Jan. 2018.

[20] J. M. Slater, J. O. Archambeau, D. W. Miller, M. I. Notarus, W. Preston, and J. D. Slater, "The proton treatment center at Loma Linda University Medical Center: Rationale for and description of its development," *Int. J. Radiat. Oncol. Biol. Phys.*, vol. 22, no. 2, pp. 383–389, 1992.

[21] J. H. Lawrence, "Proton irradiation of the pituitary," *Cancer*, vol. 10, no. 4, pp. 795–798, Jul. 1957.

[22] M. Ju, A. T. Berman, and N. Vapiwala, "The evolution of proton beam therapy: insights from early trials and tribulations," *Int. J. Radiat. Oncol. Biol. Phys.*, vol. 90, no. 4, pp. 733–735, Nov. 2014.

[23] J. M. Slater, D. W. Miller, and J. O. Archambeau, "Development of a hospital-based proton beam treatment center," *Int. J. Radiat. Oncol. Biol. Phys.*, vol. 14, no. 4, pp. 761–775, Apr. 1988.

[24] W. D. Newhauser and R. Zhang, "The physics of proton therapy," *Phys. Med. Biol.*, vol. 60, no. 8, R155–R209, Apr. 2015.

[25] H. Bethe, "Zur Theorie des Durchgangs schneller Korpuskularstrahlen durch Materie," *Ann. Phys.*, vol. 397, no. 3, pp. 325–400, 1930.

[26] F. Bloch, "Zur Bremsung rasch bewegter Teilchen beim Durchgang durch Materie," *Ann. Phys.*, vol. 408, no. 3, pp. 285–320, 1933.

[27] U. Fano, "Penetration of Protons, Alpha Particles, and Mesons," *Annu. Rev. Nucl. Sci.*, vol. 13, pp. 1–66, 1963.

[28] H. Paganetti, "Nuclear interactions in proton therapy: dose and relative biological effect distributions originating from primary and secondary particles," *Phys. Med. Biol.*, vol. 47, no. 5, pp. 747–764, Mar. 2002.

[29] X.-J. Li, Y.-C. Ye, Y.-S. Zhang, and J.-M. Wu, "Empirical modeling of the percent depth dose for megavoltage photon beams," *PLoS One*, vol. 17, no. 1, 2022.

[30] P. B. Romesser *et al.*, "Proton beam radiation therapy results in significantly reduced toxicity compared with intensity-modulated radiation therapy for head and neck tumors that require ipsilateral radiation," *Radiother. Oncol.*, vol. 118, no. 2, pp. 286–292, Feb. 2016.

[31] B. C. Baumann *et al.*, "Comparative Effectiveness of Proton vs Photon Therapy as Part of Concurrent Chemoradiotherapy for Locally Advanced Cancer," *JAMA Oncol.*, vol. 6, no. 2, pp. 237–246, Feb. 2020.

[32] R. Leroy, N. Benahmed, F. Hulstaert, N. Van Damme, and D. De Ruysscher, "Proton Therapy in Children: A Systematic Review of Clinical Effectiveness in 15 Pediatric Cancers," *Int. J. Radiat. Oncol. Biol. Phys.*, vol. 95, no. 1, pp. 267–278, May 2016.

[33] *Stopping-Power & Range Tables for Electrons, Protons, and Helium Ions | NIST*, `https://www.nist.gov/pml/stopping-power-range-tables-electrons-protons-and-helium-ions`, Accessed: 2022-05-10.

[34] H. Paganetti *et al.*, "Relative biological effectiveness (RBE) values for proton beam therapy," *Int. J. Radiat. Oncol. Biol. Phys.*, vol. 53, no. 2, pp. 407–421, Jun. 2002.

[35] E. Blomquist, K. R. Russell, B. Stenerlöw, A. Montelius, E. Grusell, and J. Carlsson, "Relative biological effectiveness of intermediate energy protons. Comparisons with 60Co gamma-radiation using two cell lines," *Radiother. Oncol.*, vol. 28, no. 1, pp. 44–51, Jul. 1993.

[36] H. Paganetti, "Relative biological effectiveness (RBE) values for proton beam therapy. Variations as a function of biological endpoint, dose, and linear energy transfer," *Phys. Med. Biol.*, vol. 59, no. 22, R419–R472, Nov. 2014.

[37] H. Paganetti, "Proton Relative Biological Effectiveness – Uncertainties and Opportunities," *Int. J. Part. Ther.*, vol. 5, no. 1, pp. 2–14, Sep. 2018.

[38] H. Willers *et al.*, "Toward A variable RBE for proton beam therapy," *Radiother. Oncol.*, vol. 128, no. 1, pp. 68–75, Jul. 2018.

[39] S. McMahon, "The linear quadratic model: usage, interpretation and challenges," *Phys. Med. Biol.*, vol. 64, no. 1, Nov. 2018.

[40] F. Kalholm, L. Grzanka, E. Traneus, and N. Bassler, "A systematic review on the usage of averaged LET in radiation biology for particle therapy," *Radiother. Oncol.*, vol. 161, pp. 211–221, Aug. 2021.

[41] T. Friedrich, U. Scholz, T. Elsässer, M. Durante, and M. Scholz, "Systematic analysis of RBE and related quantities using a database of cell survival experiments with ion beam irradiation," *J. Radiat. Res.*, vol. 54, no. 3, pp. 494–514, May 2013.

[42] A. McNamara, J. Schuemann, and H. Paganetti, "A phenomenological relative biological effectiveness (RBE) model for proton therapy based on all published in vitro cell survival data," *Phys. Med. Biol.*, vol. 60, no. 21, pp. 8399–8416, Nov. 2015.

[43] A. McNamara, H. Willers, and H. Paganetti, "Modelling variable proton relative biological effectiveness for treatment planning," *Br. J. Radiol.*, vol. 93, no. 1107, Mar. 2020.

[44] G. Giovannini *et al.*, "Variable RBE in proton therapy: comparison of different model predictions and their influence on clinical-like scenarios," *Radiat. Oncol.*, vol. 11, no. 1, May 2016.

[45] P. Yepes *et al.*, "Fixed- versus Variable-RBE Computations for Intensity Modulated Proton Therapy," *Adv. Radiat. Oncol.*, vol. 4, no. 1, pp. 156–167, Dec. 2018.

[46] M. Chuong *et al.*, "Minimal acute toxicity from proton beam therapy for major salivary gland cancer," *Acta Oncol.*, vol. 59, no. 2, pp. 196–200, Feb. 2020.

[47] S. Sharma *et al.*, "Quality of Life of Postoperative Photon versus Proton Radiation Therapy for Oropharynx Cancer," *Int. J. Part. Ther.*, vol. 5, no. 2, pp. 11–17, Nov. 2018.

[48] E. B. Holliday *et al.*, "Proton Therapy Reduces Treatment-Related Toxicities for Patients with Nasopharyngeal Cancer: A Case-Match Control Study of Intensity-Modulated Proton Therapy and Intensity-Modulated Photon Therapy," *Int. J. Part. Ther.*, vol. 2, no. 1, pp. 19–28, Jul. 2015.

[49] M. W. McDonald, Y. Liu, M. G. Moore, and P. A. S. Johnstone, "Acute toxicity in comprehensive head and neck radiation for nasopharynx and paranasal sinus cancers: cohort comparison of 3D conformal proton therapy and intensity modulated radiation therapy," *Radiat. Oncol.*, vol. 11, no. 1, Feb. 2016.

[50] M. Huynh, L. G. Marcu, E. Giles, M. Short, D. Matthews, and E. Bezak, "Current status of proton therapy outcome for paediatric cancers of the central nervous system - Analysis of the published literature," *Cancer Treat. Rev.*, vol. 70, pp. 272–288, Nov. 2018.

[51] S. H. Patel *et al.*, "Charged particle therapy versus photon therapy for paranasal sinus and nasal cavity malignant diseases: a systematic review and meta-analysis," *Lancet Oncol.*, vol. 15, no. 9, Aug. 2014.

[52] N. N. Sanford *et al.*, "Protons versus Photons for Unresectable Hepatocellular Carcinoma: Liver Decompensation and Overall Survival," *Int. J. Radiat. Oncol. Biol. Phys.*, vol. 105, no. 1, pp. 64–72, Sep. 2019.

[53] J.-Y. Cheng *et al.*, "Proton versus photon radiotherapy for primary hepatocellular carcinoma: a propensity-matched analysis," *Radiat. Oncol.*, vol. 15, no. 1, Jun. 2020.

[54] *Study of Proton Versus Photon Beam Radiotherapy in the Treatment of Head and Neck Cancer*, https://clinicaltrials.gov/ct2/show/NCT02923570, Accessed: 2021-09-28.

[55] *Randomized Trial of Intensity-Modulated Proton Beam Therapy (IMPT) Versus Intensity-Modulated Photon Therapy (IMRT) for the Treatment of Oropharyngeal Cancer of the Head and Neck*, https://clinicaltrials.gov/ct2/show/NCT01893307, Accessed: 2021-09-28.

[56] *Photon Therapy Versus Proton Therapy in Early Tonsil Cancer. (ARTSCAN V)*, https://clinicaltrials.gov/ct2/show/NCT03829033, Accessed: 2021-09-28.

[57] J. Price, E. Hall, C. West, and D. Thomson, "TORPEdO – A Phase III Trial of Intensity-modulated Proton Beam Therapy Versus Intensity-modulated Radiotherapy for Multi-toxicity Reduction in Oropharyngeal Cancer," *Clin. Oncol. (R. Coll. Radiol.)*, vol. 32, no. 2, pp. 84–88, Feb. 2020.

[58] J. E. Bekelman *et al.*, "Pragmatic randomised clinical trial of proton versus photon therapy for patients with non-metastatic breast cancer: the Radiotherapy Comparative Effectiveness (RadComp) Consortium trial protocol," *BMJ Open*, vol. 9, no. 10, Oct. 2019.

[59] S. H. Lin *et al.*, "Randomized phase IIB trial of proton beam therapy versus intensity-modulated radiation therapy for locally advanced esophageal cancer," *J. Clin. Oncol.*, vol. 38, no. 14, pp. 1569–1579, May 2020.

[60] *Definition of phase II/III clinical trial - NCI Dictionary of Cancer Terms - NCI*, https://www.cancer.gov/publications/dictionaries/cancer-terms/def/phase-ii-iii-clinical-trial, Accessed: 2021-07-20.

[61] R. Mohan *et al.*, "Proton therapy reduces the likelihood of high-grade radiation-induced lymphopenia in glioblastoma patients: phase II randomized study of protons vs photons," *Neuro Oncol.*, vol. 23, no. 2, pp. 284–294, Feb. 2021.

[62] S. Devicienti, L. Strigari, M. D'Andrea, M. Benassi, V. Dimiccoli, and M. Portaluri, "Patient positioning in the proton radiotherapy era," *J. Exp. Clin. Cancer Res.*, vol. 29, no. 1, May 2010.

[63] R. Pidikiti *et al.*, "Commissioning of the world's first compact pencil-beam scanning proton therapy system," *J. Appl. Clin. Med. Phys.*, vol. 19, no. 1, pp. 94–105, Jan. 2018.

[64] G. Vilches-Freixas *et al.*, "Beam commissioning of the first compact proton therapy system with spot scanning and dynamic field collimation," *Br. J. Radiol.*, vol. 93, no. 1107, Mar. 2020.

[65] C. Shang, G. Evans, M. Rahman, and L. Lin, "Beam characteristics of the first clinical 360°rotational single gantry room scanning pencil beam proton treatment system and comparisons against a multi-room system," *J. Appl. Clin. Med. Phys.*, vol. 21, no. 9, pp. 266–271, Sep. 2020.

[66] C. Hua *et al.*, "A robotic C-arm cone beam CT system for image-guided proton therapy: design and performance," *Br. J. Radiol.*, vol. 90, no. 1079, Nov. 2017.

[67] J. L. Romero *et al.*, "Patient positioning for protontherapy using a proton range telescope," *Nucl. Instrum. Methods Phys. Res. A*, vol. 356, no. 2-3, pp. 558–565, Mar. 1995.

[68] M. F. Spadea *et al.*, "Contrast-Enhanced Proton Radiography for Patient Set-up by Using X-Ray CT Prior Knowledge," *Int. J. Radiat. Oncol. Biol. Phys.*, vol. 90, no. 3, pp. 628–636, Nov. 2014.

[69] A. Hammi, S. Koenig, D. C. Weber, B. Poppe, and A. J. Lomax, "Patient positioning verification for proton therapy using proton radiography," *Phys. Med. Biol.*, vol. 63, no. 24, Dec. 2018.

[70] M. Engelsman, H. M. Lu, D. Herrup, M. Bussiere, and H. M. Kooy, "Commissioning a passive-scattering proton therapy nozzle for accurate SOBP delivery," *Med Phys.*, vol. 36, no. 6, Jun. 2009.

[71] M. T. Gillin *et al.*, "Commissioning of the discrete spot scanning proton beam delivery system at the University of Texas M.D. Anderson Cancer Center, Proton Therapy Center, Houston," *Med Phys.*, vol. 37, no. 1, pp. 154–163, Jan. 2010.

[72] E. Pedroni, D. Meer, C. Bula, S. Safai, and S. Zenklusen, "Pencil beam characteristics of the next-generation proton scanning gantry of PSI: design issues and initial commissioning results," *EPJ Plus*, vol. 126, pp. 1–27, Jul. 2011.

[73] X. Ding *et al.*, "A comprehensive dosimetric study of pancreatic cancer treatment using three-dimensional conformal radiation therapy (3DCRT), intensity-modulated radiation therapy (IMRT), volumetric-modulated radiation therapy (VMAT), and passive-scattering and modulated-scanning proton therapy (PT)," *Med. Dosim.*, vol. 39, no. 2, pp. 139–145, Jun. 2014.

[74] D. Giantsoudi, J. Adams, and H. MacDonald Shannon adn Paganetti, "Can differences in linear energy transfer and thus relative biological effectiveness compromise the dosimetric advantage of intensity-modulated proton therapy as compared to passively scattered proton therapy?" *Acta Oncol.*, vol. 57, no. 9, pp. 1259–1264, Sep. 2018.

[75] J. T. Bushberg, J. A. Seibert, E. M. Leidholdt, and J. M. Boone, *The Essential Physics of Medical Imaging*. Philadelphia, PA, USA: Lippincott Williams & Wilkins, 2012.

[76] H. Zaidi and I. El Naqa, "PET-guided delineation of radiation therapy treatment volumes: a survey of image segmentation techniques," *Eur. J. Nucl. Med. Mol. Imaging*, vol. 37, no. 11, pp. 2165–2187, Nov. 2010.

[77] U. Schneider, E. Pedroni, and A. J. Lomax, "The calibration of CT Hounsfield units for radiotherapy treatment planning," *Phys. Med. Biol.*, vol. 41, no. 1, pp. 111–124, Jan. 1996.

[78] L. Koivula, L. Wee, and J. Korhonen, "Feasibility of MRI-only treatment planning for proton therapy in brain and prostate cancers: Dose calculation accuracy in substitute CT images," *Med. Phys.*, vol. 43, no. 8, pp. 4634–4642, Aug. 2016.

[79] G. Shafai-Erfani *et al.*, "MRI-Based Proton Treatment Planning for Base of Skull Tumors," *Int. J. Part. Ther.*, vol. 6, no. 2, pp. 12–25, Sep. 2019.

[80] U. Oelfke and T. Bortfeld, "Inverse planning for photon and proton beams," *Med. Dosim.*, vol. 26, no. 2, pp. 113–124, Jun. 2001.

[81] J. O. Deasy, D. M. Shepard, and T. R. Mackie, "Distal Edge Tracking: A Proposed Delivery Method for Conformal Proton Therapy using Intensity Modulation," in *Proceedings XIIth International Conference on the Use of Computers in Radiation Therapy*, (Madison, WI), D. D. Leavitt and G. Starkschall, Eds., Medical Physics Publishing, 1997, pp. 406–409.

[82] A. J. Lomax, "Intensity modulation methods for proton radiotherapy," *Phys. Med. Biol.*, vol. 44, no. 1, pp. 185–205, Jan. 1999.

[83] A. Trofimov and T. Bortfeld, "Optimization of beam parameters and treatment planning for intensity modulated proton therapy," *Technol. Cancer Res. Treat.*, vol. 2, no. 5, pp. 437–444, Oct. 2003.

[84] F. Albertini, S. Gaignat, M. Bosshardt, and A. J. Lomax, "Planning and Optimizing Treatment Plans for Actively Scanned Proton Therapy," in *Biomedical mathematics: Promising Directions in Imaging, Therapy Planning, and Inverse Problems*, Y. Censor, M. Jiang, and G. Wang, Eds., Madison, WI: Medical Physics Publishing, 2009, ch. 1, pp. 1–18.

[85] A. J. Lomax *et al.*, "Intensity modulated proton therapy: A clinical example," *Med. Phys.*, vol. 28, no. 3, pp. 317–324, Mar. 2001.

[86] T. J. Pugh *et al.*, "Multi-Field Optimization Intensity-Modulated Proton Therapy (MFO-IMPT) for Prostate Cancer: Robustness Analysis through Simulation of Rotational and Translational Alignment Errors," *Med. Dosim.*, vol. 38, no. 3, pp. 344–350, Sep. 2013.

[87] S. Dowdell, C. Grassberger, G. Sharp, and H. Paganetti, "Fractionated Lung IMPT Treatments: Sensitivity to Setup Uncertainties and Motion Effects Based on Single-Field Homogeneity," *Technol. Cancer Res. Treat.*, vol. 15, no. 5, pp. 689–696, Oct. 2016.

[88] C. Thieke *et al.*, "A new concept for interactive radiotherapy planning with multicriteria optimization: First clinical evaluation," *Radiother. Oncol.*, vol. 85, no. 2, pp. 292–298, Nov. 2007.

[89] T. S. Hong, D. L. Craft, F. Carlsson, and T. R. Bortfeld, "Multicriteria Optimization in Intensity-Modulated Radiation Therapy Treatment Planning for Locally Advanced Cancer of the Pancreatic Head," *Int. J. Radiat. Oncol. Biol. Phys.*, vol. 72, no. 4, pp. 1208–1214, Nov. 2008.

[90] L. Hong *et al.*, "A pencil beam algorithm for proton dose calculations," *Phys. Med. Biol.*, vol. 41, no. 8, pp. 1305–1330, Aug. 1996.

[91] H. Paganetti, "Monte Carlo simulations will change the way we treat patients with proton beams today," *Br. J. Radiol.*, vol. 87, no. 1040, Aug. 2014.

[92] P. Andreo, "Monte Carlo simulations in radiotherapy dosimetry," *Radiat. Oncol.*, vol. 13, no. 1, Jun. 2018.

[93] J. Perl, J. Shin, J. Schuemann, B Faddegon, and H Paganetti, "TOPAS: an innovative proton Monte Carlo platform for research and clinical applications," *Med. Phys.*, vol. 39, no. 11, pp. 6818–6837, Nov. 2012.

[94] A. N. Schreuder *et al.*, "Validation of the RayStation Monte Carlo dose calculation algorithm using realistic animal tissue phantoms," *J. Appl. Clin. Med. Phys.*, vol. 20, no. 10, pp. 160–171, Oct. 2019.

[95] H. Paganetti, P. Botas, G. C. Sharp, and B. Winey, "Adaptive proton therapy," *Phys. Med. Biol.*, vol. 66, no. 22, Nov. 2021.

[96] C. L. Brouwer, R. J. H. M. Steenbakkers, J. A. Langendijk, and N. M. Sijtsema, "Identifying patients who may benefit from adaptive radiotherapy: Does the literature on anatomic and dosimetric changes in head and neck organs at risk during radiotherapy provide information to help?" *Radiother. Oncol.*, vol. 115, no. 3, pp. 285–294, Jun. 2015.

[97] L. Placidi *et al.*, "Effect of Anatomic Changes on Pencil Beam Scanned Proton Dose Distributions for Cranial and Extracranial Tumors," *Int. J. Radiat. Oncol. Biol. Phys.*, vol. 97, no. 3, pp. 616–623, Mar. 2017.

[98] E. B. Villarroel, X. Geets, and E. Sterpin, "Online adaptive dose restoration in intensity modulated proton therapy of lung cancer to account for inter-fractional density changes," *phiRO*, vol. 15, pp. 30–37, Jul. 2020.

[99] A. J. A. J. van de Schoot *et al.*, "Dosimetric advantages of proton therapy compared with photon therapy using an adaptive strategy in cervical cancer," *Acta Oncol.*, vol. 55, no. 7, pp. 892–899, Jul. 2016.

[100] M. Bobić *et al.*, "Comparison of weekly and daily online adaptation for head and neck intensity-modulated proton therapy," *Phys. Med. Biol.*, vol. 66, no. 5, Jan. 2021.

[101] S. Acharya *et al.*, "Adaptive Proton Therapy for Pediatric Patients: Improving the Quality of the Delivered Plan With On-Treatment MRI," *Int. J. Radiat. Oncol. Biol. Phys.*, vol. 109, no. 1, pp. 242–251, Jan. 2021.

[102] C. Kurz *et al.*, "Feasibility of automated proton therapy plan adaptation for head and neck tumors using cone beam CT images," *Radiat. Oncol.*, vol. 11, no. 1, Apr. 2016.

[103] J. A. Oliver *et al.*, "Commissioning an in-room mobile CT for adaptive proton therapy with a compact proton system," *J. Appl. Clin. Med. Phys.*, vol. 19, no. 3, pp. 149–158, May 2018.

[104] P. Botas, J. Kim, B. Winey, and H. Paganetti, "Online adaption approaches for intensity modulated proton therapy for head and neck patients based on cone beam CTs and Monte Carlo simulations," *Phys. Med. Biol.*, vol. 64, no. 1, Dec. 2018.

[105] F. Albertini, M. Matter, L. Nenoff, Y. Zhangh, and A. Lomax, "Online daily adaptive proton therapy," *Br. J. Radiol.*, vol. 93, no. 1107, Mar. 2020.

[106] A. C. Kraan *et al.*, "Dose Uncertainties in IMPT for Oropharyngeal Cancer in the Presence of Anatomical, Range, and Setup Errors," *Int. J. Radiat. Oncol. Biol. Phys.*, vol. 87, no. 5, pp. 888–896, Dec. 2013.

[107] Y. Kumazaki, T. Akagi, T. Yanou, D. Suga, Y. Hishikawa, and T. Teshima, "Determination of the mean excitation energy of water from proton beam ranges," *Radiat. Meas.*, vol. 42, no. 10, pp. 1683–1691, Nov. 2007.

[108] B. Schaffner and E. Pedroni, "The precision of proton range calculations in proton radiotherapy treatment planning: experimental verification of the relation between CT-HU and proton stopping power," *Phys. Med. Biol.*, vol. 43, no. 6, pp. 1579–1592, Jun. 1998.

[109] A. J. Lomax, "Intensity modulated proton therapy and its sensitivity to treatment uncertainties 1: the potential effects of calculational uncertainties," *Phys. Med. Biol.*, vol. 53, no. 4, pp. 1027–1042, Feb. 2008.

[110] M. Yang, G. Virshup, J. Clayton, X. R. Zhu, R. Mohan, and L. Dong, "Theoretical variance analysis of single- and dual-energy computed tomography methods for calculating proton stopping power ratios of biological tissues," *Phys. Med. Biol.*, vol. 55, no. 5, pp. 1343–1362, Mar. 2010.

[111] N. Hünemohr, B. Krauss, C. Tremmel, B. Ackermann, O. Jäkel, and S. Greilich, "Experimental verification of ion stopping power prediction from dual energy CT data in tissue surrogates," *Phys. Med. Biol.*, vol. 59, no. 1, pp. 83–96, Jan. 2014.

[112] F. Albertini, A. Bolsi, A. J. Lomax, H. P. Rutz, B. Timmerman, and G. Goitein, "Sensitivity of intensity modulated proton therapy plans to changes in patient weight," *Radiother. Oncol.*, vol. 86, no. 2, pp. 187–194, Feb. 2008.

[113] Y. Z. Szeto, M. G. Witte, S. R. van Kranen, J.-J. Sonke, J. Belderbos, and M. van Herk, "Effects of anatomical changes on pencil beam scanning proton plans in locally advanced NSCLC patients," *Radiother. Oncol.*, vol. 120, no. 2, pp. 286–292, Aug. 2016.

[114] A. J. Lomax, "Myths and realities of range uncertainty," *Br. J. Radiol.*, vol. 93, no. 1107, Mar. 2020.

[115] C. Winterhalter, A. J. Lomax, D. Oxley, D. C. Weber, and S. Safai, "A study of lateral fall-off (penumbra) optimisation for pencil beam scanning (PBS) proton therapy," *Phys. Med. Biol.*, vol. 63, no. 2, Jan. 2018.

[116] T. Landberg *et al.*, "ICRU Report 50," *J. ICRU*, vol. os26, no. 1, Sep. 1993.

[117] S. J. Thomas, "Margins for treatment planning of proton therapy," *Phys. Med. Biol.*, vol. 51, no. 6, pp. 1491–1501, Mar. 2006.

[118] E. Rietzel *et al.*, "Design of 4D treatment planning target volumes," *Int. J. Radiat. Oncol. Biol. Phys.*, vol. 66, no. 1, pp. 287–295, Sep. 2006.

[119] P. C. Park *et al.*, "A BEAM-SPECIFIC PLANNING TARGET VOLUME (PTV) DESIGN FOR PROTON THERAPY TO ACCOUNT FOR SETUP AND RANGE UNCERTAINTIES," *Int. J. Radiat. Oncol. Biol. Phys.*, vol. 82, no. 2, e329–e336, Feb. 2012.

[120] J. Unkelbach, T. C. Y. Chan, and T. Bortfeld, "Accounting for range uncertainties in the optimization of intensity modulated proton therapy," *Phys. Med. Biol.*, vol. 52, no. 10, pp. 2755–2773, May 2007.

[121] J. Unkelbach, T. Bortfeld, B. C. Martin, and M. Soukup, "Reducing the sensitivity of IMPT treatment plans to setup errors and range uncertainties via probabilistic treatment planning," *Med. Phys.*, vol. 36, no. 1, pp. 149–163, Jan. 2009.

[122] J. Unkelbach *et al.*, "Robust radiotherapy planning," *Phys. Med. Biol.*, vol. 63, no. 22, Nov. 2018.

[123] A. Fredriksson, A. Forsgen, and B. Hårdemark, "Minimax optimization for handling range and setup uncertainties in proton therapy," *Med. Phys.*, vol. 38, no. 3, pp. 1672–1684, Mar. 2011.

[124] A. Fredriksson and R. Bokrantz, "A critical evaluation of worst case optimization methods for robust intensity-modulated proton therapy planning," *Med. Phys.*, vol. 41, no. 8, Aug. 2014.

[125] W. Liu, S. J. Frank, X. Li, Y. Li, R. X. Zhu, and R. Mohan, "PTV-based IMPT optimization incorporating planning risk volumes vs robust optimization," *Med. Phys.*, vol. 40, no. 2, Feb. 2013.

[126] W. Liu *et al.*, "Effectiveness of robust optimization in intensity-modulated proton therapy planning for head and neck cancers," *Med. Phys.*, vol. 40, no. 5, May 2013.

[127] F. Kroupal, M. C. Frese, E. Heath, and U. Oelfke, "Robust Radiobiological Optimization for Proton Therapy Treatment Planning," in *IFMBE Proceedings, volume 25/1*, (Berlin, Heidelberg), O. Dössel and W. C. Schlegel, Eds., Spinger, 2009, pp. 433–436.

[128] S. van de Water, F. Albertini, D. c. Weber, B. J. M. Heijmen, M. S. Hoogeman, and A. J. Lomax, "Anatomical robust optimization to account for nasal cavity filling variation during intensity-modulated proton therapy: a comparison with conventional and adaptive planning strategies," *Phys. Med. Biol.*, vol. 63, no. 2, Jan. 2018.

[129] M. Cubillos-Mesías *et al.*, "Including anatomical variations in robust optimization for head and neck proton therapy can reduce the need of adaptation," *Radiother. Oncol.*, vol. 131, pp. 127–134, Feb. 2019.

[130] V. T. Taasti *et al.*, "Comparison of single and dual energy CT for stopping power determination in proton therapy of head and neck cancer," *phiRO*, vol. 6, pp. 14–19, Apr. 2018.

[131] T. G. Flohr *et al.*, "First performance evaluation of a dual-source CT (DSCT) system," *Eur. Radiol.*, vol. 16, no. 2, pp. 256–269, Feb. 2006.

[132] C. H. McCollough, S. Leng, L. Yu, and J. G. Fletcher, "Dual- and Multi-Energy CT: Principles, Technical Approaches, and Clinical Applications," *Radiology*, vol. 276, no. 3, pp. 637–653, Sep. 2015.

[133] N. Hünemohr, H. Paganetti, S. Greilich, O. Jäkel, and J. Seco, "Tissue decomposition from dual energy CT data for MC based dose calculation in particle therapy," *Med. Phys.*, vol. 41, no. 6, Jun. 2014.

[134] P. Wohlfahrt *et al.*, "Clinical Implementation of Dual-energy CT for Proton Treatment Planning on Pseudo-monoenergetic CT scans," *Int. J. Radiat. Oncol. Biol. Phys.*, vol. 97, no. 2, pp. 427–434, Feb. 2017.

[135] E. Bär, A. Lalonde, G. Royle, H.-M. Lu, and H. Bouchard, "The potential of dual-energy CT to reduce proton beam range uncertainties," *Med. Phys.*, vol. 44, no. 6, Jun. 2017.

[136] C. Möhler *et al.*, "Experimental verification of stopping-power prediction from single- and dual-energy computed tomography in biological tissues," *Phys. Med. Biol.*, vol. 63, no. 2, Jan. 2018.

[137] P. Wohlfahrt, C. Möhler, C. Richter, and S. Greilich, "Evaluation of Stopping-Power Prediction by Dual- and Single-Energy Computed Tomography in an Anthropomorphic Ground-Truth Phantom," *Int. J. Radiat. Oncol. Biol. Phys.*, vol. 100, no. 1, pp. 244–253, Jan. 2018.

[138] N. Peters *et al.*, "Reduction of clinical safety margins in proton therapy enabled by the clinical implementation of dual-energy CT for direct stopping-power prediction," *Radiother. Oncol.*, vol. 166, pp. 71–78, Jan. 2022.

[139] R. W. Schulte and S. N. Penfold, "Proton CT for Improved Stopping Power Determination in Proton Therapy, invited," *Trans. Am. Nucl. Soc.*, vol. 106, pp. 55–58, 2012.

[140] G. Poludniowski, N. M. Allinson, and P. M. Evans, "Proton radiography and tomography with application to proton therapy," *Br. J. Radiol.*, vol. 88, no. 1053, Sep. 2015.

[141] K. M. Hanson *et al.*, "Computed tomography using proton energy loss," *Phys. Med. Biol.*, vol. 26, no. 6, pp. 965–983, May 1981.

[142] K. M. Hanson *et al.*, "Proton computed tomography of human specimens," *Phys. Med. Biol.*, vol. 27, no. 1, pp. 25–36, Jun. 1982.

[143] R. P. Johnson *et al.*, "A Fast Experimental Scanner for Proton CT: Technical Performance and First Experience with Phantom Scans," *IEEE Trans. Nucl. Sci.*, vol. 63, no. 1, pp. 52–60, Dec. 2016.

[144] M. Esposito *et al.*, "PRaVDA: The first solid-state system for proton computed tomography," *Phys. Med.*, vol. 55, pp. 149–154, Nov. 2018.

[145] G. Dedes *et al.*, "Experimental comparison of proton CT and dual energy x-ray CT for relative stopping power estimation in proton therapy," *Phys. Med. Biol.*, vol. 64, no. 16, Aug. 2019.

[146] K. Parodi and J. C. Polf, "In vivo range verification in particle therapy," *Med. Phys.*, vol. 45, no. 11, e1036–e1050, Nov. 2018.

[147] D. W. Litzenberg *et al.*, "On-line monitoring of radiotherapy beams: experimental results with proton beams," *Med. Phys.*, vol. 26, no. 6, pp. 992–1006, Jun. 1999.

[148] K. Parodi, W. Enghardt, and T. Haberer, "In-beam PET measurements of beta$^+$ radioactivity induced by proton beams," *Phys. Med. Biol.*, vol. 47, no. 1, pp. 21–36, Jan. 2002.

[149] T. Nishio, T. Sato, H. Kitamura, K. Murakami, and T. Ogino, "Distributions of beta$^+$ decayed nuclei generated in the CH2 and H2O targets by the target nuclear fragment reaction using therapeutic MONO and SOBP proton beam," *Med. Phys.*, vol. 32, no. 4, pp. 1070–1082, Apr. 2005.

[150] X. Zhu and G. El Fakhri, "Proton therapy verification with PET imaging," *Theranostics*, vol. 3, no. 10, pp. 731–740, Sep. 2013.

[151] M. Conti and L. Eriksson, "Physics of pure and non-pure positron emitters for PET: a review and a discussion," *EJNMMI Phys.*, vol. 3, no. 8, Dec. 2016.

[152] K. Parodi *et al.*, "PATIENT STUDY OF IN VIVO VERIFICATION OF BEAM DELIVERY AND RANGE, USING POSITRON EMISSION TOMOGRAPHY AND COMPUTED TOMOGRAPHY IMAGING AFTER PROTON THERAPY," *Int. J. Radiat. Oncol. Biol. Phys.*, vol. 68, no. 3, pp. 920–934, Jul. 2007.

[153] A.-C. Knopf, K. Parodi, T. Bortfeld, H. A. Shih, and H. Paganetti, "Systematic analysis of biological and physical limitations of proton beam range verification with offline PET/CT scans," *Phys. Med. Biol.*, vol. 54, no. 14, pp. 4477–4495, Jul. 2009.

[154] T. Nishio, A. Miyatake, T. Ogino, K. Nakagawa, N. Saijo, and H. Esumi, "The development and clinical use of a beam ON-LINE PET system mounted on a rotating gantry port in proton therapy," *Int. J. Radiat. Oncol. Biol. Phys.*, vol. 76, no. 1, pp. 277–286, Jan. 2010.

[155] X. Zhu *et al.*, "Monitoring proton radiation therapy with in-room PET imaging," *Phys. Med. Biol.*, vol. 56, no. 13, pp. 4041–4057, Jul. 2011.

[156] V. Ferrero *et al.*, "Online proton therapy monitoring: clinical test of a Silicon-photodetector-based in-beam PET," *Sci. Rep.*, vol. 8, Mar. 2018.

[157] A.-C. Knopf *et al.*, "Accuracy of proton beam range verification using post-treatment positron emission tomography/computed tomography as function of treatment site," *Int. J. Radiat. Oncol. Biol. Phys.*, vol. 79, no. 1, pp. 297–304, Jan. 2011.

[158] K. Grogg, X. Zhu, H. Shih, N. Alpert, and G. El Fakhri, "Proton Range Verification with PET Imaging in Brain and Head and Neck Cancers," *J. Nucl. Med.*, vol. 59, no. S1, May 2018.

[159] A.-C. Knopf, K. Parodi, H. Paganetti, E. Cascio, A. Bonab, and T. Bortfeld, "Quantitative assessment of the physical potential of proton beam range verification with PET/CT," *Phys. Med. Biol.*, vol. 53, no. 15, pp. 4137–4151, Aug. 2008.

[160] C.-H. Min, C. H. Kim, M.-Y. Youn, and J.-W. Kim, "Prompt gamma measurements for locating the dose falloff region in the proton therapy," *Phys. Med. Biol.*, vol. 89, no. 18, Nov. 2006.

[161] M. Moteabbed, S. España, and H. Paganetti, "Monte Carlo patient study on the comparison of prompt gamma and PET imaging for range verification in proton therapy," *Phys. Med. Biol.*, vol. 56, no. 4, pp. 1063–1082, Feb. 2011.

[162] J. Smeets *et al.*, "Experimental Comparison of Knife-Edge and Multi-Parallel Slit Collimators for Prompt Gamma Imaging of Proton Pencil Beams," *Front. Oncol.*, vol. 6, Jun. 2016.

[163] E. Draeger *et al.*, "3D prompt gamma imaging for proton beam range verification," *Phys. Med. Biol.*, vol. 63, no. 3, Jan. 2018.

[164] E. Muñoz *et al.*, "Proton range verification with MACACO II Compton camera enhanced by a neural network for event selection," *Sci. Rep.*, vol. 11, no. 1, Apr. 2021.

[165] C. Golnik *et al.*, "Range assessment in particle therapy based on prompt γ-ray timing measurements," *Phys. Med. Biol.*, vol. 59, no. 18, Sep. 2014.

[166] S. Kurosawa *et al.*, "Prompt gamma detection for range verification in proton therapy," *Curr. Appl. Phys.*, vol. 12, no. 2, pp. 364–368, Mar. 2012.

[167] F. Hueso-González *et al.*, "Compton Camera and Prompt Gamma Ray Timing: Two Methods for In Vivo Range Assessment in Proton Therapy," *Front. Oncol.*, vol. 6, Apr. 2016.

[168] C. Richter *et al.*, "First clinical application of a prompt gamma based in vivo proton range verification system," *Radiother. Oncol.*, vol. 118, no. 2, pp. 232–237, Feb. 2016.

[169] Y. Xie *et al.*, "Prompt Gamma Imaging for In Vivo Range Verification of Pencil Beam Scanning Proton Therapy," *Int. J. Radiat. Oncol. Biol. Phys.*, vol. 99, no. 1, pp. 210–218, Sep. 2017.

[170] Y. Xie *et al.*, "Prompt gamma imaging for the identification of regional proton range deviations due to anatomic change in a heterogeneous region," *Br. J. Radiol.*, vol. 93, Dec. 2020.

[171] J. Berthold *et al.*, "First-In-Human Validation of CT-Based Proton Range Prediction Using Prompt Gamma Imaging in Prostate Cancer Treatments," *Int. J. Radiat. Oncol. Biol. Phys.*, vol. 111, no. 4, pp. 1033–1043, Nov. 2021.

[172] G. A. Askaryan, "Hydrodynamic radiation from the tracks of ionizing particles in stable liquids," *Sov. J. At. Energy*, vol. 3, pp. 921–923, Aug. 1957.

[173] K. C. Jones, A. Witztum, C. M. Sehgal, and S. Avery, "Proton beam characterization by proton-induced acoustic emission: simulation studies," *Phys. Med. Biol.*, vol. 59, no. 21, pp. 6549–6563, Nov. 2014.

[174] K. C. Jones *et al.*, "Experimental observation of acoustic emissions generated by a pulsed proton beam from a hospital-based clinical cyclotron," *Med. Phys.*, vol. 42, no. 12, pp. 7090–7097, Dec. 2015.

[175] S. Lehrack *et al.*, "Submillimeter ionoacoustic range determination for protons in water at a clinical synchrocyclotron," *Phys. Med. Biol.*, vol. 62, no. 17, pp. L20–L30, Aug. 2017.

[176] S. K. Patch, D. E. M. Hoff, T. B. Webb, L. G. Sobotka, and T. Zhao, "Two-stage ionoacoustic range verification leveraging Monte Carlo and acoustic simulations to stably account for tissue inhomogeneity and accelerator–specific time structure – A simulation study," *Med. Phys.*, vol. 45, no. 2, pp. 783–793, Feb. 2018.

[177] K. C. Jones *et al.*, "Acoustic-based proton range verification in heterogeneous tissue: simulation studies," *Phys. Med. Biol.*, vol. 63, no. 2, Jan. 2018.

[178] T. Takayanagi *et al.*, "A novel range-verification method using ionoacoustic wave generated from spherical gold markers for particle-beam therapy: a simulation study," *Sci. Rep.*, vol. 9, Mar. 2019.

[179] T. Takayanagi *et al.*, "On-line range verification for proton beam therapy using spherical ionoacoustic waves with resonant frequency," *Sci. Rep.*, vol. 10, Nov. 2020.

[180] S. Kellnberger *et al.*, "Ionoacoustic tomography of the proton Bragg peak in combination with ultrasound and optoacoustic imaging," *Sci. Rep.*, vol. 6, Jul. 2016.

[181] J. Lascaud *et al.*, "Investigating the accuracy of co-registered ionoacoustic and ultrasound images in pulsed proton beams," *Phys. Med. Biol.*, vol. 66, no. 18, Sep. 2021.

[182] S. Tattenberg, T. M. Madden, B. L. Gorissen, T. Bortfeld, K. Parodi, and J. Verburg, "Proton range uncertainty reduction benefits for skull base tumors in terms of normal tissue complication probability (NTCP) and healthy tissue doses," *Med. Phys.*, vol. 48, no. 9, pp. 5356–5366, Sep. 2021.

[183] S. Van de Water, I. van Dam, D. R. Schaart, A. Al-Mamgani, B. J. M. Heijmen, and M. S. Hoogeman, "The price of robustness; impact of worst-case optimization on organ-at-risk dose and complication probability in intensity-modulated proton therapy for oropharyngeal cancer patients," *Radiother. Oncol.*, vol. 120, no. 1, pp. 56–62, Jul. 2016.

[184] D. Wagenaar *et al.*, "Head and neck IMPT probabilistic dose accumulation: Feasibility of a 2 mm setup uncertainty setting," *Radiother. Oncol.*, vol. 154, no. 1, pp. 45–52, Jan. 2021.

[185] H. M. Kooy *et al.*, "A case study in proton pencil-beam scanning delivery," *Int. J. Radiat. Oncol. Biol. Phys.*, vol. 76, no. 2, pp. 624–630, Feb. 2010.

[186] J. Gondzio, "Interior point methods 25 years later," *Eur. J. Oper. Res.*, vol. 218, no. 3, pp. 587–601, May 2010.

[187] B. L. Gorissen, "Interior point methods can exploit structure of convex piecewise linear functions with application in radiation therapy," unpublished, 2022.

[188] S. Petit, J. Seco, and H. Kooy, "Increasing maximum tumor dose to manage range uncertainties in IMPT treatment planning," *Phys. Med. Biol.*, vol. 58, no. 20, pp. 7329–7341, Oct. 2013.

[189] C. Burman, G. J. Kutcher, B. Emami, and M. Goitein, "Fitting of normal tissue tolerance data to an analytic function," *Int. J. Radiat. Oncol. Biol. Phys.*, vol. 21, no. 1, pp. 123–135, May 1991.

[190] R. Mohan *et al.*, "Clinically relevant optimization of 3-D conformal treatments," *Med. Phys.*, vol. 19, no. 4, pp. 933–944, Jul. 1992.

[191] G. L. Jiang *et al.*, "Radiation-induced injury to the visual pathway," *Radiother. Oncol.*, vol. 30, no. 1, pp. 17–25, Jan. 1994.

[192] C. Mayo, M. K. Martel, L. B. Marks, J. Flickinger, J. Nam, and J. Kirkpatrick, "Radiation dose-volume effects of optic nerves and chiasm," *Int. J. Radiat. Oncol. Biol. Phys.*, vol. 76, no. 3S, S28–S35, Mar. 2010.

[193] C. Hahn *et al.*, "Impact of range uncertainty on clinical distributions of linear energy transfer and biological effectiveness in proton therapy," *Med. Phys.*, vol. 47, no. 12, pp. 6151–6162, Dec. 2020.

[194] C. Mayo, E. Yorke, and T. E. Merchant, "Radiation associated brainstem injury," *Int. J. Radiat. Oncol. Biol. Phys.*, vol. 76, no. 3S, S36–S41, Mar. 2010.

[195] S. Tattenberg, T. M. Madden, T. Bortfeld, K. Parodi, and J. Verburg, "Range uncertainty reductions in proton therapy may lead to the feasibility of novel beam arrangements which improve organ-at-risk sparing," *Med. Phys.*, vol. 49, no. 7, pp. 4693–4704, Jul. 2022.

[196] H. Paganetti, "Mechanisms and Review of Clinical Evidence of Variations in Relative Biological Effectiveness in Proton Therapy," *Int. J. Radiat. Oncol. Biol. Phys.*, vol. 112, no. 1, pp. 222–236, Jan. 2022.

[197] J. Vogel *et al.*, "Risk of brainstem necrosis in pediatric patients with central nervous system malignancies after pencil beam scanning proton therapy," *Acta Oncol.*, vol. 58, no. 12, pp. 1752–1756, Dec. 2019.

[198] D. J. Indelicato *et al.*, "Outcomes Following Proton Therapy for Pediatric Low-Grade Glioma," *Int. J. Radiat. Oncol. Biol. Phys.*, vol. 104, no. 1, pp. 149–156, May 2019.

[199] D. Haas-Kogan *et al.*, "NCI Workshop on Proton Therapy for Children: Considerations Regarding Brainstem Injury," *Int. J. Radiat. Oncol. Biol. Phys.*, vol. 101, no. 1, pp. 152–168, May 2018.

[200] D. Giantsoudi *et al.*, "Incidence of CNS Injury for a Cohort of 111 Patients Treated With Proton Therapy for Medulloblastoma: LET and RBE Associations for Areas of Injury," *Int. J. Radiat. Oncol. Biol. Phys.*, vol. 95, no. 1, pp. 287–296, May 2016.

[201] A. Carabe, M. Moteabbed, N. Depauw, J. Schuemann, and H. Paganetti, "Range uncertainty in proton therapy due to variable biological effectiveness," *Phys. Med. Biol.*, vol. 57, no. 5, pp. 1159–1172, Mar. 2012.

[202] D. Giantsoudi, C. Grassberger, D. Craft, A. Niemierko, A. Trofimov, and H. Paganetti, "Linear energy transfer-guided optimization in intensity modulated proton therapy: feasibility study and clinical potential," *Int. J. Radiat. Oncol. Biol. Phys.*, vol. 87, no. 1, pp. 216–222, Sep. 2013.

[203] W. Gu, R. Neph, D. Ruan, W. Zou, L. Dong, and K. Sheng, "Robust Beam Orientation Optimization for Intensity-Modulated Proton Therapy," *Med. Phys.*, vol. 46, no. 8, pp. 3356–3370, Aug. 2019.

[204] V. T. Taasti, L. Hong, J. Shim, J. O. Deasy, and M. Zarepisheh, "Automating proton treatment planning with beam angle selection using Bayesian optimization," *Med. Phys.*, vol. 47, no. 8, pp. 3286–3296, Aug. 2020.

[205] S. Tattenberg *et al.*, "Validation of prompt gamma spectroscopy for proton range verification in tissue-mimicking and porcine samples," *Med. Phys.*, vol. 67, no. 20, 2022.

[206] J. E. Scholey, D. Chandramohan, T. Naren, W. Liu, P. E. Z. Larson, and A. Sudhyadhom, "Technical note: A methodology for improved accuracy in stopping power estimation using MRI and CT," *Med. Phys.*, vol. 48, no. 1, pp. 342–353, Jan. 2021.

[207] A. Allisy, D. R. White, J. Booz, R. V. Griffith, J. J. Spokas, and I. J. Wilson, "ICRU Report 44: Tissue Substitutes in Radiation Dosimetry and Measurement," International Commission on Radiation Units and Measurements, Tech. Rep., 1989.

[208] "ICRP Publication 23: Report on the Task Group on Reference Man," International Commission on Radiological Protection, Tech. Rep., 1975.

[209] F. Li and S. P. Brimmer, "Initial study of a combustion-mass spectrometric system for organic microanalysis," *Anal. Chim. Acta*, vol. 525, no. 1, pp. 141–149, Nov. 2004.

[210] P. Barca, M. Giannelli, M. E. Fantacci, and D. Caramella, "Computed tomography imaging with the Adaptive Statistical Iterative Reconstruction (ASIR) algorithm: dependence of image quality on the blending level of reconstruction," *Australas. Phys. Eng. Sci. Med.*, vol. 41, no. 2, pp. 463–473, Jun. 2018.

[211] *IBA Dosimetry: Zebra - Scan monolayer SOBP measurements*, `https://www.iba-dosimetry.com/product/zebra`, Accessed: 2022-05-11.

[212] K. B. Niepel *et al.*, "Animal tissue-based quantitative comparison of dual-energy CT to SPR conversion methods using high-resolution gel dosimetry," *Phys. Med. Biol.*, vol. 66, no. 7, Mar. 2021.

[213] D. R. White, R. V. Griffith, and I. J. Wilson, "The Composition of Body Tissues," *J ICRU*, vol. 24, no. 1, pp. 5–9, Feb. 1992.

[214] X. Jia, J. Schuemann, H. Paganetti, and S. B. Jiang, "GPU-based fast Monte Carlo dose calculation for proton therapy," *Phys. Med. Biol.*, vol. 57, no. 23, pp. 7783–7797, Nov. 2012.

[215] X. Ding, X. Li, J. M. Zhang, P. Kabolizadeh, C. Stevens, and D. Yan, "Spot-Scanning Proton Arc (SPArc) Therapy: The First Robust and Delivery-Efficient Spot-Scanning Proton Arc Therapy," *Int. J. Radiat. Oncol. Biol. Phys.*, vol. 96, no. 5, pp. 1107–1116, Dec. 2016.

[216] L. Toussaint *et al.*, "Towards proton arc therapy: physical and biologically equivalent doses with increasing number of beams in pediatric brain irradiation," *Acta Oncol.*, vol. 58, no. 10, pp. 1451–1456, Oct. 2019.

List of Publications

Peer-reviewed research articles published over the course of this dissertation

As first author

S. Tattenberg, T. M. Madden, B. L. Gorissen, T. Bortfeld, K. Parodi, and J. Verburg. Proton range uncertainty reduction benefits for skull base tumors in terms of normal tissue complication probability (NTCP) and healthy tissue doses. *Med. Phys.*, 48(9):5356–5366, Sept. 2021.

S. Tattenberg, T. M. Madden, T. Bortfeld, K. Parodi, and J. Verburg. Range uncertainty reductions in proton therapy may lead to the feasibility of novel beam arrangements which improve organ-at-risk sparing. *Med. Phys.*, 49(7):4693-4704, Jul. 2022.

S. Tattenberg, R. Marants, K. Niepel, T. Bortfeld, A. Sudhyadhom, G. Landry, K. Parodi, and J. Verburg. Validation of prompt gamma spectroscopy for proton range verification in tissue-mimicking and porcine samples . *Phys. Med. Biol.*, 67(20), Oct. 2022.

As co-author

Contributions to conferences over the course of this dissertation

As first author

S. Tattenberg, B. L. Gorissen, T. M. Madden, T. Bortfeld, and J. Verburg. The Impact of Range Uncertainties On Organ at Risk Doses in Proton Therapy. *Joint American Association of Physicists in Medicine (AAPM) | Canadian Organization of Medical Physicists (COMP) Meeting*, July 2020, virtual.

S. Tattenberg, T. M. Madden, B. L. Gorissen, T. Bortfeld, K. Parodi, and J. Verburg. The Benefit of Reducing Range Uncertainties in Proton Therapy for Skull Base Tumors. *Annual New England AAPM Meeting*, March 2021, virtual.

S. Tattenberg, T. M. Madden, B. L. Gorissen, T. Bortfeld, K. Parodi, and J. Verburg. The Benefit of Novel Beam Arrangements Made Feasible by Range Uncertainty Reductions in Proton Therapy for Brain and Skull Base Tumors. *63^{rd} Annual AAPM Meeting & Exhibition*, July 2021, virtual.

S. Tattenberg, R. Marants, K. Niepel, T. Bortfeld, A. Sudhyadhom, G. Landry, K. Parodi, and J. Verburg. Prompt Gamma-Ray Spectroscopy Validation for Real-Time Proton Range Verification. *64^{th} Annual AAPM Meeting & Exhibition*, July 2022, Washington, DC, USA.

As co-author

J. Verburg, F. Hueso-González, **S. Tattenberg**, P. Wohlfahrt, T. Ruggieri, and T. Bortfeld. First-In-Human Use of Prompt Gamma-Ray Spectroscopy for Proton Range Verification. *Joint AAPM |*

COMP Meeting, July 2020, virtual.

A. Hammi, **S. Tattenberg**, and F. Hueso-González. Blood Dose Calculation: Proton pencil beam scanning versus passively scattered proton therapy and photon therapy. *59^{th} Annual PTCOG Conference*, June 2021, virtual.

A. Hammi, **S. Tattenberg**, and F. Hueso-González. Blood Dose Calculation in Radiotherapy. *63^{rd} Annual AAPM Meeting & Exhibition*, July 2021, virtual.

A. Hammi, **S. Tattenberg**, and F. Hueso-González. Blood dose calculation model: proton therapy versus photon therapy. Annual Congress of the European Society for Radiotherapy and Oncology (ESTRO), August 2021, Madrid, Spain.

J. Berthold, F. Hueso-González, P. Wohlfahrt, T. Bortfeld, C. Khamfongkhruea, **S. Tattenberg**, M. Zarifi, C. Richter, and J. Verburg. Prompt-gamma based treatment verification: Multi-institutional benchmark experiment of a prompt-gamma-imaging and a prompt-gamma-spectroscopy prototype system using an anthropomorphic head phantom. *60^{th} Annual PTCOG Conference*, June-July 2022, Miami, Florida, USA.

K. Niepel, **S. Tattenberg**, R. Marants, T. Bortfeld, J. Verburg, G. Landry, A. Sudhyadhom, and K. Parodi. Validation of Dual-Energy CT Based Composition Analysis Using Fresh Animal Tissues and Novel, Non-Epoxy Tissue Equivalent Samples. *64^{th} Annual AAPM Meeting & Exhibition*, July 2022, Washington, DC, USA.

K. Niepel, **S. Tattenberg**, R. Marants, T. Bortfeld, J. Verburg, G. Landry, A. Sudhyadhom, and K. Parodi. Verifying dual-energy CT based composition extraction against chemical combustion analysis and prompt gamma imaging. *10^{th} International Symposium on Medical Applications of X-ray, Phase-Contrast & Photon-Counting (IMXP)*, August 2022, Munich, Germany.

F. Hueso-González, J. Berthold, P. Wohlfahrt, T. Bortfeld, C. Khamfongkhruea, **S. Tattenberg**, M. Zarifi, J. Verburg, and C. Richter. Experimental comparison of Prompt Gamma-Ray Imaging and Spectroscopy under Equalized Conditions Using a Calibrated Head Phantom. *Institute of Electrical and Electronics Engineers (IEEE) Nuclear Science Symposium, Medical Imaging Conference and Room Temperature Semiconductor Detector Conference*, November 2022, Milan, Italy.

Acknowledgements

I would like to thank Prof. Dr. Katia Parodi for her supervision and support over the years, both during my time in Munich as well as while I was abroad. The medical physics environment at the Ludwig Maximilian University of Munich (LMU) has allowed me to grow a lot over the past six years, and I would not be at this point without Prof. Parodi and the program at LMU. I would also like to thank Dr. Joost Verburg for his help and guidance over the last four years, and Prof. Dr. Thomas Bortfeld for giving me the opportunity to join his group at MGH. They both supported and taught me a lot, and being able to learn from the research environment at MGH was invaluable.
Thank you as well to everyone working at the offices at 125 Nashua Street, both previously and currently, for the positive working environment they have created. I would especially like to single out Dr. Fernando Hueso-González for his relentless positivity and his endless support, and Dr. Abdelkhalek Hammi for being as good-natured as he is and for all the advice. Further thanks to Dr. Patrick Wohlfahrt, Dr. Nadya Shusharina, and Mislav Bobić as well as Dr. Melek Zarifi and Chunxia Li for their help and support and for making my time in Boston as enjoyable as it was.
For their help with both optimization-related projects, I would like to thank Dr. Bram L. Gorissen and Thomas Madden for their extended support and Dr. Nicolas Depauw for his help with the treatment planning system and, at times, his patience. For the prompt gamma-ray spectroscopy and MLIC measurements, I would like to thank Dr. Greg Sharp for instructing me in the use of the department's CT scanners and Debora De Souza Antonio and Doug Trenholm for their help with the Zebra MLIC. Thanks as well to Dr. Atchar Sudhyadhom and Dr. Raanan Marants for providing the irradiated samples and thereby making the measurements possible, and to Prof. Dr. Guillaume Landry and Katharina Niepel for the helpful discussions related to the project. I would further like to thank the team at MGH's machine shop, especially Tom Ruggieri, Michael Melaragni, and Arthur Brown, as well as the staff of the Francis H. Burr Proton Therapy Center for their part in enabling the measurements.
On a more personal note, thanks also to my parents, Annelie and Roland Tattenberg, as well as my brother, Dr. Jan Tattenberg, for their enduring support over the years, be it financial or otherwise. I would not have been able to pursue my studies without them. I would also like to thank Pip Mamo Dryden, whose support and patience over the years can hardly be overstated.
The studies pursued for this dissertation were in part supported by the Federal Share of program income earned by Massachusetts General Hospital on C06-CA059267, Proton Therapy Research and Treatment Center, and by the National Cancer Institute grant R01-CA229178, Fast Individualized Delivery Adaptation in Proton Therapy. Over the last four years, I was also awarded a PROSA scholarship by LMU, which is funded the German Academic Exchange Service (DAAD) and the Free State of Bavaria, as well as a grant by the Monika Kutzner Foundation, a non-profit organization dedicated to supporting cancer research.